High Temperature Behavior and Self-reporting Properties of Boride Coatings

Von der Fakultät für Georessourcen und Materialtechnik der
Rheinisch-Westfälischen Technischen Hochschule Aachen

zur Erlangung des akademischen Grades eines

Doktors der Ingenieurwissenschaften

genehmigte Dissertation

vorgelegt von

Sebastian Lellig, M. Sc.

Berichtende: Univ.-Prof. Dr. h.c. Jochen Michael Schneider, Ph. D.
Prof. Johann Michler, Ph. D.

Tag der mündlichen Prüfung: 26.06.2025

Abstract

Boride coatings show exceptional properties for high-temperature and extreme environments due to their high thermal stability, oxidation behavior and mechanical properties making them suitable candidates for a sustainable industry.

In the first part, the oxidation behavior and thermal stability of stoichiometric $Ti_{0.12}Al_{0.21}B_{0.67}$ coatings are investigated unraveling the underlying atomic mechanisms. To that end, scanning transmission electron microscopy (STEM) is applied after oxidizing $Ti_{0.12}Al_{0.21}B_{0.67}$ coatings up to 900 °C for 8 h and after annealing at 1000 °C for up to 3 h. The scale layer formed upon oxidation is amorphous at 700 °C consisting of Al, O and B and is made up of (nano-)crystalline $Al_5(BO_3)O_6$ upon oxidation at 900 °C for 8 h. Simultaneously, spinodal decomposition takes place in the unoxidized coating resulting in the formation of Ti- and Al-rich diboride regions. Chemical environment dependent density functional theory (DFT) envelope calculations of the energies required for mass transport on the metal sublattice show a significantly lower activation energy of diffusion for Al atoms in comparison to Ti atoms. Al diffusion is therefore initiated at a lower temperature leading to the formation of the passivating Al-rich oxide layer. In the unoxidized coating, the concurrent migration of Al and Ti, initiated at 900 °C, is characterized by spinodal decomposition into Al- and Ti-rich regions. Upon annealing at 1000 °C, atom probe tomography (APT) and STEM similarly show spinodal decomposition into Ti- and Al-rich domains taking place. Furthermore, upon longer annealing at 1000 °C, the concentration of Al in the coatings is decreased from 20.9 at.% to 16.8 at.% and 12.5 at.% after 1 and 3 h, respectively. Selective area electron diffraction (SAED) shows the formation of AlB_{12} as the Al-rich diboride domains, that formed due to spinodal decomposition, further decompose into AlB_{12} and liquid Al explaining the loss of Al in the coatings, which was

also observed *in situ* by STEM. While the preferential diffusion of Al enables the superior oxidation behavior of $Ti_{0.12}Al_{0.21}B_{0.67}$, spinodal decomposition and the subsequent decomposition of Al-rich diboride regions limit their application to temperatures < 1000 °C.

In the second part, a contactless autonomous health tracking method of ceramic coatings is demonstrated. Changes in contactless eddy current resistivity measurements of amorphous $Cr_{0.34}Al_{0.31}B_{0.35}$ coatings reveal the formation and grain growth of Cr_2AlB_2 and Cr_3AlB_4 as well as their subsequent decomposition into CrB and CrB_2. Upon annealing up to 800 °C, contact-based *in situ* resistivity measurements revealed the phase formation of the MAB phases Cr_2AlB_2 and Cr_3AlB_4, whereby M stands for an early transition metal, A for an A group element and B for Boron, as well as their grain growth. The analysis was verified by *in situ* and *ex situ* SAED and STEM analysis as well as differential scanning calorimetry (DSC), X-ray diffraction (XRD) and elastic-recoil detection analysis (ERDA). As the contactless resistivity measurements show a maximum deviation of 4 %, the phase changes could be tracked without the need for physical contact. Similarly, at temperatures above 800 °C, both *in situ* contact-based and *ex situ* contactless resistivity measurements show the decomposition of the Cr_2AlB_2 and Cr_3AlB_4 phases into the binary CrB and CrB_2 phases by deintercalation of Al with a maximum deviation of 11 %. The proof of concept of contactless materials health tracking of both, phase transformations and decomposition, enables a more lasting and sustainable material and component usage.

Zusammenfassung

Boridbeschichtungen besitzen außerordentliche Eigenschaften für hohe Temperaturen und extreme Umgebungen aufgrund ihrer hohen thermischen Stabilität, ihres Oxidationsverhalten und mechanischen Eigenschaften, was sie zu passenden Werkstoffkandidaten für eine nachhaltige Industrie macht.

Im ersten Teil werden das Oxidationsverhalten und die thermische Stabilität von stöchiometrischen $Ti_{0.12}Al_{0.21}B_{0.67}$ Beschichtungen untersucht, wobei die zugrundeliegenden atomaren Mechanismen aufgedeckt werden. Dafür wird nach dem Oxidieren von $Ti_{0.12}Al_{0.21}B_{0.67}$ bei bis zu 900 °C für 8 h und nach dem Glühen in Vakuum bei 1000 °C für bis zu 3 h, Rastertransmissionselektronenmikroskopie (STEM) zur Untersuchung eingesetzt. Die Oxidschicht, welche sich beim Glühen in Luft bildet, ist bei 700 °C amorph und besteht aus Al, O und B, wohingegen sie nach dem Glühen in Luft bei 900 °C nach 8 h aus (nano-)kristallinem $Al_5(BO_3)O_6$ besteht. Gleichzeitig erfolgt eine spinodale Entmischung in der unoxidierten Beschichtung, wodurch sich Ti- und Al-reiche Diboridregionen bilden. Dichtefunktionaltheorie-Berechnungen (DFT) in Abhängigkeit der chemischen Umgebung der für Massentransport auf dem metallischen Untergitter benötigten Energien zeigen eine deutlich niedrigere Aktivierungsenergie für die Diffusion von Al-Atomen im Vergleich zu Ti-Atomen. Al-Diffusion tritt dementsprechend bereits bei niedrigeren Temperaturen auf, was zur Bildung einer passivierenden Al-reichen Oxidschicht führt. In der unoxidierten Beschichtung wird die gleichzeitige Migration von Al und Ti, welche bei 900 °C anfängt, durch die spinodale Entmischung in Al- und Ti-reiche Regionen charakterisiert. Glüht man die Schichten bei 1000 °C in Vakuum, so zeigen Atomsonden-Tomographie (APT) und STEM ebenfalls die spinodale Entmischung in Ti- und Al-reiche Regionen. Des Weiteren sinkt die Al-Konzentration in den Schichten bei längerem Glühen bei

1000 °C von 20.9 at.% auf 16.8 at.% nach 1 h und auf 12.5 at.% nach 3 h. Mit Feinbereichselektronenbeugung (SAED) lässt sich AlB_{12} nachweisen, da sich die durch die spinodale Entmischung entstandenen Al-reichen Diboridregionen in AlB_{12} und flüssiges Al zersetzen, wodurch auch der Verlust an Al in der Beschichtung erklärt wird. Dies wurde ebenfalls *in situ* mit STEM beobachtet. Während die bevorzugte Diffusion von Al das herausragende Oxidationsverhalten von $Ti_{0.12}Al_{0.21}B_{0.67}$ ermöglicht, begrenzen die spinodale Entmischung und die folgende Zersetzung der Al-reichen Diboridregionen ihren Einsatz zu Temperaturen < 1000 °C.

Im zweiten Teil wird eine kontaktlose autonome Methode zur Überwachung des Materialzustandes von keramischen Beschichtungen präsentiert. Änderungen in kontaktlosen Wirbelstromwiderstandsmessungen von amorphen $Cr_{0.34}Al_{0.31}B_{0.35}$ Beschichtungen zeigen sowohl Bildung und Kornwachstum von Cr_2AlB_2 und Cr_3AlB_4, als auch ihre darauffolgende Zersetzung in CrB und CrB_2. Beim Glühen bis 800 °C konnte die Phasenbildung der MAB Phasen, wobei M für ein frühes Übergangsmetall, A für ein Hauptgruppenelement und B für Bor steht, Cr_2AlB_2 und Cr_3AlB_4, sowie ihr Kornwachstum durch kontaktbasierte *in situ* Widerstandsmessungen aufgezeigt werden. Die Analyse wurde mit *in situ* und *ex situ* SAED und STEM, sowie mit dynamischer Differenzkalorimetrie (DSC), Röntgenbeugung (XRD) und elastischer Rückstreudetektionsanalyse (ERDA) verifiziert. Da die kontaktlosen Widerstandsmessungen eine maximale Abweichung von 4 % aufweisen, können die Phasenumwandlungen auch ohne physischen Kontakt verfolgt werden. In ähnlicher Weise zeigen sowohl *in situ* kontaktbasierte, als auch *ex situ* kontaktlose Widerstandsmessungen bei einer maximalen Abweichung von 11 % die Zersetzung der Cr_2AlB_2 und Cr_3AlB_4 Phasen bei Temperaturen über 800 °C durch die Deinterkalation von Al. Der Nachweis für die kontaktlose Überwachung des

Materialzustandes für sowohl Phasenumwandlungen als auch Zersetzung ermöglicht eine dauerhaftere und nachhaltigere Nutzung von Materialien und Komponenten.

Preface

The research was supported by funds from the German Research Foundation (DFG SCHN 735/42-1 and 735/47-1). For DFT calculations, computing time was supplied from the Jülich-Aachen Research Alliance (JARA) HPC at the IT Center of RWTH Aachen University under the projects JARA0221 and JARA0151.

The following papers contribute to this thesis:

Paper I, first author

Passivating oxidation behavior of $Ti_{0.12}Al_{0.21}B_{0.67}$ coatings investigated by scanning transmission electron microscopy and chemical environment dependent density functional theory simulations.

S. Lellig, A.H. Navidi Kashani, P. Schweizer, M. Hans, G.K. Nayak, J. Michler, J.M. Schneider

Acta Materialia 285 (2025): 120662.

https://doi.org/10.1016/j.actamat.2024.120662

Paper II, shared first authorship

Temporally-resolved decomposition of $Ti_{0.12}Al_{0.21}B_{0.67}$ thin films at 1000 °C

A.H. Navidi Kashani, S. Lellig, M. Hans, L. Löfler, S. Mráz, P. Schweizer, A. Müller, D. Primetzhofer, J. Michler, J.M. Schneider

Surf. Coat. Technol. 487 (2024) 131026

https://doi.org/10.1016/j.surfcoat.2024.131026

Paper III, shared first authorship

Contactless health monitoring in autonomous self-reporting ceramic coatings

P.J. Pöllmann, S. Lellig, D. Bogdanovski, A.H. Navidi Kashani, D.M. Holzapfel, C. Azina, P. Schweizer, M. Hans, P. Zöll, D. Primetzhofer, S. Kolozsvári, P. Polcik, J. Michler, J.M. Schneider

Nanoscale 17.11 (2025): 6854-6862

https://doi.org/10.1039/D4NR03822C

Paper IV, shared first authorship

Contactless tracking of decomposition in self-reporting ceramic Cr-Al-B coatings

P. J. Pöllmann, S. Lellig, D. Bogdanovski, A.H. Navidi Kashani, D.M. Holzapfel, C. Azina, P. Schweizer, M. Hans, P. Zöll, D. Primetzhofer, S. Kolozsvári, P. Polcik, J. Michler, J.M. Schneider

Advanced Materials Interface (2025): 2500092

https://doi.org/10.1002/admi.202500092

Contribution to the papers

All research questions and scientific strategies were conceived by SL and JMS. The first draft of Paper I was compiled by SL, while the first drafts of Paper II and III/IV were compiled in a shared first authorship with ANK and PJP, respectively. All co-authors contributed to the evaluation and discussion of results as well as to editing the papers.

Paper I: S.L.: Writing – original draft, Visualization, Validation, Software, Investigation, Formal analysis, Data curation, Conceptualization. **A.H.N.K.:** Writing – review & editing, Investigation, Formal analysis, Data curation. **P.S.:** Writing – review & editing, Visualization, Software, Investigation, Formal analysis, Data curation. **M.H.:** Writing – review & editing, Writing – original draft, Visualization, Software, Investigation, Formal analysis, Data curation. **G.K.N.:** Writing – review & editing, Writing – original draft, Visualization, Software, Formal analysis, Data curation. **J.M.:** Writing – review & editing, Supervision, Resources, Funding acquisition, Conceptualization. **J.M.S.:** Writing – original draft, Supervision, Resources, Project administration, Funding acquisition, Conceptualization.

Paper II: A.H.N.K: Writing – review & editing, Writing – original draft, Visualization, Validation, Methodology, Investigation, Formal analysis, Data curation, Conceptualization. **S.L.:** Writing – review & editing, Writing – original draft, Visualization, Validation, Methodology, Investigation, Formal analysis, Data curation, Conceptualization. **M.H.:** Writing – review & editing, Visualization, Validation, Investigation, Formal analysis. **L.L.:** Writing – review & editing, Software, Formal analysis. **S.M.:** Writing – review & editing, Validation, Conceptualization. **P.S.:** Writing – review & editing, Visualization, Validation, Investigation, Formal analysis. **A.M.:** Writing – review & editing, Validation, Investigation, Formal analysis. **D.P.:** Writing – review & editing, Validation, Resources, Investigation, Funding acquisition, Formal analysis. **J.M.:** Writing – review & editing, Validation, Supervision, Resources, Funding acquisition. **J.M.S.:** Writing – review & editing, Validation, Supervision, Resources, Funding acquisition, Conceptualization.

Paper III: P.J.P.: Conceptualization, methodology, formal analysis, investigation (lead), data curation, writing – original draft, and visualization. **S.L.:** Conceptualization, methodology, formal analysis, investigation (lead), data curation, writing – original draft, and visualization. **D.B.:** Investigation, and writing – review and editing. **A.H.N.K.:** Investigation, formal analysis, and writing – review and editing. **D.M.H.:** Investigation, formal analysis, and writing – review and editing. **C.A.:** Investigation, formal analysis, data curation, and writing – review and editing. **P.S.:** Investigation, formal analysis, and writing – review and editing. **M.H.:** Investigation, formal analysis, data curation, and writing – review and editing. **P.Z.:** Investigation and writing – review and editing. **D.P.:** Investigation, formal analysis, writing – review and editing, and funding acquisition. **S.K.:** Resources and writing – VIII review and editing. **P.P.:** Resources and writing – review and editing. **J.M.:** Conceptualization, methodology, funding acquisition, supervision, and writing – review and editing. **J.M.S.:** Conceptualization, methodology, project administration, writing – original draft, supervision, and funding acquisition.

Paper IV: P.J.P.: Conceptualization, methodology, formal analysis, investigation (lead), data curation, writing – original draft, and visualization. **S.L.:** Conceptualization, methodology, formal analysis, investigation (lead), data curation, writing – original draft, and visualization. **D.B.:** Investigation, and writing – review and editing. **A.H.N.K.:** Investigation, formal analysis, and writing – review and editing. **D.M.H.:** Investigation, formal analysis, and writing – review and editing. **C.A.:** Investigation, formal analysis, data curation, and writing – review and editing. **P.S.:** Investigation, formal analysis, and writing – review and editing. **M.H.:** Investigation, formal analysis, data curation, and writing – review and editing. **P.Z.:** Investigation and writing – review and editing. **D.P.:** Investigation, formal analysis, writing – review and editing, and funding acquisition. **S.K.:** Resources and writing – review and editing. **P.P.:** Resources and writing – review and editing. **J.M.:** Conceptualization, methodology, funding acquisition, supervision, and writing – review and editing. **J.M.S.:** Conceptualization, methodology, project administration, writing – original draft, supervision, and funding acquisition.

Publications related to the topic of the thesis:

Paper V

Morphology, mechanical properties, and oxidation behavior of stoichiometric $Ti_{0.33-x}Al_xB_{0.67}$ coatings (x = 0.04, 0.15, 0.21, and 0.28)

A.H. Navidi Kashani, M. Hans, S. Lellig, D.M. Holzapfel, L. Löfler, S. Mráz, D. Primetzhofer, J. Michler, J.M. Schneider

Acta Mater. 270 (2024) 119829

https://doi.org/10.1016/j.actamat.2024.119829

Paper VI

Metastable phase formation of (Mo,Cr)2AlB2 MAB phase thin films revealed by theory and experiments

P.J. Pöllmann, D. Bogdanovski, S. Lellig, P. Schweizer, M. Hans, C. Azina, S. Karimi Aghda, P. Zöll, D.M. Holzapfel, D. Primetzhofer, S. Kolozsvári, P. Polcik, J. Michler, J.M. Schneider

Mater. Res. Lett. 12 (2024) 58-66

https://doi.org/10.1080/21663831.2023.2292054

Paper VII

Improved oxidation behavior of $Hf_{0.11}Al_{0.20}B_{0.69}$ in comparison to $Hf_{0.28}B_{0.72}$ magnetron sputtered thin films.

P. Kümmerl, S. Lellig, A.H. Navidi Kashani, M. Hans, P.J. Pöllmann, L. Löfler, G.K. Nayak, D.M. Holzapfel, S. Kolozsvári, P. Polcik, P. Schweizer, D. Primetzhofer, J. Michler, J.M. Schneider

Scientific reports 14.1 (2024): 21653.

https://doi.org/10.1038/s41598-024-72134-3

Paper VIII

Comparative Oxidation Behavior of Columnar and Equiaxed Cr_2AlC Coatings

D.J. Ramesh, M. Hans, S. A. Salman, S. Lellig, D. Primetzhofer, J. Michler, J. M. Schneider

Available at SSRN 5154477.

http://dx.doi.org/10.2139/ssrn.5154477

Other Publications:

Paper IX

A run-time reconfigurable Ge field-effect transistor with symmetric on-states

A. Fuchsberger, L. Wind, D. Nazzari, L. Kühberger, D. Popp, J. Aberl, E. Prado Navarrete, M. Brehm, L. Vogl, P. Schweizer, S. Lellig, X. Maeder, M. Sistani, W.M. Weber

IEEE J. Electron. Devices Soc. 12 (2024) 83-87

https://doi.org/10.1109/JEDS.2024.3350209

Paper X

A reconfigurable Ge transistor functionally diversified by negative differential resistance.

A. Fuchsberger, L. Wind, D. Nazzari, L. Kühberger, A. Dobler, J. Aberl, E. Prado Navarrete, M. Brehm, L. Vogl, P. Schweizer, S. Lellig, X. Maeder, M. Sistani, W.M. Weber

IEEE Journal of the Electron Devices Society (2024).

https://doi.org/10.1109/JEDS.2024.3432971

Acknowledgments

Ich möchte zuerst meinen beiden Betreuern, meinem Doktorvater Professor Jochen M. Schneider und Professor Johann Michler für Ihr Vertrauen und die Möglichkeit bedanken, meine Promotion am Institut Materials Chemistry der RWTH Aachen und gleichzeitig am Laboratory of Mechanics of Materials and Nanostructures der Empa absolvieren zu können. Eure Anleitung, Rat und Hilfe haben mir geholfen mich immer weiterzuentwickeln und ein besserer Wissenschaftler zu werden.

Des Weiteren gilt ein besonderer Dank Dr. Peter Schweizer, von dem ich nicht nur die Grundlagen des TEMs lernen durfte, sondern viele weitere Prinzipien des wissenschaftlichen Arbeitens.

Ganz besonders möchte ich mich dazu bei Peter und Amir bedanken. Die Zusammenarbeit mit euch war nicht nur sehr produktiv, sondern hat vor allem auch echt viel Spaß gemacht!

Für ihre wissenschaftliche Expertise und Hilfe in verschiedensten Bereichen möchte ich mich zudem bei Marcus, Stano und Ganesh bedanken.

Das Arbeiten am MCh und an der empa ist durch die enge und offene Zusammenarbeit gekennzeichnet, wofür ich mich bei allen aktuellen und ehemaligen MCh und empa Mitgliedern bedanken möchte, insbesondere Eva, Sameer, Janani, Pauline, Deborah, Subisha, Markus, Héloïse, Janis, Matej, Soheil, Damian, Stephan, Simon, Fedor, Maria, Barbara, Krzysztof und Hendrik.

Für die zuverlässige und schnelle Unterstützung in allen organisatorischen Fragen möchte ich mich bei Gabi, Simon und Eveline bedanken.

Zu guter Letzt gilt mein großer Dank meiner Verlobten Anna, meinen Eltern und meiner Schwester, sowie meinen Freunden, insbesondere Michael. Vielen Dank für eure Unterstützung und Hilfe in allen Situationen, ich kann euch gar nicht genug danken.

Table of Contents

1 Introduction

A responsible and sustainable materials consumption is necessary to enable a future-proof industry. In order to achieve this goal, the lifetime of materials and components has to be improved. Therefore, two main objectives need to be addressed, on the one hand improving the materials properties and on the other hand tracking the materials health to increase the length of their lifecycle. Boride coatings show desired properties for both of these approaches. Transition metal diborides are well suited as protective coatings for extreme environment applications due to their exceptional thermal stability and mechanical properties [1, 2]. MAB phases, whereby M stands for an early transition metal, A for an A group element and B for Boron, also show promising properties like oxidation resistance [3, 4], thermal stability [5] and low electrical resistivity [5] and are therefore a suitable candidate as a self-reporting material.

Titanium diboride (TiB_2) is one of the most extensively studied transition metal diborides, whereby it is often used as a protective coating for e.g. cutting tools [6-8]. In contrast to its extraordinary thermal stability, the oxidation resistance of TiB_2 coatings is improvable as they form an oxide scale consisting mostly of B_2O_3 and TiO_2 upon oxidation at temperatures > 400 °C [9]. The scale becomes porous and depleted of B due to the evaporation of volatile B_2O_3 at 500 °C [10] as well as up to temperatures ranging from 950 to 1100 °C [11]. In order to improve the oxidation resistance, Al has been added to TiB_2 coatings successfully decreasing the oxidation rate [9, 10, 12-14]. Comparing the oxidation behavior of over-stoichiometric $TiB_{2.4}$ with B-deficient $Ti_{0.68}Al_{0.32}B_{1.35}$ at 700 °C for 1 h, Bakhit et al. [10] found a significantly lower oxide scale thickness upon addition of Al. They ascribed the improvement to the formation of a dense Al containing oxide layer, that was X-ray amorphous, which formed beneath an outer, porous layer, whereby the absence of a B-rich tissue phase in the grain boundaries for the Al-containing diboride has to be taken into account as well. The influence of the presence of a tissue phase and subsequently the B concentration on the oxidation behavior was further analyzed by Thörnberg et al. [13]. Hereby, the absence of a boron-rich tissue phase in $Ti_{0.9}Al_{0.1}B_{1.3}$ lead to a lower oxide scale thickness of ~ 140 nm after oxidation at 600 °C for 10 h in comparison to ~ 320 nm for the tissue phase containing $Ti_{0.9}Al_{0.1}B_{1.9}$. A more systematic approach to investigate the oxidation behavior and mechanical properties with regard to the B concentration was done by Navidi et al. [12], who varied the B content of $(Ti_{0.35}Al_{0.65})B_y$ thin films between $y = 1.7$ (under-stoichiometric), $y = 2$ (stoichiometric) and $y = 2.4$ (over-stoichiometric). While the over-stoichiometric sample possessed an oxide scale of 204 ± 16 nm after oxidation for 8 h at 700 °C, both the stoichiometric and under-stoichiometric samples showed a superior oxidation behavior with oxide thicknesses of 39 ± 7 nm and 40 ± 4 nm, respectively. This was attributed to the absence of a B-rich tissue phase as well as the oxide scale consisting mostly of Al and O. Considering both oxidation resistance and mechanical properties, the stoichiometric $(Ti_{0.35}Al_{0.65})B_2$ clearly outperforms the other two [12]. In a following study, Navidi et al. [15] also investigated the influence of the Al content on the oxidation behavior of stoichiometric $Ti_{0.33-x}Al_xB_{0.67}$ coatings with x = 0.04, 0.15, 0.21, and 0.28. While upon oxidation up to 900 °C for 8 h, samples with $x \geq 21$ at.% showed an X-ray amorphous oxide scale consisting mostly of Al and O with passivating behavior, coatings with $x \leq 15$ at.% possessed a non-passivating, crystalline oxide scale containing Al and Ti as well as pores [15].

Self-reporting materials, whereby the material itself functions as a sensor reporting on its current health status, help to significantly increase components or materials lifetime. A detailed knowledge of the current status of the material reduces the need for safety factors, generally defining the lifetime of a component, whereby the component is taken out of commission significantly before its actual end of lifetime [16, 17]. Generally, an easily measurable property of a self-reporting material correlated to structural or chemical properties can be used to assess the current health status [18]. Self-reporting materials can e.g. report on scratches in metals [19], crack formation [20-26] and mechanical loading [21, 27-31] by the change of various properties including color [20, 21, 27, 32], photoluminescence [19, 21, 28-31] as well as electrical resistance [22-26], whereby the materials include polymers [27-29], composites [21, 30] and ceramics [31]. In addition to single phase self-reporting materials, a secondary sensor phase can be introduced into the material reporting on electrical degradation or chemical changes in polymers [33], composites [34-36] and ceramics [18]. Previously, Stelzer et al. showed the self-reporting properties of Cr_2AlC in measuring the contact-based electrical resistivity and thereby tracking phase changes of amorphous Cr_2AlC to an ordered crystalline structure upon annealing in vacuum [37].

In the first part of the thesis, the atomic scale mechanism explaining the extraordinary oxidation behavior are illustrated, also demonstrating the limitations and thermal stability of stoichiometric $Ti_{0.12}Al_{0.21}B_{0.67}$ coatings. To that end, high-resolution studies of $Ti_{0.12}Al_{0.21}B_{0.67}$ coatings, that were oxidized up to 900 °C for 8 h as well as annealed in vacuum up to 1000 °C for 3 h, have been conducted. Transmission electron microscopy (TEM) in combination with energy X-ray dispersive spectroscopy (EDX) mappings and atom probe tomography (APT) were rationalized by density functional theory (DFT) statistical envelope calculations [38, 39] unraveling the activation energy of diffusion explaining both the oxidation behavior as well as thermal stability of stoichiometric $Ti_{0.12}Al_{0.21}B_{0.67}$ coatings.

In the second part, a method for contactless tracking of materials health of $Cr_{0.34}Al_{0.31}B_{0.35}$ coatings by contactless eddy current resistivity measurements is outlined. Without the necessity of physical contact, the changes in electrical resistivity allow conclusions to be drawn on phase transitions, chemical changes as well as the decomposition of the formed MAB phases. The proof of concept enables the future use of the proposed contactless method to significantly increase components lifetime and reduce the materials waste. The *in situ* contact based and *ex situ* contactless resistivity measurements are verified by high-resolution and well-established methods including *in situ* and *ex situ* scanning transmission electron microscopy (STEM) measurements, selected area electron diffraction (SAED), differential scanning calorimetry (DSC), X-ray diffraction (XRD) and DFT.

2 Methods

2.1 Magnetron Sputtering

Magnetron sputtering is a well-known physical vapor deposition (PVD) technique. The setup of magnetron sputtering is the following: In a vacuum chamber, a target with the to be deposited materials functions as a cathode, while the to be coated substrate is located opposite to it. The gap in between is filled with a sputtering gas [40, 41]. While the generated magnetron plasma is most commonly made up of the inert Ar, reactive gases, like O, C or N can also be used in a process called reactive sputtering [42]. When a negative voltage is applied at the cathode, electrons are repelled from the cathode and accelerated towards the sputtering gas creating positively charged ions of the sputtering gas atoms [43]. These ions are accelerated towards the target generating secondary electrons upon hitting it, which themselves are pushed away from the cathode generating more ions in the sputtering gas. With the process repeating, more and more secondary electrons and subsequently gas ions are generated. Simultaneously, atoms of the target materials are ejected travelling to the substrate, where they condense and form the desired thin film or coating. This happens due to collision cascades taking place in the target material by collision with an excited particle transferring part of its energy to a target atom, which itself hits neighboring atoms. Such a collision cascade can then end with a surface atom receiving significant momentum and being ejected from the target [44]. While this process is similar for diode sputtering, the advantage of magnetron sputtering lies in the addition of magnets positioned behind the target generating a static magnetic field confining the electrons to the vicinity of the cathode. Due to their extended lifetime, the confined electrons ionize a larger quantity of gas atoms resulting in an increased deposition rate and lowered discharge voltage [44].

The advantages of magnetron sputtering lie in the extremely high cooling rates [45] and its high versatility as nearly all metals and compounds can be produced [46]. Furthermore, the properties can be finely adjusted by tuning various parameters including target power, working pressure, sputtering gas or deposition temperature.

2.2 X-ray Diffraction

To analyze the structure of a crystalline sample, X-ray diffraction (XRD) is used [47]. Monochromatic X-rays irradiate the crystalline sample at an angle θ. Thereby, constructive interference between the X-rays scattered from the crystal lattice, can be observed if the Bragg’s equation is fulfilled:

$$2\,d\,sin(\theta) = n\,\lambda$$

whereby d equals to the lattice parameter, n to an integer related to the reflection order and λ to the wavelength of the X-ray. With XRD, the structure, texture, phases, lattice constants and residual stresses can be characterized [47].

2.3 Energy Dispersive X-Ray Spectrometry

Energy Dispersive X-Ray Spectrometry (EDX(S)) is used for the qualitative and quantitative elemental analysis of a material [48]. X-rays characteristic for each element are generated by an electron beam exciting the sample. Thereby, the critical ionization energy needs to be surpassed leading to the ionization of an atomic shell by an electron leaving the shell, generating an electron hole. An electron from a higher energy level fills this electron hole. The energy differences between the electron shells is released as characteristic X-rays, which are collected with the help of a semiconductor detector [48, 49]. In a qualitative analysis, the generated characteristic peaks are assigned to the corresponding elements [48]. To quantitatively determine the chemical composition of the probed material, peak fitting is employed, whereby ZAF matrix corrections are used, with Z relating to the atomic number, A to absorption and F to fluorescence [48].

2.4 Differential Scanning Calorimetry

Differential scanning calorimetry (DSC) is used to track chemical or phase changes in a material upon heating or cooling. To that end, a sample, in this case in powder form, is heated at a constant rate, while an empty crucible serves as a reference cell. The difference in heat supplied or emitted is tracked in the heat flow as function of the temperature [50].

2.5 Resistance Measurements

Contact-based resistance measurements were carried out based on the van-der-Pauw method, which is valid for arbitrary shaped, flat samples with a homogeneous thickness [51, 52]. Four contacts are positioned on the circumference of the sample. The resistance R_1 is based on the potential difference $V_3 - V_4$ between point 3 and 4 for a current $i_{1\text{-}2}$ flowing between points 1 and 2 [51, 52]:

$$R_1 = \frac{V_4 - V_3}{i_{1-2}}$$

Repeating the process with a different couple of pairs of the four contacts gives the resistance R_2. With d being the thickness of the sample and f a geometric factor dependent on the ratio R_1/R_2 [53], that can be solved numerically, the electrical resistivity ρ is given by the formula below [51, 52].

$$\rho = \frac{\pi d}{ln2} \frac{(R_1 + R_2)}{2} f$$

The here used setup has been described in [37] and [18] and consisted of four Pt contacts, that were clamped with ceramic clamps.

For contactless resistivity measurements, eddy currents are induced by the proximity of an electromagnetic field that is generated by an excitation coil. The eddy currents themselves create an electromagnetic field oppositionally directed to the prior field altering the impedance of it. The change is dependent on the geometry of the setup, the conductivity, composition, morphology and surface of the sample. Changes in the material lead to a change in the impedance. While eddy current measurements are limited to conductive materials, their advantages include short measurement times and a high sensitivity to changes in the materials [54, 55].

2.6 Focused Ion Beam Techniques

In order to prepare lamellae with dimension of 10 µm in length and less than 100 nm in width that can be used for further analytical methods, focused ion beam (FIB) milling in combination with a scanning electron microscope (SEM) is used. While liquid metal ion sources (LMIS) generate Ga ions, plasma sources mostly work with an inert gas as Xe, Ne or Ar [48]. The so generated ions are accelerated to the sample and focused with the help of high-voltage, electrostatic lenses. In addition to imaging, which is done via secondary electrons that are produced by the ions in the sample material, the ion beam can be used for milling by sputtering, which is utilized in the lamellae preparation process [48]. After the deposition of a protective layer, often Pt, the lamellae is milled with an accelerating voltage of 30 kV, removed with the help of a nanomanipulator and subsequently thinned with 30 kV and polished with 5 kV to a thickness of less than 100 nm [48].

2.7 Transmission Electron Microscopy

A transmission electron microscope (TEM) is used to investigate the morphology, structure and chemical composition down to the atomic level [56]. Today, it is mostly composed of a field emission electron source emitting an electron beam with an acceleration voltage in a range between 2 – 400 kV that is focused using electromagnetic lenses. In order to further reduce lens defects, spherical C_S as well as chromatic C_C aberration are corrected in modern TEMs by using complex systems of quadrupole and octupole lenses for C_s correction and monochromators or energy-filtering for C_C correction [56]. Samples that are investigated can be prepared conventionally or by FIB and should possess a thickness of < 100 nm. Alternatively, TEM or TEM heating chips can be deposited with a coating < 100 nm. For imaging a sample, two main modii are differentiated. Using a lenses setup that results in parallel beams hitting the specimen, it is referred to as (conventional) TEM, while using a converged electron beam, that scans over the specimen, it is referred to as scanning transmission electron microscopy (STEM) [56]. TEM images are simply projected on a viewing screen and captured with a camera positioned in the image plane. In the case of a direct beam, a bright field (BF) image is created, while selecting scattered beams results in dark field (DF) images, which is done by using an objective aperture. For STEM images, a digital image is created from an electron detector upon scanning the specimen. The most common STEM images that are produced in a TEM are high-angle annular dark-field (HAADF) images supplying a Z-contrast, but also BF and DF images are possible [56].

In order to receive chemical information of a sample close to the atomic level, TEMs are often equipped with an EDX detector, which works similarly as described in 2.3, but with a significantly higher spatial resolution due to the focused electron beam and higher counts for elemental mapping due to the high acceleration voltage.

In order to receive structural information, selected electron area diffraction (SAED) is used, whereby the electron beam is diffracted from the crystal lattice, similarly to the X-rays in 2.2. Thereby, smaller crystal sizes can be probed due to the significantly smaller spot sizes [56].

2.8 Atom Probe Tomography

Atom probe tomography (APT) is used to generate elemental maps of the chemical composition that are three dimensional [57, 58]. Thereby, the spatial resolution is in the sub-nanometer range. The imaging is based on field ion microscopy, whereby a high voltage applied to a needle-shaped specimen, which leads to the evaporation of the specimen as an electrostatic field is generated. In addition, time-of-flight mass spectrometers supply further data on the evaporated particles [58]. The specimen are prepared by FIB and generally have a diameter at the tip of less than 100 nm [59, 60]. Laser pulses as well as voltage pulses can be used to set off the field evaporation. A position-sensitive detector is made up of microchannel plates that turn the ions into electrons that can then be collected by an anode [57, 58]. Thereby, data on the evaporated atoms can be collected and reconstructed in a 3D map giving insight on the atomic coordinates and mass-to-charge ratio [57].

2.9 Ion Beam Analysis

In both, Rutherford backscattering spectrometry (RBS) as well as elastic recoil detection analysis (ERDA), the elastically scattered ions from the nuclei of the sample are analyzed [61] enabling the determination of the composition of the sample. In the case of RBS, a light monoenergetic ion beam, e.g. He, is used and the backscattered ions are counted with their energies being measured using a solid-state particle detector. Thereby, the energies of the backscattered ions are correlated to the mass of the sample, while the amount of the ions gives an insight into their concentration. For ERDA, heavier ions are used with a glancing incident angle, whereby the energy of the recoiling sample nucleus is quantified. ERDA is specifically helpful for measuring light elements in combination with heavier ones [61].

2.10 DFT Calculations

Density functional theory (DFT) is a computational approach utilizing quantum mechanics, which is in principle dependent on solving the Schrödinger equation [62, 63]. As it is based on the fundamental Hamiltonian without utilizing any external or experimental information as input, it is referred to as an *ab initio* or *first principles* approach [62]. In order to determine the ground state energy of a system, Hohenberg and Kohn [64] proved that the external potential of a system is uniquely determined by the electron density. Thereby, the ground state energy and density is a function of the universal functional electron density, making only the solution of a single-particle problem necessary [64, 65]. The electron density again can be calculated with the help of the Kohn-Sham equations [66]. DFT calculations can be used to calculate various materials properties like hardness, shear and bulk modulus or phase stability [65].

3 Passivating Oxidation Behavior of $Ti_{0.12}Al_{0.21}B_{0.67}$ Coatings Investigated by Scanning Transmission Electron Microscopy and Chemical Environment Dependent Density Functional Theory Simulations

3.1 Introduction

Due to their outstanding thermal stability, transition metal diborides (TMB_2) are employed in (ultra) high-temperature applications [67-69]. For example, titanium diboride (TiB_2) has been extensively studied as a protective coating material for cutting tools [6-8], whereby temperatures may exceed 1000 °C at the cutting edge [70], protective shields for space applications [71] or as a functionally graded armor ceramic [72] due to its melting point of > 3000 °C [73], exceptional thermal stability [1, 2] and outstanding mechanical properties [1, 2, 74, 75]. The application of TiB_2 as a cathode material for aluminum electrolysis with temperatures up to 1400 °C [76-79] and its potential use as a protective coating for metallic bipolar plates in proton-exchange membrane fuel cells (PEMFCs) [80] is enabled by the considerable chemical stability and corrosion resistance [69, 80-82]. However, during exposure to atmosphere at elevated temperatures the oxidation behavior of bulk TiB_2 was reported by Cai et al.

[83] to be highly dependent on the configuration of the scale. Compared to 650 °C, the oxidation rate at 500 °C increased considerably which was attributed to be due to the formation of an Ti-B-O amorphous inner layer dual phase top layer containing amorphous B_2O_3 and rutile TiO_2. At 800 °C, a scale thickness of approximately 10 µm is measured after 1 hour of oxidation [83].

Hexagonal TiB_2 (space group P6/mmm) thin films were produced by magnetron sputtering, possessing a columnar nanostructure [2]. The formation of an amorphous, boron-rich tissue phase located between column boundaries was observed for thin films with an excess of boron [2]. It was reported that the tissue phase leads to a significant increase in hardness from 43.4 ± 0.8 GPa ($TiB_{1.97}$) [75] to > 60 GPa ($TiB_{2.4-3.2}$) [2]. Furthermore, Fuger et al. report a significant hardness-anisotropy for TiB_z films with z varying from 2.07 to 4.42 based on an increase in film hardness of > 10 GPa with increasing {0001} fraction [84].

Upon oxidation, the scale formed is mostly composed of B_2O_3 and TiO_2, whereby oxidation is initiated at 400 °C [9]. At 500 °C, Bakhit et al. reported that $TiB_{2.4}$ films, containing a B-rich tissue phase, formed B-deficient and porous scales, which was attributed to evaporation of volatile B_2O_3 [10]. Similarly, Voitovich et al. observed a decrease in the amount of B_2O_3 in comparison to TiO_2 in the scale after oxidation in the temperature range of 950 to 1100 °C [11].

It has been shown, that the addition of Al to TiB_2 thin films leads to a significant reduction of the oxide scale thickness [9, 10, 12-14] and a concurrent decrease in both, hardness and Young’s modulus in comparison to TiB_2 [10, 85, 86].

With regard to thermal stability of a $(Ti_{0.71}Al_{0.29})B_{3.08}$ coating, Mockuté et al. observed phase separation after annealing at 1000 °C for 1 h. The formation of Ti-deficient crystallites observed within (Ti,Al)B_2 columns, which are in turn embedded in the B-rich tissue phase, was ascribed to be due to nucleation and growth via grain boundary diffusion and surface-directed decomposition [87].

Bakhit et al. [10] compared the oxide scale thickness formed on over-stoichiometric $TiB_{2.4}$, containing a B-rich tissue phase, with B-deficient $Ti_{0.68}Al_{0.32}B_{1.35}$ after oxidizing at 700 °C for 1 h. The authors attributed the improved oxidation behavior to be due to the formation of an X-ray amorphous, dense oxide layer containing Al, hindering coarsening of the oxide, below a more porous outer layer. Additionally, it was reported that the film containing Al possessed Ti-rich grain boundaries encapsulated in an Al-rich and B-deficient tissue phase in contrast to the B-rich $TiB_{2.4}$ film exhibiting a B-rich tissue phase [10]. Hence, it is reasonable to assume that the improved oxidation behavior in $Ti_{0.9}Al_{0.1}B_{1.3}$ compared to $TiB_{2.4}$ is due to the combined effect of Al incorporation and the lack of a B-rich tissue phase.

The influence of the B concentration on the oxide scale formation during oxidation at 600 °C for 10 h was studied by Thörnberg et al. [13]. They investigated $Ti_{0.9}Al_{0.1}B_{1.9}$, exhibiting a B-rich tissue phase, despite the under-stoichiometric composition, and $Ti_{0.9}Al_{0.1}B_{1.3}$, without a tissue phase, and observed oxide scales composed of a TiO_2 and Al_2O_3-TiO_2 double layer with thicknesses of ~320 nm and ~ 140 nm, respectively. Additionally, B_2O_3 was suggested to be present at the interface between the two oxide layers [13]. The improvement in the oxidation resistance of $Ti_{0.9}Al_{0.1}B_{1.3}$ compared to $Ti_{0.9}Al_{0.1}B_{1.9}$ was attributed to the absence of the boron-rich tissue phase in the more B-deficient film [13].

Navidi et al. [12] systematically investigated the influence of deviations from stoichiometry on oxidation behavior and mechanical properties of $(Ti_{0.35}Al_{0.65})B_y$ thin films considering besides y = 2.0 over- (y = 2.4) and under-stoichiometric (y = 1.7) compositions. $(Ti_{0.35}Al_{0.65})B_{2.0}$ possessed an elastic modulus of 395 ± 12 GPa, which was higher than the moduli of the B-rich $(Ti_{0.34}Al_{0.66})B_{2.4}$ and the B-deficient $(Ti_{0.36}Al_{0.64})B_{1.7}$ with 330 ± 9 GPa and 274 ± 16 GPa, respectively. This trend is in good agreement with ab-initio calculations resulting in theoretical values for the elastic modulus of 253 GPa for the B-deficient $(Ti_{0.36}Al_{0.64})B_{1.7}$ and 353 GPa for stoichiometric $(Ti_{0.35}Al_{0.65})B_{2.0}$ coating. The lower elastic modulus for the B-deficient compositions can be rationalized by bond weakening as witnessed by composition induced changes in cohesive energy. The elastic modulus reduction for the B-rich coating reported in [12] was, consistent with Nedfors et al. [86], ascribed to the presence of B-rich tissue phase.

The stoichiometric $(Ti_{0.35}Al_{0.65})B_{2.0}$ thin film reported [12] showed an oxide scale consisting mostly of Al and O and a thickness of 39 ± 7 nm, which was similar to the B-deficient sample (40 ± 4 nm) in comparison to 204 ± 16 nm for the B-rich $(Ti_{0.34}Al_{0.66})B_{2.4}$ coating after oxidizing at 700 °C for 8 h, clearly outperforming titanium aluminum nitride coatings with a similar Al/Ti ratio. The considerable reduction in oxidation resistance observed for the B-rich coating was attributed, in line with Bakhit et al. [10], to be due to the presence of boron-rich tissue phases. Overall, the stoichiometric $(Ti_{0.35}Al_{0.65})B_{2.0}$ coating composition proved superior in comparison to both, the B-rich and the B-deficient coatings, when oxidation resistance and mechanical behavior are considered jointly [12]. Navidi et al. [15] revealed the influence of the Al content in stoichiometric $Ti_{0.33-x}Al_xB_{0.67}$ coatings with x = 0.04, 0.15, 0.21, and 0.28 upon oxidation at temperatures up to 900 °C for 8 h. For $x \geq 21$ at.%, the formation of a passivating, X-ray amorphous oxide scale was observed, while for $x \leq 15$ at.% a non-passivating, crystalline oxide scale was formed. This scale showed besides the presence of pores also Al-rich and Ti-rich oxide regions [15].

While oxidation resistance data for TiB_2 with additions of Al have been reported for temperatures up to 900 °C [22, 24, 30], and the passivation requirements in terms of the Al concentration have been communicated for this temperature range [30], little is known regarding the underlying, atomic scale mechanisms enabling passivating oxidation behavior of stoichiometric $(Ti,Al)B_2$ coatings.

Here, high-resolution studies have been performed before and after oxidation of $Ti_{0.12}Al_{0.21}B_{0.67}$ coatings. Specifically, transmission electron microscopy (TEM) analyses including energy X-ray dispersive spectroscopy (EDX) mappings and scanning transmission electron microscopy (STEM) as well as atom probe tomography (APT) were utilized to analyze changes in local chemical composition occurring during scale formation upon oxidation at 700, 800 and 900 °C for up to 8 h. The temporal evolution of spatially resolved composition and structure data were compared to density functional theory (DFT) statistical envelope calculations [38, 39] of the formation energy of vacancies as well as the activation energy of migration to identify the atomistic mechanisms enabling scale formation.

3.2 Experimental Details

The protocol employed for the synthesis of the boride coatings using magnetron sputtering of two B targets and a $Ti_{0.4}Al_{0.6}$ target in an ultra-high vacuum growth system was described by Navidi et al. [12]. With target power densities of 8.5 W/cm^2 for the B targets and 2 W/cm^2 for the $Ti_{0.4}Al_{0.6}$ target, a composition of 11.6 ± 1.2 at.% Ti, 21.4 ± 2.2 at.% Al and 67.0 ± 3.4 at.% B, based on elastic recoil detection analysis (ERDA), was obtained and is henceforth referred to as stoichiometric $Ti_{0.12}Al_{0.21}B_{0.67}$ [12].

Different $Ti_{0.12}Al_{0.21}B_{0.67}$ coatings were oxidized in ambient air at 700 °C for 1, 4 and 8 h as well as for 8 h at 800 and 900 °C in a GERO (SR70-200/12) tube furnace. To this end, an Al_2O_3 crucible containing one sample was introduced together with a Ni/Ni-Cr thermocouple located on the same height as the crucible into the pre-heated furnace and removed after the corresponding oxidation time.

For the structural and chemical analysis of the coatings, STEM imaging, selected area electron diffraction (SAED) as well as EDX mapping were performed using a Thermo Fisher Scientific Titan Themis 200 G3 equipped with a SuperX detector. Therefore, lamellae were prepared by focused ion beam (FIB) milling using a FEI Helios Nanolab 660 dual-beam microscope as well as a Tescan Lyra FIB/scanning electron microscope (SEM), whereby Pt was deposited as a protective layer. The lamellae were thinned to around 50 nm and polished with a voltage of 5 kV. The oxide scale thickness values are based on 10 individual measurements and the scale thickness range given corresponds to one standard deviation. For the chemical composition ranges determined by EDX within a region of interest, average values are given as well as the minimum and maximum values for each line scan.

Three-dimensional chemical composition analysis at the nanometer scale was carried out by APT and specimens were prepared in plan-view lift-out geometry (see supplementary information of [38]) at a distance of ~300 nm from the surface/interface of the unoxidized coating region. This lift-out geometry was chosen in order to maximize the number of grain boundaries as the coatings exhibit columnar grains. Atom probe specimens were prepared by FIB techniques using the FEI Helios Nanolab 660 dual-beam microscope according to a standard protocol [88]. Low voltage cleaning at 5 kV and 40 pA has been carried out for 10 minutes in order to achieve needle-like specimens with radius and shank angle of < 30 nm and < 10°, respectively. Field evaporation was done using a CAMECA local electrode atom probe (LEAP)4000X HR and assisted by thermal pulsing with a UV laser at 50 pJ pulse energy, 125 kHz laser pulse frequency, 60 K base temperature and the detection rate was set at 0.5%. While 10 million ions could be acquired for the coating oxidized at 700 °C for 8 h, only 1 million ions were collected for the as deposited coating and for the coating oxidized at 900 °C for 8 h due to premature fracture of the specimens. Reconstructions and data analysis were done with AP Suite 6.1.

3.3 Computational Details

The vacancy formation energy (E_f) and activation energy of migration (E_b) calculation presented in this work is based on statistical envelope calculations, which were introduced in references [38, 39]). To this end, Ti in hexagonal TiB_2 (space group P6/mmm) is partly substituted by Al. The random $(Ti,Al)B_2$ solid solution configuration was obtained with the special quasi-random structure (SQS) method [89]. To mimic the desired experimental composition, i.e., $Ti_{0.12}Al_{0.21}B_{0.67}$, the metal sublattice is populated with 17 Al atoms and 10 Ti atoms in a single-crystal model of $(Ti,Al)B_2$ with a supercell of 3 × 3 × 3.

To calculate E_f and E_b, DFT was used as implemented in the Vienna Ab initio Simulation Package (VASP) [90, 91]. Generalized Gradient Approximations (GGA)-Perdew-Burke-Ernzerhof (PBE) [92] parametrization has been used to describe the electron-electron exchange and correlation interactions. The pseudo-potentials used for each of the elements in the calculations treat any semi-core states as valence, and the recommended potential is used as per the VASP website recommendation. The ion-electron interactions were described using the projector augmented wave method [93], with a plane-wave energy cut-off of 500 eV. The corresponding Brillouin zone was with 7 × 7 × 7 Monkhorst–Pack k-point mesh [94]. The Methfessel–Paxton [95] smearing of 0.2 eV was applied. A convergence criterion of 10^{-6} eV (per supercell) was used for the total energy during the electronic self-consistency cycles and ionic relaxations during structural optimizations, and the total energy convergence of 10^{-4} eV (per supercell) was applied. All calculations were non-magnetic.

First, a vacancy was created at each of the 81 sites (27 metal, 54 non-metal) and E_f is calculated separately as $E_f = E_i - E_0 + \mu_i$, where E_i and E_0 are the total energy of the supercell with and without the vacancy, respectively, and μ_i is the chemical potential of the species *i*. The chemical potential for each species was conventionally set equal to the energy-per-atom of the corresponding element in its stable solid structure. E_b was calculated using the nudged elastic band (NEB) method [96]. The envelope approach [38, 39] is designed so that the migrating atom diffuses to another vacant site only if that site was occupied by the same species in the parent (vacancy-free) supercell, see Figure 1. Here, it can be seen that depending on the trajectory, the chemical environment differs, which in turn affects the magnitude of E_b. Also, the energy required to form a vacancy is chemical environment dependent. The variability induced by changes in chemical environment for both energies are collected in the envelope for each element. The cells were relaxed regarding size, shape, and atomic positions before vacancy and migration barrier calculations.

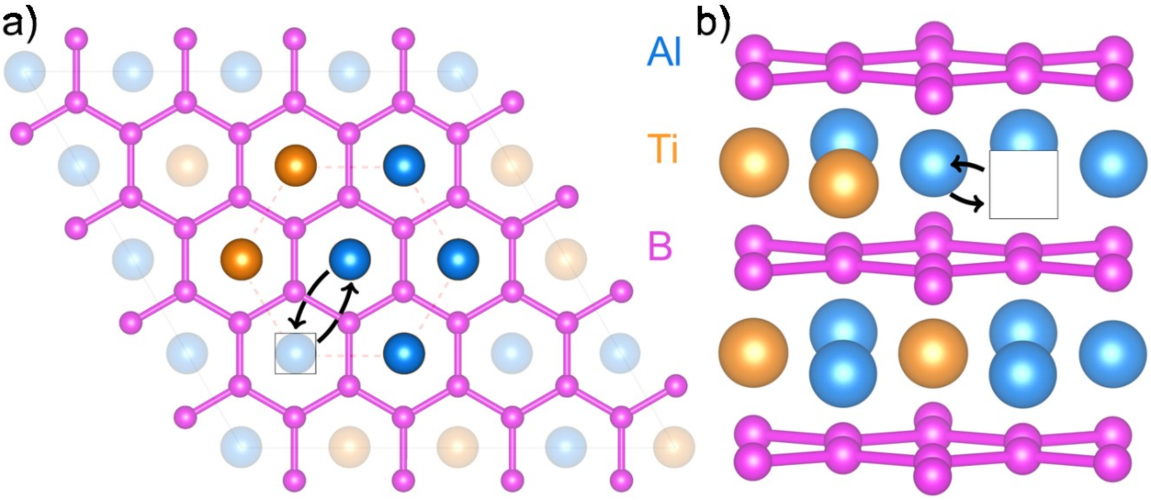

Figure 1. Schematic representation of the chemical environment around the diffusing Al atom (in the middle) to its adjacent lattice side from the top view (a) and side view (b).

The transition state corresponding to the saddle point along the minimum energy diffusion path was determined using the NEB [96] method implemented in VASP, following the protocol laid out in [97].

3.4 Results and Discussion

To investigate the mechanisms active during oxidation of stoichiometric $Ti_{0.12}Al_{0.21}B_{0.67}$, DFT envelope calculations were conducted. Here, the envelope captures the impact of different chemical environments encountered in the ternary solid solution during vacancy formation and migration. As is shown in Figure 2 (a), the formation energy envelope for vacancies is significantly lower for Al as compared to B and Ti. For the formation of Al vacancies, the minimum and maximum energies required are 0.41 and 0.84 eV/atom, respectively, corresponding to an 0.62 ± 0.22 eV/atom envelope. The corresponding envelopes for Ti and B are 3.37 ± 0.28 and 2.48 ± 0.34 eV/atom, respectively. Hence, on the metal sublattice the formation of Al vacancies is predicted to take place at lower temperatures than the formation of Ti vacancies. Similarly to the vacancy formation predictions, the activation energy of migration is predicted to be lower for Al compared to Ti, see Figure 2 (b). Hereby, the in-plane and out-of-plane movement needs to be differentiated, see Figure 2 (c). In-plane movement describes the transfer from a metal atom to a free vacancy of the same type in the metal lattice. For out-of-plane movement, metal atoms must transit through a B layer, see Figure 2 (c). The energy for migration for out-of-plane movement is significantly higher for Ti with 8.41 ± 0.15 eV/atom than for Al with 4.51 ± 0.19 eV/atom. While in general for the out-of-plane transfer higher activation energies are needed, the activation energy for migration of Al in-plane movement possesses with 1.56 ± 0.31 eV/atom the lowest activation energy for migration range overall in comparison to 4.02 ± 0.41 eV/atom for the Ti in-plane movement, which is slightly below the Al out-of-plane migration energy of 4.51 ± 0.19 eV/atom.

Under the assumption, that the atomic vacancy concentration is zero, the activation energy for diffusion via vacancies (Q_D) can be estimated by $Q_D = E_b + E_f$ [98]. This results in an activation energy for diffusion envelope of 2.19 ± 0.53 eV/atom for Al and 7.38 ± 0.69 eV/atom for Ti, when considering in-plane migration and 5.13 ± 0.41 eV/atom for Al and 11.77 ± 0.43 eV/atom for Ti for out-of-plane migration.

Hence, for both, in-plane and out-of-plane migration scenarios Al diffusion is predicted to be initiated at significantly lower temperatures than Ti migration.

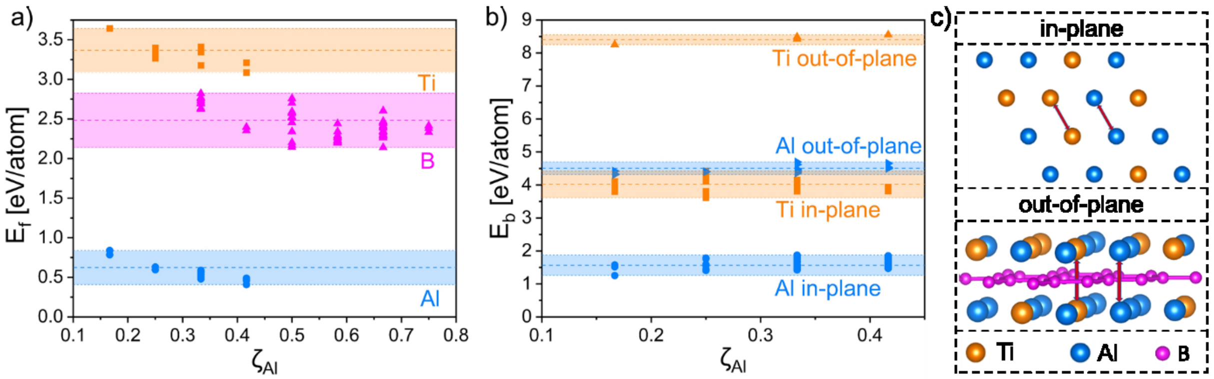

Figure 2. Formation energy of vacancies for Ti, B and Al in Ti$_{0.12}$Al$_{0.21}$B$_{0.67}$ (a) as well as activation energy of migration of Al and Ti atoms (b) in dependence of the Al-fraction of the local chemical environment ζ_{Al}. For the activation energy, in-plane (within the metal lattice) and out-of-plane movement (through the B lattice) has to be differentiated (c).

TEM images of the cross-sectional morphology and corresponding EDX maps of the as deposited as well as the oxidized $Ti_{0.12}Al_{0.21}B_{0.67}$ coatings are shown in Figure 3. For the as deposited coating, in agreement with Navidi et al. [12], a well-defined columnar morphology with a column width ranging from 10 to 65 nm is observed in Figure 3 (a). EDX and SAED (supplementary materials Figure S 1) are consistent with the formation of a homogeneous solid solution between $Ti_{0.33}B_{0.67}$ and $Al_{0.33}B_{0.67}$. Additionally, a native oxide scale with a thickness of around 4 nm, containing mainly Al and O, is identified by STEM and EDX. Furthermore, it can be seen, that the column boundaries are enriched in Al and O, see Figure 3 (a). Hereby, an O gradient from the coating surface to the substrate interface can be observed, which appears to be caused by a change in grain boundary morphology: At the coating surface the column boundaries are less dense than in the vicinity of the interface to the substrate. The cross sections of coatings annealed at 700 °C for 1, 4 and 8 h are shown in Figure 3 (b) to (d), respectively. Comparison between Figure 3 (b) and Figure 3 (a) shows that, after oxidation for 1 h at 700 °C, the column asperity geometry changes from spherical-like towards facetted. HRSTEM analysis, shown in Figure S 2, reveals the formation of $(1\bar{1}01)$ facets. While this topographic change appears to remain unaltered for longer holding times, see Figure 3 (c) and (d), the oxide scale thickness increases after oxidation for 1 and 4 h from the native oxide scale with a thickness of ~ 4 nm to 30 ± 8 nm and 41 ± 9 nm, respectively. After oxidation for 8 h at 700°C, no significant changes in oxide scale thickness (42 ± 12 nm) or morphology could be observed.

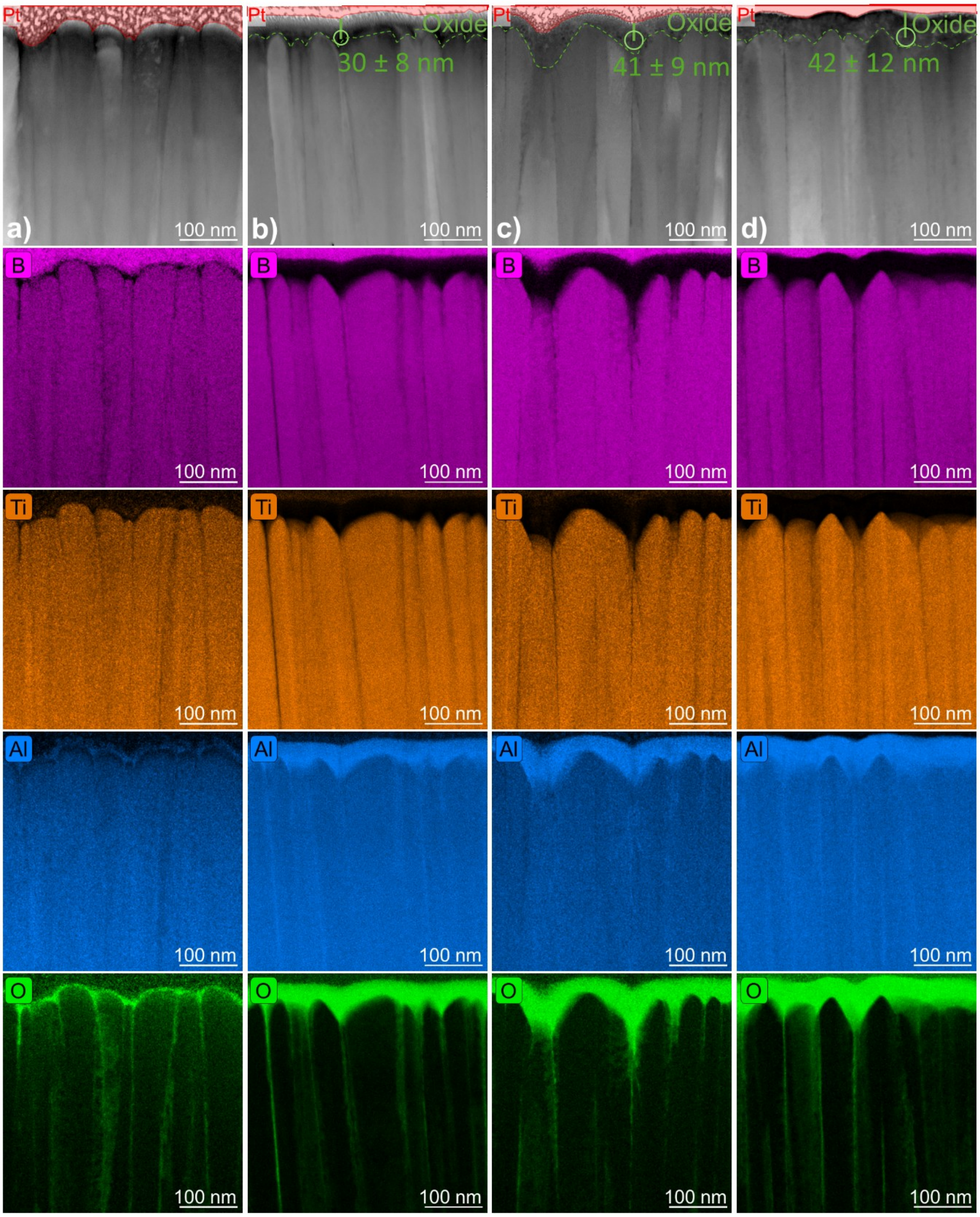

Figure 3. HAADF images and EDX maps in at.% of a) as-deposited sample and oxidized samples at 700 °C for b) 1 h c) 4 h and d) 8 h. The protective Pt layer is colored in red.

STEM and EDX data shown in Figure 4 (a), indicate that the oxide layer formed after oxidation at 700 °C for 8 h consists primarily of Al and O (40 ± 2 at.% Al and 54 ± 2 at.% O) with a B content of 6 ± 2 at.%. The measured concentration of Ti is with ~ 0.3 at.% within the detection limit and hence a significant presence of Ti in the scale cannot be inferred. Raising the oxidation temperature to 800 and 900 °C, the oxide layer thickness measured after 8 h increases to 86 ± 12 nm and 333 ± 11 nm, respectively. As can be seen in Figure 4 (b), the scale is primarily composed of Al and O (34 ± 4 at.% Al and 61 ± 4 at.% O) containing 5 ± 2 at.% B, and is hence similar to the composition measured after oxidation at 700 °C. The formation of the Al-rich oxide layer is consistent with DFT data, see Figure 2, as Al diffusion is predicted to be enabled at lower temperatures than Ti-diffusion. This prediction is based on envelope calculations taking the energy required to form vacancies on the metal sublattice as well as the associated migration barriers into account. While the morphology of the oxide scale surface after oxidation at 700 °C is smooth without apparent roughness, see Figure 4 (c), after oxidation at 900 °C, see Figure 4 (d), the oxide scale shows evidence for pronounced faceting, see also Figure 5 (a).

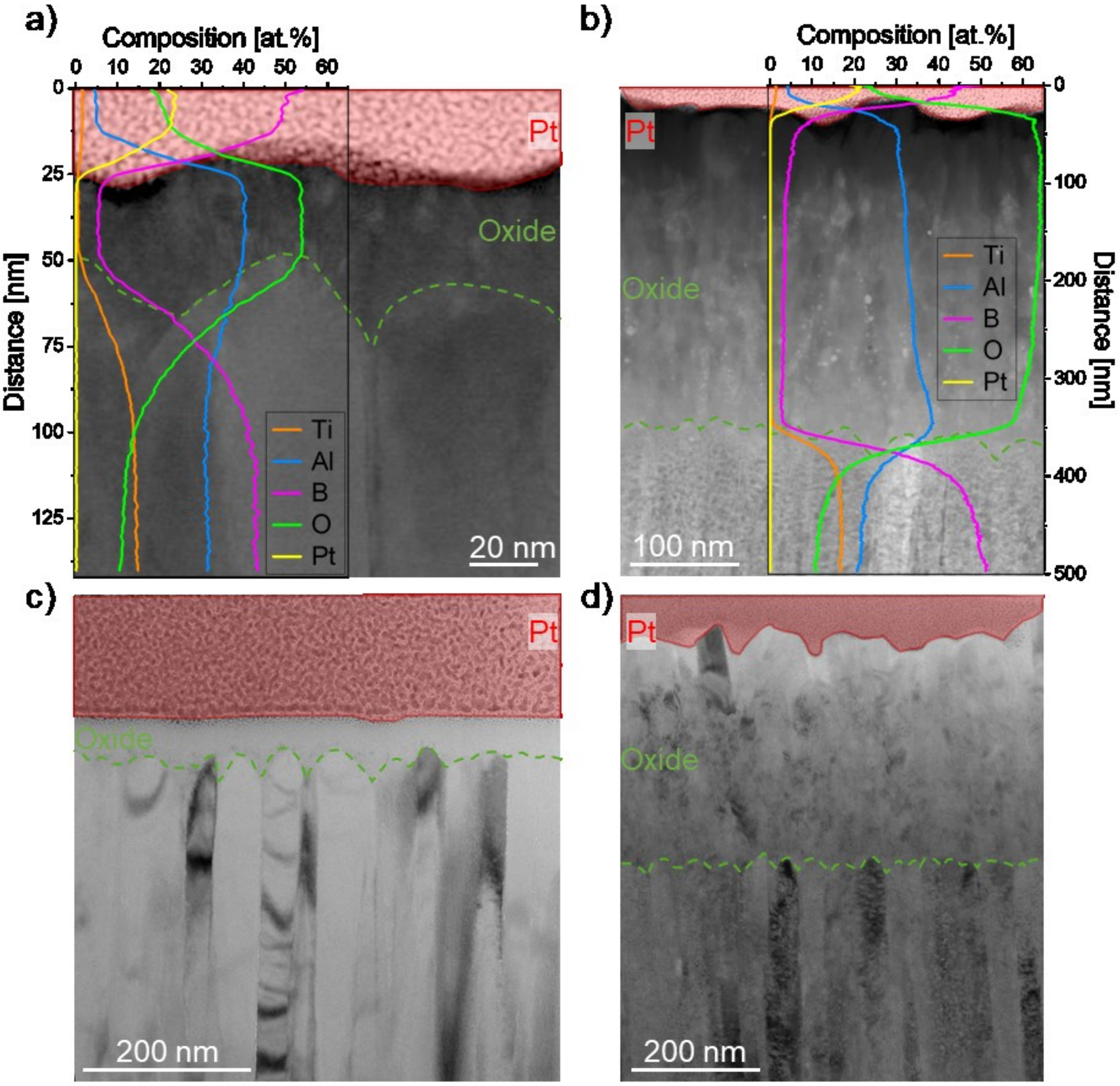

Figure 4. a) EDX line scan of oxidized sample (700 °C, 8 h): Oxide layer consists primarily of Al and O. b) Composition of the oxide layer after oxidation at 900 °C for 8 h. c) and d) TEM images of the oxide layer morphology: after annealing at 700 °C for 8 h, the oxide layer is smooth (c), while after oxidation at 900 °C for 8 h, faceting is observed (d).

To probe the structure evolution along the oxide layer thickness after oxidation at 900 °C for 8 h, SAED data was obtained from regions depicted in Figure 5 (a) ranging from the interface of the oxide scale with the coating (Figure 5 (b)) to the oxide scale surface (Figure 5 (f)).

In the vicinity of the interface, the formation of a continuous (nano-)crystalline layer is witnessed by the fully developed diffraction rings shown in Figure 5 (c). Additionally, the presence of amorphous regions is indicated by broad and diffuse diffraction rings, see Figure 5 (c). Grain size and crystallinity within the scale increase with increasing distance to the coating/scale interface, see Figure 5 (c) to (f), where the formation of crystallites with grain sizes < 70 nm is evident from Figure 5 (a). With increasing distance from the coating/oxide interface, the intensity of reflexes corresponding to the diborides decreases, while the intensity corresponding to the oxide scale increases [99-101].

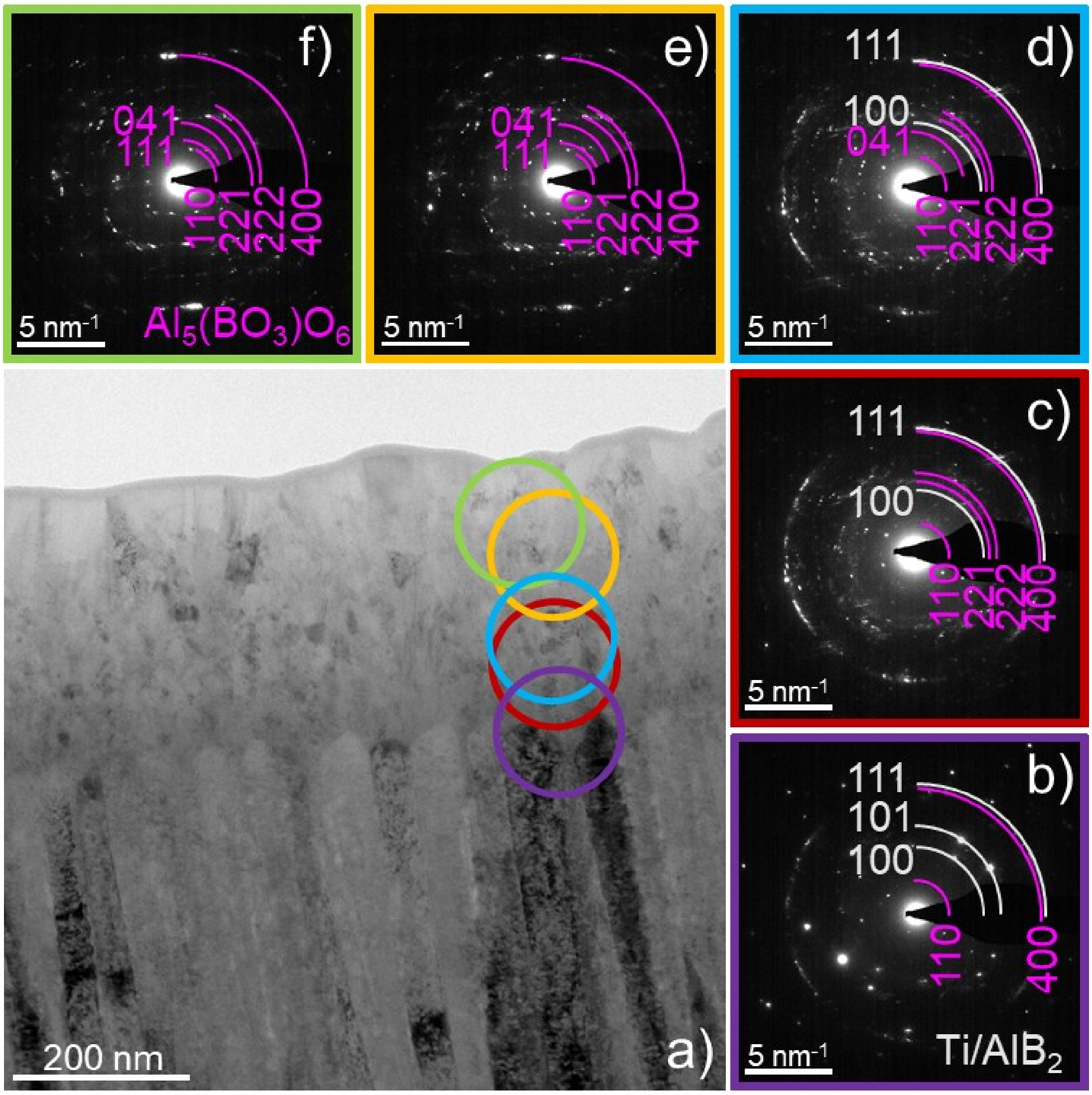

Figure 5. TEM BF-image (a) and SAED patterns from different regions through the oxide layer (b-f) including the interface between scale and remaining film of a coating oxidized at 900 °C for 8 h. At the interface between coating and scale (b-c), the formation of amorphous regions as well as a continuous (nano-)crystalline layer is observed, while the grain size increases significantly towards the surface (d-f).

Phase analysis, based on the SAED data presented in Table 1**,** reveals the formation of $Al_5(BO_3)O_6$ crystallites [100], while the presence of initially expected alumina polymorphs appears to be unlikely. All major diffraction signals can be exclusively explained by the presence of $Al_5(BO_3)O_6$ in the oxide scale, whereby the (110) and (041) peaks are unique to orthorhombic $Al_5(BO_3)O_6$ and cannot be explained by the presence of alumina polymorphs. Additionally, the measured interplanar spacings are in very good agreement with the ICSD (PDF 01-072-1931) [100] data with a deviation of 0.5 ± 0.5 %, compare Table 1 and Figure S 3. In contrast, the best fit for alumina, especially for lower atomic distances, is for θ- and κ-alumina, see Figure S 3, whereby the deviation to the ICSD (PDF 01-079-1559 and 01-088-0107) [102, 103] data of 2.5 ± 1.3 % for θ-alumina and 1.6 ± 1 % for κ-alumina are significantly larger than for $Al_5(BO_3)O_6$. Thereby, taking the unique peaks as well as the deviations to the ICSD data into account, the presence of $Al_5(BO_3)O_6$ is clearly established. However, the here obtained diffraction data also shows very good agreement with orthorhombic $Al_{18}B_4O_{33}$ (PDF 00-032-0003). Both, the chemical and structural differences between the two borate phases are minute. While the O concentration in both phases is with 60 at.% constant, the differences in B and Al concentrations are 0.6 at.% and hence not resolvable with the composition probes employed here. The maximum relative deviation of experimentally observed diffraction signals, within the interplanar spacing range of $1.4 \leq d \leq 6.0$ Å between $Al_{18}B_4O_{33}$ (PDF 00-032-0003) and $Al_5(BO_3)O_6$ (PDF 01-072-1931), is 0.1 %. Hence, the two aluminoborates, $Al_{18}B_4O_{33}$ and $Al_5(BO_3)O_6$, cannot be differentiated with the acquired data, as the composition and structural deviations cannot be resolved.

Table 1. Phase analysis of SAED pattern shown in Figure 5 (f). The measured atomic distances in Å are identified to correlate with the formation of $Al_5(BO_3)O_6$ [100] in comparison to θ- [102] and κ- [103] alumina. The accuracy between the literature and measured value is given by a color scheme (green < 1 %, yellow < 2 %, orange ≥ 2 %, red = no fit).

	$Al_5(BO_3)O_6$			**θ-Al_2O_3**			**κ-Al_2O_3**		
d_m [Å]	**(hkl)**	**d** [100]	**Δd/d [%]**	**(hkl)**	**d** [102]	**Δd/d [%]**	**(hkl)**	**d** [103]	**Δd/d [%]**
5.35	(021)	5.37	0.4	(001)	5.46	2.0			🟥
5.3	(110)	5.3	0.0			🟥			🟥
4.36	(111)	4.37	0.2	(20-1)	4.54	4.0	(002)	4.48	2.7
3.7	(130)	3.75	1.3	(201)	3.56	3.9	(111)	3.79	2.4
3.37	(041)	3.37	0.0			🟥			🟥
2.82	(200)	2.83	0.4	(400) (40-1)	2.88 2.84	2.1 0.7	(013)	2.81	0.4
2.66	(042) (220)	2.69 2.65	1.1 0.4	(002)	2.73	2.6	(031)	2.65	0.4
2.5	(221)	2.51	0.4	(111)	2.45	2.0	(122)	2.58	3.1
2.23	(240)	2.26	1.3	(401)	2.33	4.3	(211)	2.25	0.9
2.18	(222)	2.18	0.0	(31-1)	2.25	3.1	(123)	2.17	0.5
1.41	(400)	1.42	0.7	(20-4)	1.41	0.0	(205) (135)	1.44 1.44	2.1 2.1

To critically appraise the preferential Al diffusion notion, predicted by DFT envelope calculations, the spatially and temporally resolved chemical composition in regions adjacent to the coating/scale interface was measured via EDX line scans after oxidation for 1, 4 and 8 h at 700 °C and compared to the as deposited state, see Figure 6 (a) to (d) and Figure S 4.

For all investigated coatings, the O concentration is significantly higher compared to the data measured by ERDA [12]. This is likely due to oxidation of the lamellae sides as a consequence of atmosphere exposure during transfer after lift-out prior to TEM imaging. Therefore, only O concentration variations within one sample are discussed further, while the Al/metal ratio is compared between the coatings.

The O content of the as deposited coating depicted in Figure 6 (a) is steadily increasing over the 100 nm thick region adjacent to the surface, where the interfacial region between the 4 nm thick native oxide scale (not distinguishable) and the coating is marked in red, see Figure 3 (a) and Figure S 4 (a). The increase of oxygen concentration in the region below the 4 nm thick native oxide and the coating/scale interface, marked in red, can be attributed to preferential O incorporation at grain boundaries and triple junctions due to atmosphere exposure. In contrast to the O content, a decrease in the Al/metal ratio in a region of 20 nm below the native oxide, can be observed. It is evident that Al forming the native oxide scale has diffused out of this region.

Upon oxidation at 700 and 800 °C, see Figure 6 (b) to (e), the formation of the oxide scale, marked in green, is evident while the Al/metal ratio within the coating in the region adjacent to the interfacial region, marked in red, is within the range of 0.65 ± 0.05. Furthermore, a drastic increase in the Al/metal ratio can be seen in the interfacial region, marked in red, for all at 700 and 800 °C oxidized samples. This is in stark contrast to the chemical composition measured in the interfacial region of the as deposited sample, shown in Figure 6 (a), where Al depletion by the native oxide scale formation causes a decrease in the Al/metal ratio from 0.65 to 0.48 in the region marked in red. Hence, it is evident that the Al depleted region, only identified for the as deposited coating, could not be replenished by Al diffusion from the reservoir in the as deposited coating. Contrarily at ≥ 700°C, this kinetic limitation is overcome as witnessed by the disappearance of the Al depleted region beneath the interfacial region, marked in red in Figure 6 (b) to (e) as a consequence of the Al redistribution from the Al reservoir of the coating resulting in a homogeneous distribution of Al over the coating thickness.

Further evidence for thermally activated Al diffusion, enabling the formation of the oxide scale, is shown by HR-EDX in Figure S 5 in the form of an Al pile up at the coating/scale interface after oxidation at 700 °C for 8 h. Figure 6 (f) depicts the EDX linescans after oxidation at 900 °C for 8 h. While the composition variations measured in the interfacial region, marked in red, correspond to observations made at lower oxidation temperatures, the oxide scale thickness increased to 333 ± 11 nm and the Al/metal ratio within the coating ranges from 0.49 to 0.58.

Assuming that the oxide layer consists exclusively of $Al_5(BO_3)O_6$ with a density of 2.94 g cm^{-3} [100] and that all Al atoms forming the scale are supplied from the reservoir of the unoxidized coating, the corresponding Al concentration decrease can be calculated: After oxidation for 8 h at 800 and 900 °C, the oxide scale thicknesses of 86 ± 12 nm and 333 ± 11 result in a decrease of the corresponding Al concentrations by 1.7 ± 0.2 at.% and 6.7 ± 0.2 at.% respectively. Therefore, a significant decrease in the Al content over the whole unoxidized coating thickness, indicative of the diffusion mediated redistribution of Al from the unoxidized coating to the oxide scale, can be observed after oxidation at 900 °C. However, after oxidation at 800 °C, the measured Al concentration variation is within the EDX detection limit, consequently the comparatively low Al requirement for oxide scales at temperatures < 900 °C could not be resolved.

Hence, it is evident that scale growth is mediated by Al diffusion from the unoxidized coating to the oxide scale, while no evidence for diffusion of Ti could be obtained at oxidation temperatures < 900°C, see Figure 6 (b) to (e). The fact that Al diffusion enables scale formation, while Ti diffusion is inactive, see Figure 6 (b) to (e), is consistent with the lower energies necessary for Al mass transport compared to Ti as calculated by DFT (Figure 2). Furthermore, as the oxidation temperature is increased to 900 °C, diffusion of both Al and Ti is enabled, leading to the formation of Al- and Ti-rich regions, represented by modulations in the line scan shown in Figure 6 (f) as well as by the differently colored regions in Figure 6 (g). Again, these composition variations, caused by diffusion as discussed above, are in very good agreement with the DFT calculations presented in Figure 2.

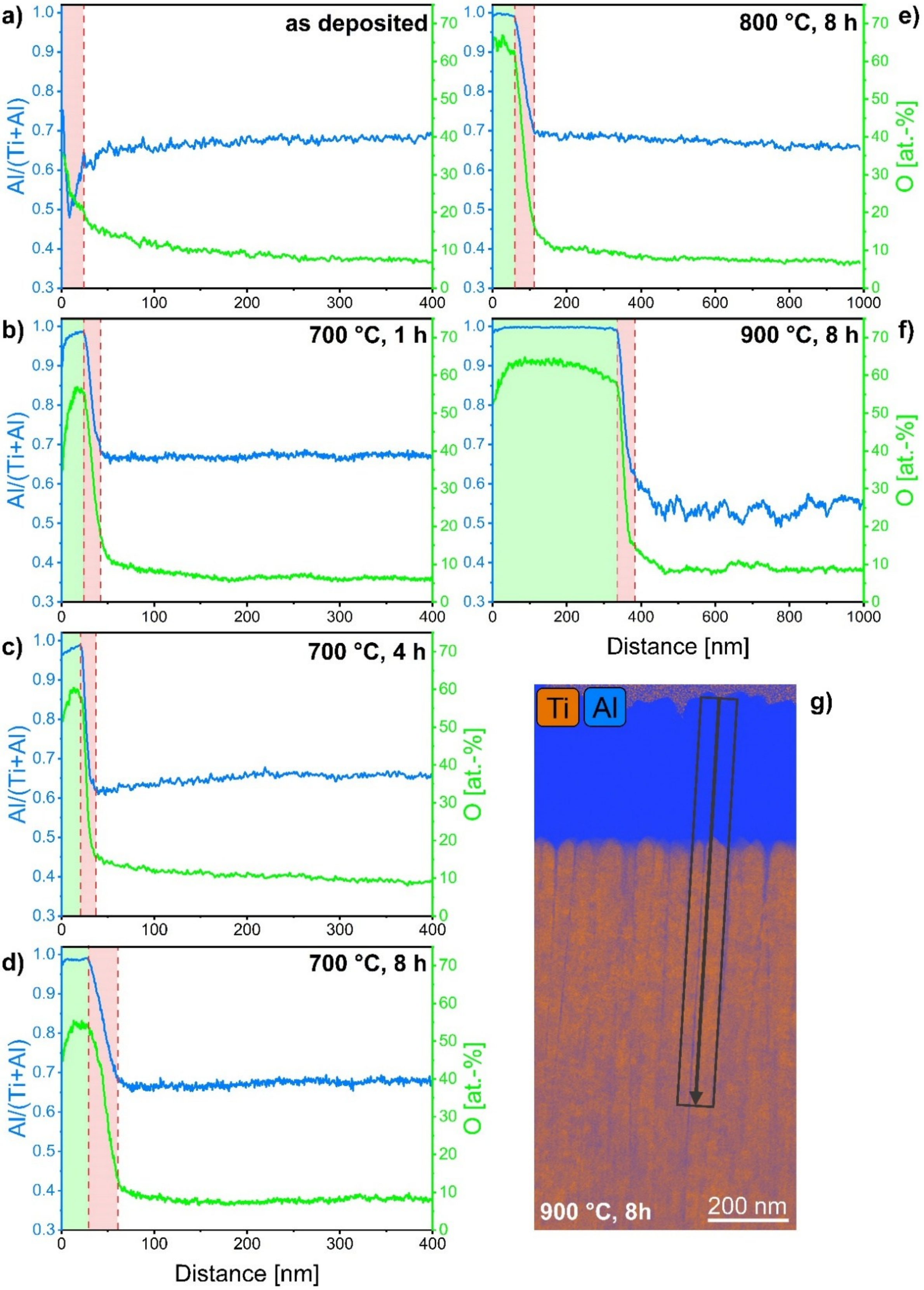

Figure 6. Linescans of as deposited (a) and oxidized $Ti_{0.12}Al_{0.21}B_{0.67}$ coatings at 700 °C for 1 h (b), 4 h (c) and 8 h (d). Diffusion of Al over the length of the coating can be seen. When increasing the oxidation temperature to 800 °C (e) and 900 °C (f), a decrease in the Al/metal ratio is shown with segregation of TiB_2 and AlB_2 visible in (g). The regions marked in green and red in images (a) to (f) correspond to the oxide scale and the interfacial regions between the scale and the unoxidized coating.

Completing the chemical information given above, the *Z* contrast in the STEM images in Figure 7 shows that the formation of Al- and Ti-rich regions within the columns is mediated by diffusion of Al as well as Ti. This observation is consistent with thermal stability investigations, where the formation of Al- and Ti-rich regions was shown to be caused by decomposition of the metastable solid solution of TiB_2 and AlB_2 [104] via spinodal decomposition. In contrast to the as deposited coating, shown in Figure 7 (a), the decomposition of the $(Ti,Al)B_2$ solid solution after oxidation is characterized by the brighter (Ti-rich) and darker (Al-rich) regions, see Figure 7(b). As a consequence of Al diffusion and Al incorporation in the oxide scale, the formation of elongated porous regions (marked in red) with sizes > 100 nm in length and a few nm in width is observed.

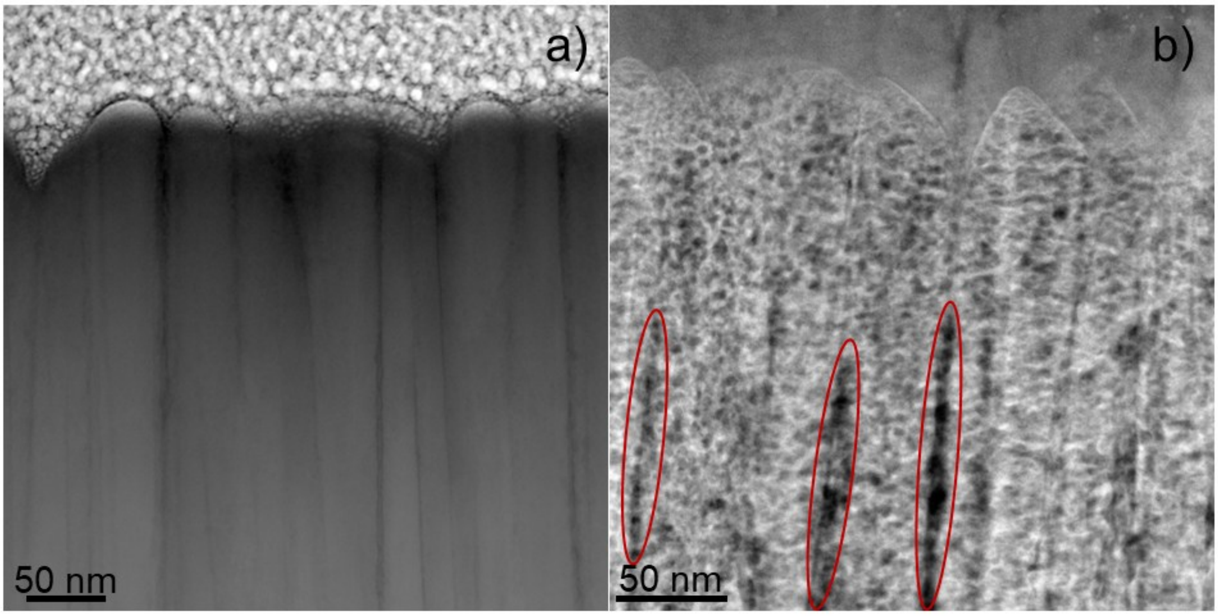

Figure 7. STEM HAADF images of an as deposited coating (a) and oxidized at 900 °C for 8 h (b).

Atom probe tomography was performed after oxidation for 8 h at 700 °C and at 900 °C and the specimens were extracted from in-plane direction at a depth of ~300 nm below the oxide/coating interface. Consistent with the EDX maps shown in Figure 3 and the associated discussion, it is evident from the spatially resolved analysis of the O content depicted in Figure 8 (a) and (b) that multiple column boundaries were probed in the sample oxidized at 700 °C. Locally, the Al and O content at the column boundaries increase from 26 ± 2 to 39 ± 2 at.% and from 2 ± 1 to 9 ± 1 at.% (distance of ~60 nm). After oxidation at 900 °C, the APT data show elemental distributions in Figure 8 (c) and (d), consistent with the above presented Al redistribution notion. In contrast to the coating oxidized at 700 °C (see Figure 8 (a) and (b)) as well as the as-deposited sample (see supplementary Figure S 6), the formation of Al- and Ti-rich regions, is witnessed by the variation of the Al/(Ti+Al) ratio between 0.31 ± 0.05 and 0.59 ± 0.10 (distance of 16 to 18 nm, Figure 8 (e)), indicating spinodal decomposition. From the same data set, the grain boundary composition ranges can be extracted. The grain boundaries contain up to 51 ± 2 at.% Al and 36 ± 2 at.% O, while the Ti and B content are reduced to 7 ± 1 at.% and 6 ± 1 at.%, respectively (distance of 27 to 28 nm).

The results observed here show both, similarities and differences to recently published thermal stability data for $Ti_{0.12}Al_{0.21}B_{0.67}$ coatings where after 1 h at 1000 °C spinodal decomposition was witnessed based on EDX and APT data [104]. Spinodal decomposition within the grains occurs upon annealing [104] as well as upon oxidation. In contrast to the coatings annealed at 1000 °C for 1 hour [104], no indication of AlB_{12} formation could be obtained after oxidation at 900 °C for 8 h, indicating that the oxidation behavior at these conditions is not limited by thermal decomposition.

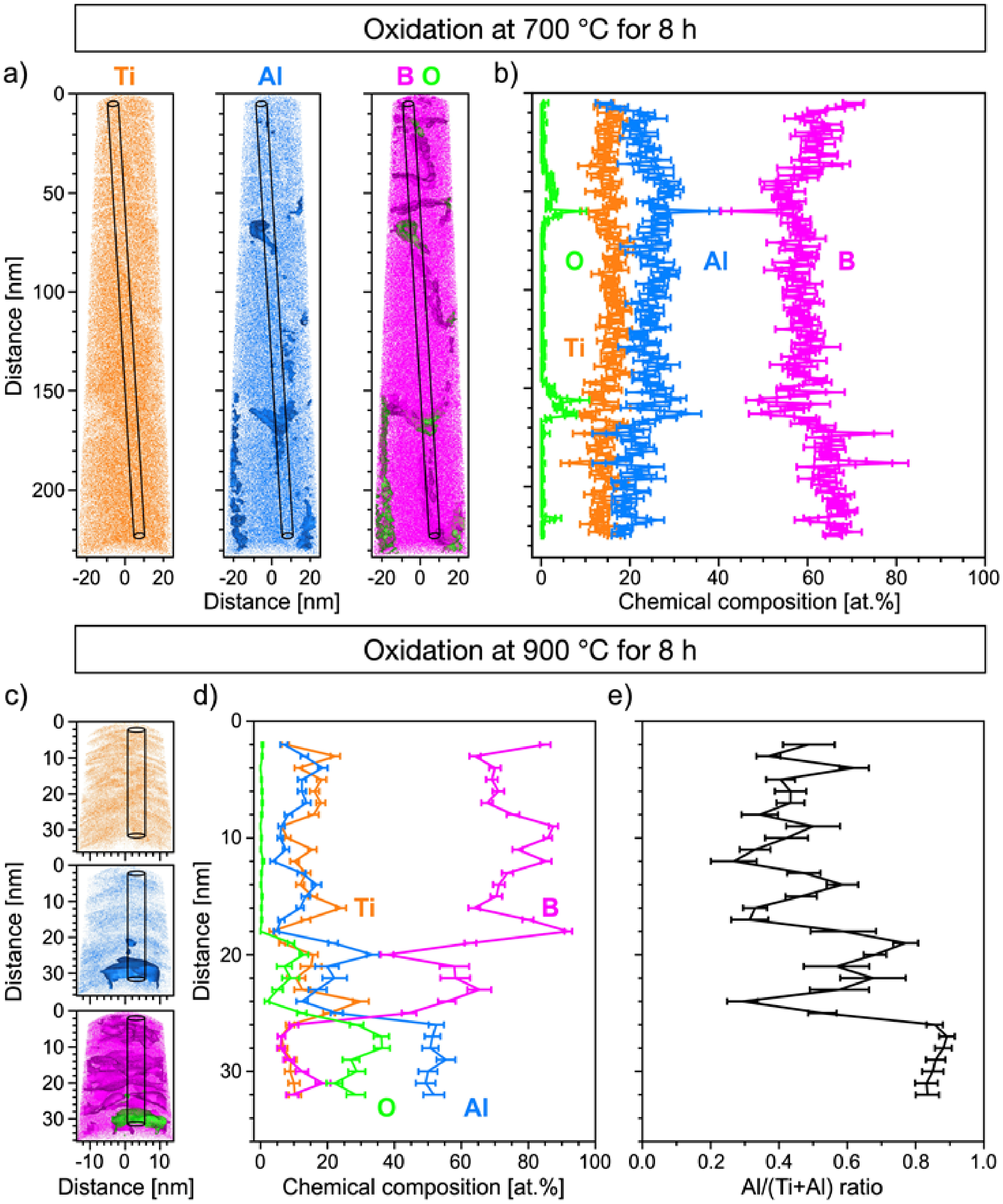

Figure 8. Atomic positions, isoconcentration surfaces (Al ≥ 30 at.%, B ≥ 70 at.%, O ≥ 4 at.%) and composition profile obtained by atom-probe tomography of an in-plane specimen taken from a depth of ~300 nm below the surface for the sample oxidized at 700 °C for 8 h (a) and (b) and 900 °C for 8 h (c) and (d) as well as the Al/(Ti+Al) ratio for the 900 °C sample (e). The cylinders exhibit a diameter of 5 nm.

Proposed oxidation mechanism

The here unraveled oxidation mechanism for passivating [12], stoichiometric $Ti_{0.12}Al_{0.21}B_{.0.67}$ is summarized in Figure 9. A columnar structure is observed in the as deposited state, exhibiting grain boundaries that are enriched in Al and O compared to the grains. Atmosphere exposure of the as deposited coating results in the formation of a 4 nm thick native oxide layer, formed by Al diffusion from a 20 nm thick region adjacent to the scale coating interface as witnessed by EDX. Upon oxidation, the topography changes from spherically terminated columns to more faceted terminated columns.

Upon oxidation, a scale layer forms, which is amorphous at 700 °C and transforms to (nano-)crystalline at 900 °C, consisting of 34 ± 4 at.% of Al, 61 ± 4 at.% of O and 5 ± 2 at.% of B at 900 °C. The scale layer is formed by Al diffusion from the unoxidized coating to the oxide scale, which requires, according to DFT predictions compiled in Figure 2, a significantly lower energy for mass transport on the metal sublattice than Ti. Hence, based on these DFT predictions, the previously unexplained superior oxidation behavior compared to $Ti_{0.27}Al_{0.21}N_{0.52}$ coatings can be understood via the here reported formation of a passivating boron containing oxide scale, while for $Ti_{0.27}Al_{0.21}N_{0.52}$ coatings, the formation of a Ti and Al containing oxide scale is observed [15].

Diffusion through the passivating oxide scale is limiting the oxidation kinetics. The homogeneous Al profile throughout the unoxidized coatings, see Figure 6, is enabled by Al diffusion, within the grains as well as along grain boundaries, in the unoxidized coating as Al required for scale formation is upon oxidation replenished for all oxidation conditions studied here, except for 900 °C and 8 hours. At this condition, the amount of Al required to form the scale can no longer be replenished by Al redistribution from the unoxidized coating as witnessed by an overall decrease of the inhomogeneous Al distribution measured by EDX, see Figure 6 (f). Simultaneously, spinodal decomposition of the $(Ti,Al)B_2$ solid solution into Al-rich and Ti-rich regions within the grains can be observed with EDX, see Figure 6 (f) and (g), HRSTEM, see Figure 7 and

APT, see Figure 8 (c) to (e), which is enabled by the onset of Ti diffusion predicted to occur at higher temperatures compared to Al, see Figure 2. Hence, at 900 °C simultaneous diffusion of Al and Ti enables spinodal decomposition. The fact that this observation is in contrast to the formation of Ti-rich crystallites by nucleation and growth as reported by Mockuté et al. [87] for B-rich tissue phase containing $Ti_{0.17}Al_{0.07}B_{0.76}$ [$(Ti_{0.71}Al_{0.29})B_{3.08}$] annealed at 1000 °C for 1 h, underlines the significance of the chemical composition, specifically deviations from stoichiometry, for the oxidation behavior of $(Ti,Al)B_2$ based coatings.

The exceptional oxidation behavior of $Ti_{0.12}Al_{0.21}B_{0.67}$ can be explained by the formation of the B containing, amorphous and (nano-)crystalline aluminoborate layer, caused by the diffusion of Al from the unoxidized coating to the scale.

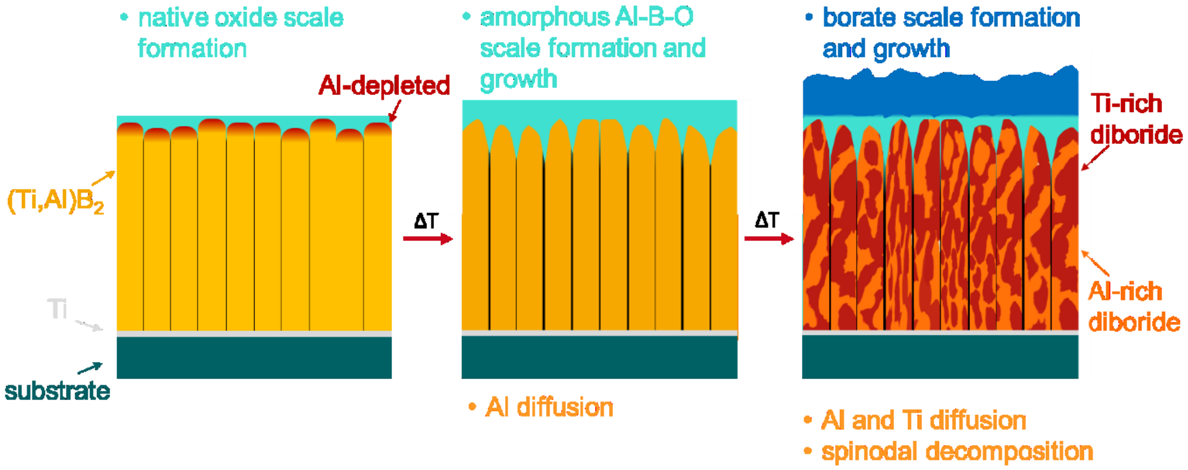

Figure 9. Schematic representation of the here identified oxidation mechanism for $Ti_{0.12}Al_{0.21}B_{.0.67}$.

Comparing the oxidation behavior at 900 °C after 2 h of a 1.3 µm thick $Ti_{0.27}Al_{0.21}N_{0.52}$ coating with the here considered $Ti_{0.12}Al_{0.21}B_{0.67}$ coating, where both coatings exhibit, within the measurement error an identical Al concentration, it is evident that the nitride coating is fully oxidized [15], while the scale thickness measured on $Ti_{0.21}Al_{0.21}B_{0.67}$ is 333 ± 11 nm at the same temperature but at a 4 times longer oxidation time. At these conditions, the superior oxidation behavior of the diboride compared to the nitride coating, both with an Al concentration of 21 at.%, is hence due to the passivating capacity of the borate scale formed on the boride as compared to the mixed, Ti and Al containing oxide scale forming on the nitride [15].

3.5 Conclusion

The high temperature oxidation behavior of $Ti_{0.12}Al_{0.21}B_{0.67}$ coatings was investigated in an electron microscopy study, supported by ab initio calculations. STEM imaging revealed the formation of a native 4 nm thick Al-rich oxide scale as well as the incorporation of O at the grain boundaries in the as deposited state. Upon oxidation, thicker scales consisting primarily of Al and O with a small B content were formed, which appear to be amorphous at 700 °C and (nano-)crystalline at 900 °C. The average activation energies of migration and the formation energy of vacancies, which were obtained by DFT calculations, proved to be lower for Al than for Ti, suggesting that Al diffusion is initiated at lower temperatures than Ti diffusion. These predictions are consistent with TEM, EDX and APT data.

Upon oxidation at 700 and 800 °C, the formation and growth of an oxide scale composed of Al and O as well as ~5 at.% B is mediated by Al diffusion within the unoxidized $Ti_{0.12}Al_{0.21}B_{0.67}$ phase, replenishing the Al required for scale formation.

After oxidation at 900 °C for 8 h, a crystalline aluminoborate layer was identified by EDX and SAED analysis. Additionally, spinodal decomposition of the $Ti_{0.12}Al_{0.21}B_{0.67}$ phase into Al- and Ti-rich boride regions is witnessed. The spinodal decomposition is enabled by concurrent diffusion of Al and Ti, setting in only at higher temperatures and longer holding times due to the higher averaged energies required for Ti migration as compared to Al, consistent with DFT predictions. Overall, the extraordinary oxidation resistance of $Ti_{0.12}Al_{0.21}B_{0.67}$ is enabled by energetically preferred Al diffusion leading to the formation of a passivating, amorphous oxide scale, predominantly comprised of Al, O and B. At higher temperatures, the transformation of the amorphous oxide scale to (nano-)crystalline $Al_5(BO_3)O_6$ occurs, while simultaneously, the onset of Ti diffusion in combination with the Al diffusion enables spinodal decomposition of the $Ti_{0.12}Al_{0.21}B_{0.67}$ phase into Ti- and Al-rich regions. In comparison to $Ti_{0.27}Al_{0.21}N_{0.52}$ coatings, with an identical Al concentration, the superior oxidation resistance of stoichiometric $Ti_{0.12}Al_{0.21}B_{0.67}$ coatings at 900 °C can be rationalized based on the formation of a passivating (nano-)crystalline aluminoborate scale layer, rendering the here investigated boride with a 333 ± 11 nm thick scale layer after oxidation for 8 h, while the $Ti_{0.27}Al_{0.21}N_{0.52}$ coating is oxidized completely after 2 h [15].

4 Temporally-resolved Decomposition of $Ti_{0.12}Al_{0.21}B_{0.67}$ Thin Films at 1000 °C

4.1 Introduction

Transition metal diborides are currently considered as coating materials for applications that require remarkable durability in challenging environments and under extreme conditions, while retaining phase stability. Particularly, TiB_2 has garnered significant attention due to its high melting point, exceeding 3225 ± 20 °C [73], low density of 4.1 to 4.5 g/cm^3 [67, 105, 106], superior hardness of 45 up to 60 GPa [2, 68, 75, 107] and an elastic modulus (Young's modulus) range of 520 to 605 GPa [2, 68, 75, 107]. Interestingly, quantum mechanical calculations predict elastic modulus values ranging from 582 [108] to 679 GPa [109]. TiB_2 crystallizes in the AlB_2 structure, a layered arrangement of covalent, ionic bonds between Ti and B atoms resulting in the notable thermal and mechanical stability of TiB_2 [110]. Given its unique combination of properties, TiB_2 bulk materials as well as thin films are commonly utilized for wear and corrosion protection [69, 107, 111, 112]. TiB_2 thin films serve as diffusion barriers in the field of microelectronics [113-116]. Bulk TiB_2 cathodes are investigated as a replacement for graphite cathodes in an effort to reduce CO_2 emissions during electrolytic Al extraction [76, 77].

In a theoretical study, Alling et al. [117] investigated several AlB_2 type ternary diborides regarding mixing energetics and age hardening potential. For $(Ti_{1-x}Al_x)B_2$, a strong driving force for isostructural clustering and hence the formation of Al- and Ti-rich $TiAlB_2$ regions has been predicted at 1000 °C. The authors suggested that this material system may be suitable for hard coating applications, since its potential for age hardening appears to be high [117].

From an equilibrium thermodynamics point of view, AlB_2 has been reported to decompose into Al and AlB_{12} at temperatures larger than 980 °C [118] and the equilibrium phase diagram of Ti-Al-B predicts the formation of a stable mixture of liquid Al, TiB_2, and AlB_{12} at temperatures ≥ 1000 °C [119].

Throughout this paper, we report the chemical composition measured in at.%. When citing chemical compositions, utilizing stoichiometric factors from literature, we add the at.% notation in brackets for the convenience of the reader. While the thermal stability of stoichiometric $(Ti,Al)B_2$ has not been studied systematically so far, Mockute et al. [120] investigated the structural and mechanical properties of $Ti_{1-x}Al_xB_{2+y}$ deposited by magnetron sputtering from AlB_2 and TiB_2 targets with $0.30 \leq x \leq 0.66$ and $0.07 \leq y \leq 1.22$. The indentation modulus (reduced elastic modulus) was reported from 278 GPa for Ti-rich to 106 GPa for the Al-rich thin films. Based on scanning transmission electron microscopy (STEM) and energy dispersive X-ray spectroscopy (STEM-EDX) data, the observed phase separation of $(Ti_{0.34}Al_{0.66})B_{2.07}$ $(Ti_{0.11}Al_{0.22}B_{0.67})$ into Ti and Al-rich nanometer-size domains in the as-deposited state was proposed to be due to surface-initiated spinodal decomposition during deposition. The as-deposited $(Ti_{0.70}Al_{0.30})B_{3.22}$ $(Ti_{0.17}Al_{0.07}B_{0.76})$ thin film, contrary to $(Ti_{0.34}Al_{0.66})B_{2.07}$ $(Ti_{0.11}Al_{0.22}B_{0.67})$, was reported to form a homogeneous solid solution with no indication for decomposition in the presence of a B-rich tissue phase at the grain boundaries.

In another study, Mockute et al. [87] investigated the structural and mechanical properties of as-deposited and annealed thin films and reported age-hardening of DCMS deposited $(Ti_{0.71}Al_{0.29})B_{3.08}$ $(Ti_{0.17}Al_{0.07}B_{0.75})$ from AlB_2 and TiB_2 targets at 1000 °C for 1 h. The hardness and elastic modulus increased after annealing from 32 ± 0.4 to 37 ± 0.8 GPa and from 436 ± 3 to 461 ± 3 GPa, respectively. The as-deposited high hardness was attributed to a columnar microstructure, in which sub-columns of $(Ti_{0.71}Al_{0.29})B_{3.08}$ $(Ti_{0.17}Al_{0.07}B_{0.75})$ are separated by a B-tissue phase. The observed age-hardening was ascribed to the microstructural transformation within the $(Ti_{0.71}Al_{0.29})B_{3.08}$ $(Ti_{0.17}Al_{0.07}B_{0.75})$ columns and the formation of Ti-deficient $(Ti,Al)B_2$ precipitates within the grain interior. This phase separation was not attributed to spinodal decomposition, but rather to nucleation and growth [87].

From the above discussion, it is evident that thermal stability data of Ti-Al-B thin films is scarce and that the thermal stability of stoichiometric $(Ti,Al)B_2$ thin films has not been investigated systematically yet.

Here, we explore the thermal stability of stoichiometric $Ti_{0.12}Al_{0.21}B_{0.67}$ during isothermal vacuum annealing at 1000 °C for 1 and 3 h and identify the active decomposition mechanisms based on temporally and spatially resolved composition and structure analysis.

4.2 Experimental Details

$Ti_{0.12}Al_{0.21}B_{0.67}$ thin films were grown by magnetron sputtering in a vacuum combinatorial growth deposition system with a base pressure of less than 1×10^{-4} Pa at a substrate temperature of 400 °C. Two B targets with a diameter of 50.8 mm and purity of 99.9% (MaTecK, Germany) were sputtered using radio frequency (RF) power supplies (13.56 MHz) at power densities of 8.5 W/cm^2 and one $Ti_{0.4}Al_{0.6}$ powder-metallurgical target with diameter of 50.8 mm (Plansee Composite Materials, Germany) was sputtered using direct current (DC) power supply at power density of 2 W/cm^2. For the calculation of the power density, the whole surface area of a target (~20.3 cm^2) was considered. α-Al_2O_3 (0001) substrates were placed at 10 cm distance from the targets, rotated with a speed of 15 rpm and kept at floating potential under an Ar atmosphere (99.9999% purity) with a pressure of 0.6 Pa. The deposition time was 180 minutes. The resulting deposition rate was 7.3 nm/min. The venting temperature was < 50 °C. For *in situ* heating tests in the transmission electron microscopy (TEM), a Ti-Al-B thin film with ~ 35 nm thickness was deposited onto a Wildfire nano-chip by DENS Solutions with a Si_3N_4 membrane.

Isothermal annealing of the thin films was performed in a vacuum furnace with a base pressure of 2×10^{-4} Pa. The temperature was set to 1000 °C and the holding time was 1 and 3 h. The heating and cooling rates were set to 10 K/min.

The phase analysis of the as-deposited and annealed thin films was conducted using a Bruker AXS D8 Discover General Area Diffraction Detection System. The Cu X-ray source (λ = 0.154 nm) was operated at voltage and current of 40 kV and 40 mA, respectively, and the incidence angle was fixed at 15° to keep the information depth constant as 2 theta is varied.

The average chemical composition of the films was determined by time-of-flight elastic recoil detection analysis (ERDA) at the Tandem Accelerator Laboratory [121] of Uppsala University. 36 MeV $^{127}I^{8+}$ primary ions were used for the generation of recoils. The incidence and exit angles were 22.5° with respect to the specimen surface, while the angle between the primary ion beam and the detector telescope was 45°. The time-of-flight was measured with thin carbon foils [122] and a segmented gas detector was used [123]. The as-deposited thin film has been characterized in our previous work with a maximum total measurement uncertainty of 5 % of the deduced B concentrations as well as aliquot fractions thereof for the metals (Ti,Al) [12]. To the initial chemical composition of the thin film deposited onto the *in situ* heating chip investigated in TEM, ERDA was performed at the laboratory of Ion Beam Physics of ETH Zürich [124]. Here, $^{127}I^{7+}$ ions were used as the primary projectile with an energy of 13.5 MeV. The incidence as well as the exit angle relative to the sample surface were 18°.

Thin lamellae for TEM investigations were prepared by focused ion beam (FIB) technique using an FEI Helios Nanolab 660 dual-beam microscope with Ga^+ ions at 30 kV. As a protection layer, a 2 µm thick Pt layer was deposited using 80 pA current, followed by trench milling at 2.5 nA. The final lamellae thicknesses were < 100 nm. The lamellae were subsequently analyzed by TEM using a Titan Themis 200 G3 equipped with a SuperX EDX detector (Thermo Fisher Scientific) at an acceleration voltage of 200 kV. *In situ* heating was conducted in the STEM mode and the samples were heated with an average heating rate of 12 K/min to 1100 °C and the holding time was 30 minutes at this temperature. The analysis of diffraction and *in situ* data was conducted with ImageJ, while Velox was used for the imaging and EDX analysis. Single out-of-focus images were removed with ImageJ in the *in situ* video for visualization.

The spatially-resolved composition at the nanometer scale of the as-deposited as well as vacuum-annealed thin films at 1000 °C for 1 and 3 h was determined by atom probe tomography (APT) using a CAMECA local electrode atom probe 4000X HR. Field evaporation was assisted by UV laser pulsing at 50 pJ pulse energy, 125 kHz pulse frequency, 60 K base temperature and the detection rate was set at 0.5 %. 0.8 to 1.4 million ions were acquired and the carried-out reconstructions with AP Suite 6.1 were based on the radii and shank angles of the as-prepared specimens. Specimens were obtained from plan-view lift-outs (see supplementary information of [38]) using FIB technique in the dual-beam microscope mentioned above according to a standard protocol [60]. Low voltage cleaning at 5 kV and 40 pA has been carried out for 10 minutes in order to achieve needle-like specimens with radius and shank angle of < 25 nm and < 10°, respectively.

4.3 Results and Discussion

The chemical composition of the as-deposited and annealed thin films, measured by ERDA, is displayed in Table 2. The as-deposited thin film with 11.4 ± 1.2 at.% of Ti, 20.9 ± 2.1 at.% of Al, and 65.5 ± 3.3 at.% of B is stoichiometric [12] within the measurement uncertainty and for simplicity referred to as $Ti_{0.12}Al_{0.21}B_{0.67}$ in the following discussion. The Al concentration of the as-deposited thin film decreases from 20.9 to 16.8 at.% after annealing for 1 h and to 12.5 at.% after annealing for 3 h. Meanwhile, the O concentration increases from 2.2 at.% for as-deposited thin film to 3.6 and 4.0 at.% after annealing for 1 and 3 h, respectively. The O concentration of the as-deposited thin film is most likely due to the incorporation of residual gas during the growth process [125, 126] and/or due to reactions occurring during exposure to the atmosphere after growth [127]. The oxygen concentration of 4.0 ± 0.3 at.% in the thin film annealed for 3 h can be explained by oxygen uptake during annealing from the residual gas and/or upon exposure to the atmosphere [127]. The thin film deposited on the heating chip contains 11.9 ± 0.9 at.% of Ti, 27.6 ± 2.1 at.% of Al, 59.9 ± 3.0 at.% of B, and 0.6 ± 0.0 at.% of O.

Table 2. Chemical composition of the as-deposited and annealed $Ti_{0.12}Al_{0.21}B_{0.67}$ thin films at 1000 °C up to 3 h obtained by ERDA. While the composition of the as-deposited thin film was reported previously [12], the data is given here again for comparison. Also, the composition of the thin film deposited onto the heating chip is given in the last line.

	Ti [at.%]	Al [at.%]	B [at.%]	O [at.%]
As-deposited **[12]**	11.4 ±	20.9 ±	65.5 ±	2.2 ± 0.1
1 h anneal	11.7 ±	16.8 ±	67.9 ±	3.6 ± 0.2
3 h anneal	12.0 ±	12.5 ±	71.5 ±	4.0 ± 0.2
As-deposited on chip	11.9 ±	27.6 ±	59.9 ±	0.6 ± 0.0

XRD was employed to analyze the phase formation of the thin films grown on sapphire (0001) and the results are presented in Figure 10. The TiB_2 and AlB_2 reference lines, based on [128] and [129], are represented by triangle and square markers, respectively. The formation of a polycrystalline single-phase hexagonal solid solution, henceforth referred to as $(Ti,Al)B_2$, is witnessed by the presence of (100), (110), (111), (200) and (201) peaks in the diffractogram of the as-deposited $Ti_{0.12}Al_{0.21}B_{0.67}$ thin film. With increasing annealing time and decreasing Al concentration, see Table 2, the intensity of the diffraction peaks decreases, see Figure 10, and the full width at half maximum increases concomitantly, see Figure 11. The corresponding lattice parameters of the thin films in this study can be found in the supplementary material. No evidence for the phase formation of AlB_{12}, as predicted in the equilibrium phase diagram [119], was resolvable by XRD.

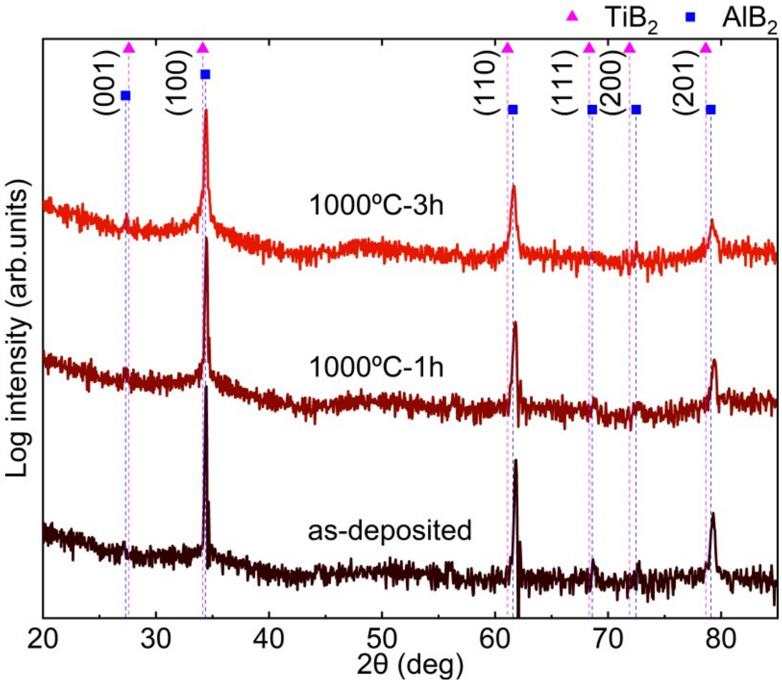

Figure 10. Diffraction patterns of the as-deposited [12] and the annealed $Ti_{0.12}Al_{0.21}B_{0.67}$ thin films at 1000 °C for 1 and 3 h.

Figure 11 depicts the full width at half maximum (FWHM) [130] measured for (001), (100), (110), and (201) diffraction peaks versus annealing time. Increasing FWHM values have been reported to signal the onset of spinodal decomposition for (Ti,Al)N [130, 131]. Hence, it is reasonable to assume that the here observed FWHM increase from 0.07 ° (as-deposited) to 0.15 ° (1 h anneal) and to 0.18° (3 h anneal) indicates the onset of spinodal decomposition in $Ti_{0.12}Al_{0.21}B_{0.67}$ as predicted by Alling *et al.* [117].

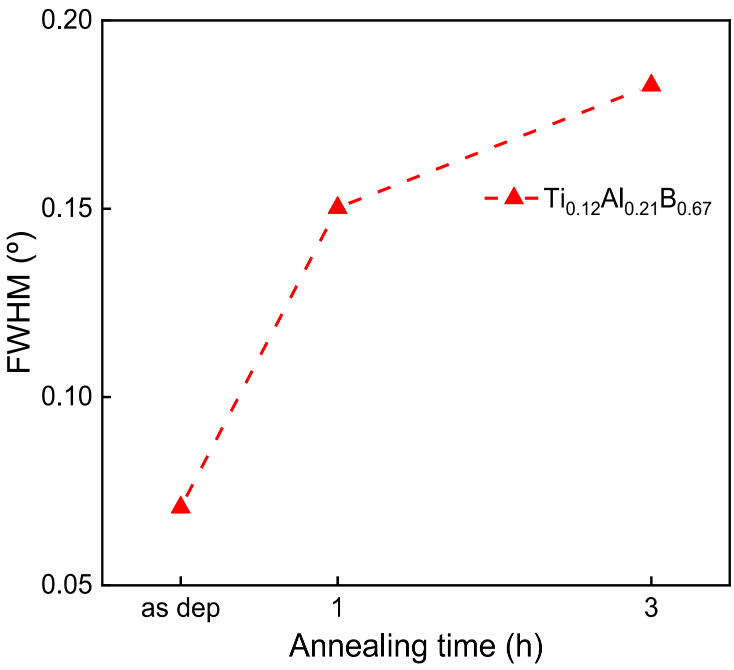

Figure 11. FWHM of the as-deposited and annealed $Ti_{0.12}Al_{0.21}B_{0.67}$ thin films at 1000 °C as a function of the annealing time.

In Figure 12, high angle annular dark field (STEM-HAADF) images with the corresponding EDX elemental maps of the as-deposited and annealed $Ti_{0.12}Al_{0.21}B_{0.67}$ thin films are shown. Figure 12 (a) displays the microstructure and elemental maps of the as-deposited thin film, in which homogenous elemental distributions of Ti, Al and B can be observed within the columns, while the intercolumnar boundaries appear to be enriched in O and Al compared to the homogenous elemental distribution within the grain. These results are in contrast with the STEM-EDX observations of Mockute et al. [120] of an as-deposited $(Ti_{0.34}Al_{0.66})B_{2.07}$ $(Ti_{0.11}Al_{0.22}\ B_{0.67})$ thin film, where surface-initiated spinodal decomposition and formation of Ti- and Al-rich nanometer-size domains were reported. This difference might be rationalized based on the different ion kinetic energy utilized during growth since a substrate bias potential of -50 V was applied in [120] compared to the floating substrate bias potential employed here.

After annealing for 1 h, see Figure 12 (b), Ti- and Al-rich $(Ti,Al)B_2$ domains with an extension ≤ 10 nm start to form in the ternary solid solution $(Ti,Al)B_2$ matrix, which is consistent with spinodal decomposition as predicted by Alling et al. [117]. After annealing for 3 h, a more pronounced segregation into Ti- and Al-rich $(Ti,Al)B_2$ domains with an extension of ≤ 20 nm can be observed in Figure 12 (c).

While the intercolumnar boundaries appeared to be already enriched with O and Al in the as-deposited state, see Figure 12 (a), likely due to residual gas incorporation during film growth [125] and/or during atmosphere exposure [127], the oxygen population within the intercolumnar boundaries increased after annealing, indicating the incorporation of oxygen from the residual gas, see Figure 12 (b) and (c) in comparison to (a). The spatially-resolved STEM-EDX data agree with global compositions measured by ERDA: While the oxygen concentration of the as-deposited film is 2.2 at.%, after annealing for 1 and 3 h, an increase to 3.6 and 4.0 at.% is obtained, respectively, see Table 2.

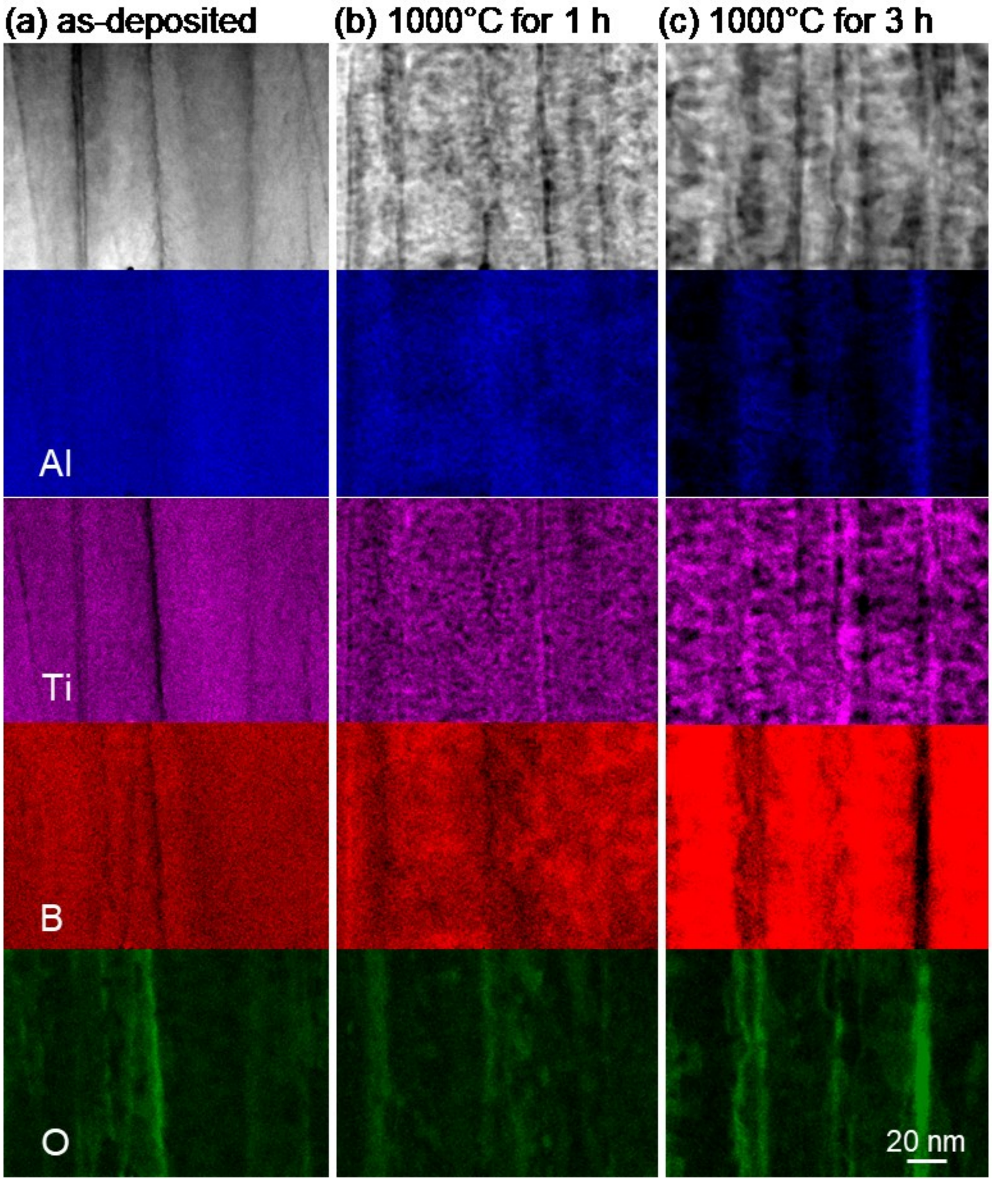

Figure 12. STEM-HAADF images and quantified EDX elemental maps, of the (a) as-deposited and annealed $Ti_{0.12}Al_{0.21}B_{0.67}$ thin films at 1000 °C for (b)1 h and (c) 3 h.

To further probe annealing induced changes in local structure, STEM imaging and selected area electron diffraction (SAED) were employed: Figure 13 (a) shows a cross-sectional image of as-deposited thin film with a columnar morphology, that is still intact after annealing at 1000 °C, see Figure 4 (c) and (e). Minute contrast differences indicate, consistent with the EDX data in Figure 12 (a), a homogeneous elemental distribution within the columns. In Figure 13 (b), the corresponding SAED pattern is indicating, consistent with the XRD data from Figure 10, the formation of the solid solution $(Ti,Al)B_2$.

Significant contrast differences associated with chemical modulations are not visible within the columns of the as-deposited thin film, see Figure 13 (a), but appear after annealing for 1 h and intensify after the 3 h anneal, see Figure 13 (c) and (e), respectively. Based on the SAED pattern presented in Figure 13 (d), the formation of AlB_{12} is indicated by the presence of low intensity (113), (201), and (211) AlB_{12} diffraction signals after annealing for 1 h in addition to the previously identified ternary solid solution. The presence of the solid solution $(Ti,Al)B_2$ can also be observed after annealing for 3 h, as well as another indication for AlB_{12} formation by (102) and (113) diffraction signals, see Figure 13 (f). The relatively low intensity of the AlB_{12} diffraction signals can be attributed to the small size of AlB_{12} crystallites as well as their low volume fraction in comparison to solid solution matrix. This observation is in consonance with the annealing temperature induced increase in FWHM depicted in Figure 11 and with the notion of continuous decomposition during annealing.

Additionally, annealing induced pore formation, see Figure 13 (c) and (e), and Figure S 7, preferentially at intercolumnar boundaries and in close proximity to the substrate (see Figure S 8), can be observed. These pores exhibit widths of up to 5 nm and lengths of up to 120 nm after 1 h and widths of up to 15 nm and lengths of up to 220 nm after 3 h, while their surface appears to be enriched in oxygen, see Figure S 7, b.

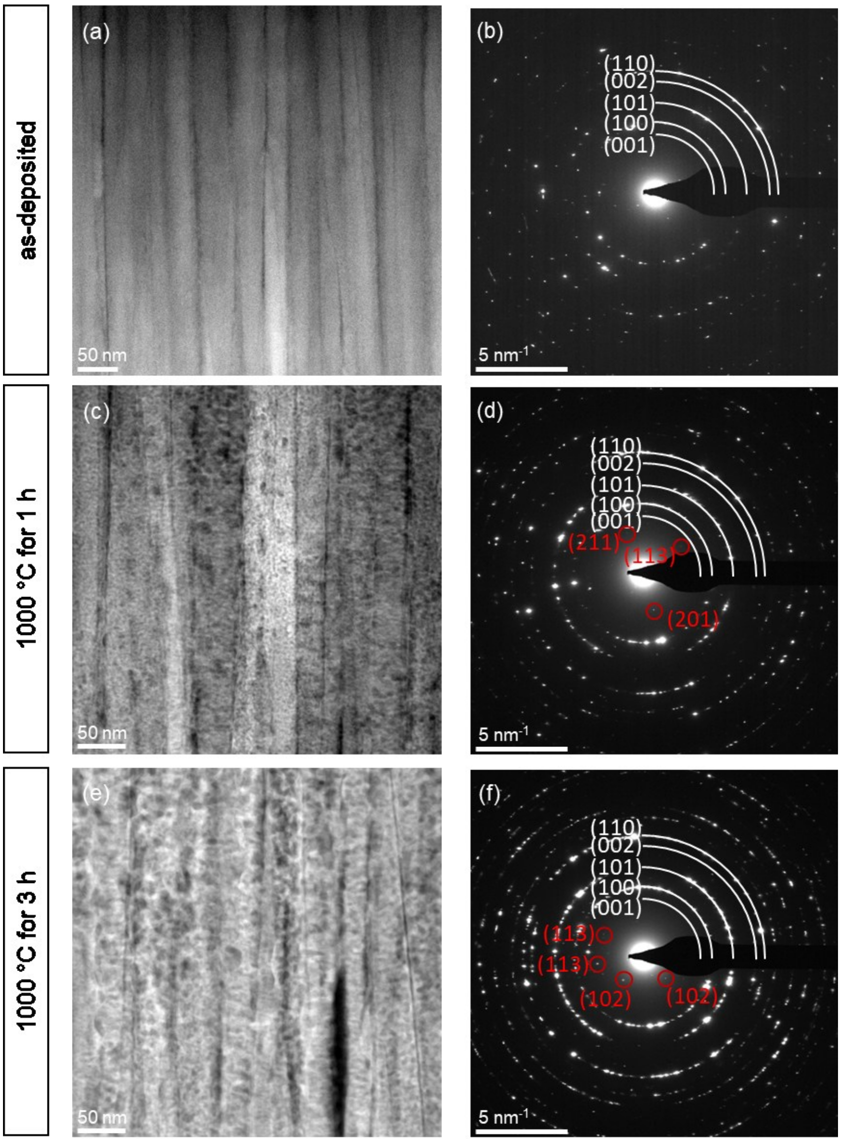

Figure 13. STEM characterization including HAADF images and SAED patterns with peak positions for TiB_2 [128] and AlB_2 [129] (white rings) and AlB_{12} [132] (red rings). (a) and (b) for the as-deposited $Ti_{0.12}Al_{0.21}B_{0.67}$, (c) and (d) after 1 h and (e) and (f) after 3 h of annealing at 1000 °C.

The local chemical composition was further studied with APT for the as-deposited as well as the vacuum-annealed films at 1000 °C for 1 h and 3 h, see Figure 14 and Figure 15. The reconstructions of Ti, Al, B and O atomic positions as well as the composition profile from the cylinder of the as-deposited film presented in Figure 14 (a), reveal the presence of O-rich regions with a size of up to 4 nm and containing up to 3 at.% O. In the distance range of 5 to 35 nm the average Ti, Al and B contents are 13.7 ± 1.4 at.%, 22.2 ±1.7 at.%, and 64.1 at.%, respectively, neglecting the average O content of < 0.2 at.%. These values correspond to an Al/(Ti+Al) ratio of 0.62 ± 0.04, Figure 15 (a).

However, deviations from the average values can be observed, which are larger than the measurement precision of ± 2 at.%. An Al-rich region is identified in the distance range of 6 to 8 nm with 11.5 ± 1.4 at.% Ti and maximum Al content of 29.9 ± 2.0 at.%, corresponding to an Al/(Ti+Al) ratio of 0.72 ± 0.04. Also, the formation of a Ti-rich region is evident in the distance range of 28 to 30 nm with 15.6 ± 1.5 at.% Ti and minimum Al content of 15.7 ± 1.5 at.%, corresponding to an Al/(Ti+Al) ratio of 0.50 ± 0.05. The Al/(Ti+Al) ratios of 0.72 ± 0.04 (Al-rich region) and 0.50 ± 0.05 (Al-deficient region) are significantly different from the average value of 0.62 ± 0.04, Figure 15 (a). The presence of 2 nm sized Al-rich and Ti-rich regions in the as-deposited sample may indicate the onset of surface diffusion mediated spinodal decomposition. The reconstruction of atomic positions as well as the composition profile from the cylinder region of the vacuum-annealed sample at 1000 °C for 1 h are presented in Figure 14 (b). B- and O-rich regions are highlighted by isoconcentration surfaces with ≥ 80 at.% B and ≥ 5 at.% O and most likely correspond to grain boundaries. Compositional modulations of Ti and Al in the distance range of 0 to 25 nm provide evidence for spinodal decomposition. Ti and Al vary periodically and anti-cyclically and maximum variations of the Al/(Ti+Al) ratio are in the range of 0.10 ± 0.02 and 0.81 ± 0.04, Figure 15 (a). The B-rich region in the distance range from 61 to 73 nm, Figure 14 (a), exhibits an average Al/(Ti+Al) ratio of 0.91 ± 0.07, Figure 15 (a), as well as an average Al/(B+Al) ratio of 0.07 ± 0.02, Figure 15 (b), which is consistent with local AlB_{12} formation.

Significant O incorporation can be observed after vacuum annealing at 1000 °C for 3 h, as highlighted by isoconcentration surfaces with ≥ 30 at.% O, Figure 14 (c). Moreover, the composition profile reveals that the Al and O contents are correlated. Based on the Al/(Ti+Al) ratio in the distance range of 0 to 25 nm, the progress of thermal decomposition is emphasized by the increased modulation wavelength of > 10 nm compared to < 10 nm in the sample annealed for 1 h, Figure 15 (a). This notion is consistent with the increase in FWHM from 0.15 to 0.18, see Figure 2 and the associated discussion. The local presence of AlB_{12} can be observed in the distance range of 25 to 27 nm with an average Al/(Ti+Al) ratio of 0.93 ± 0.03, Figure 15 (a), as well as an average Al/(B+Al) ratio of 0.10 ± 0.04, Figure 15 (b).

Therefore, the APT data reveal the spinodal decomposition of $Ti_{0.12}Al_{0.21}B_{0.67}$ annealed at 1000 °C into Ti- and Al-rich $(Ti,Al)B_2$ domains and the formation of AlB_{12} phase due to the partial decomposition of formed Al-rich $(Ti,Al)B_2$ domains to AlB_{12} phase. Spinodal decomposition during vacuum annealing, the formation of AlB_{12}, and Al evaporation have not been demonstrated in the literature previously. Mockute et al. [87] observed the formation of Ti-deficient $(Ti,Al)B_2$ precipitates within the grain interior of Ti-rich $(Ti_{0.71}Al_{0.29})B_{3.08}$ $(Ti_{0.17}Al_{0.07}B_{0.75})$, annealed at 1000 °C for 1 h, which was attributed to nucleation and growth and, hence, not to spinodal decomposition. The here observed spinodal decomposition is consistent with *ab initio* predictions by Alling et al. [117] while the here observed Al evaporation can be rationalized based on the fact that the vapor pressure of Al is 1.5×10^{-2} Pa at 1000 °C [133]. However, the formation path of AlB_{12} remains to be identified as it could be formed via decomposition of the AlB_2 phase or via Al-rich $(Ti,Al)B_2$ domains. Hence, it is evident that relying solely on XRD data for thermal stability investigations may lead to an overestimation of its thermal stability.

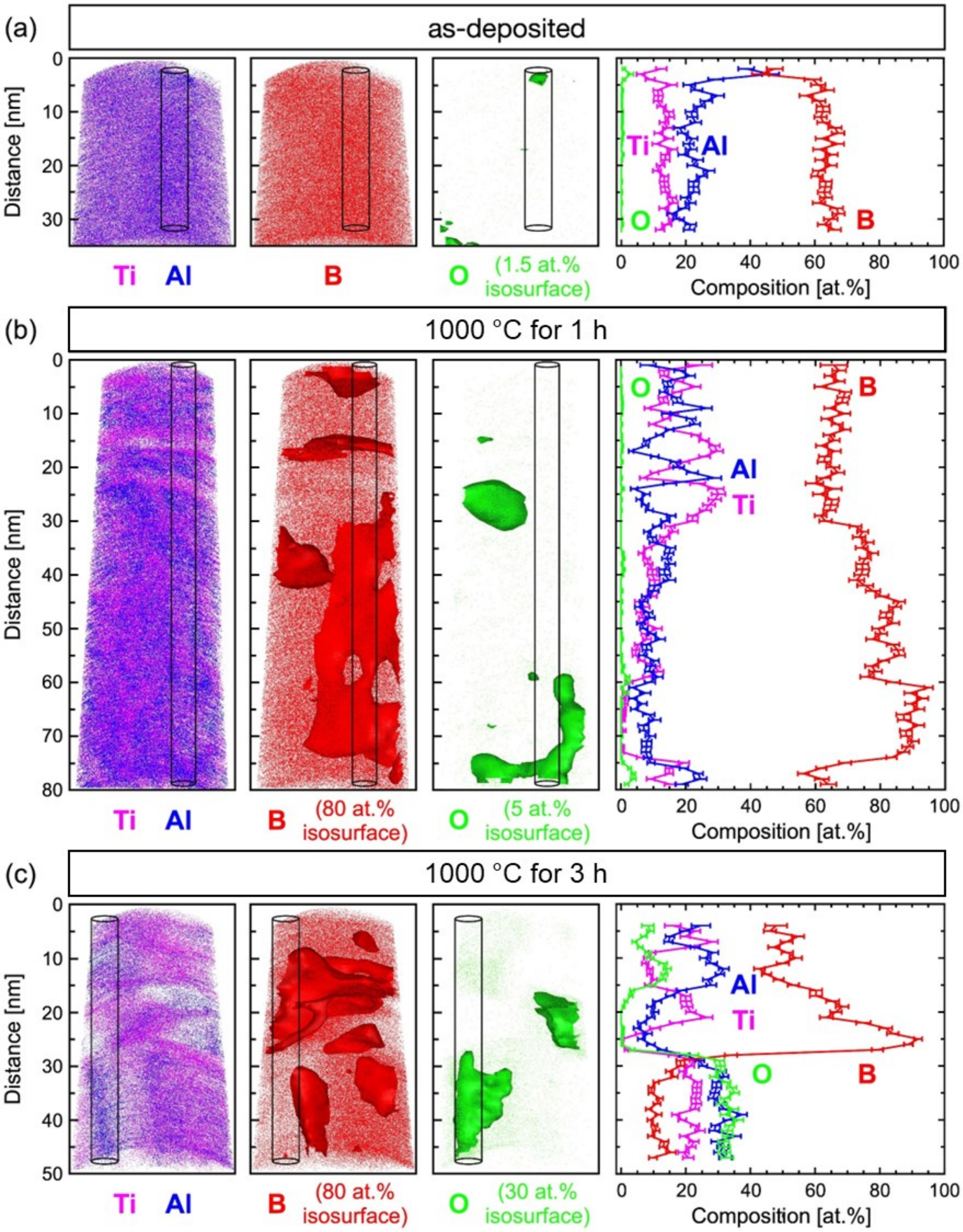

Figure 14. Spatially-resolved composition at the nanometer scale, obtained by APT. Atomic positions and composition profiles from cylindrical regions with diameter of 5 nm are shown for (a) the as-deposited state as well as after vacuum annealing at 1000 °C for (b) 1 h and (c) 3 h. The atomic positions of Ti and Al are shown together for all panels, while B-rich regions (≥ 80 at.%) are highlighted by isoconcentration surfaces in (b) and (c). Isoconcentration surfaces of O-rich regions are ≥ 1.5 at.% in (a), ≥ 5 at.% in (b) and ≥ 30 at.% in (c).

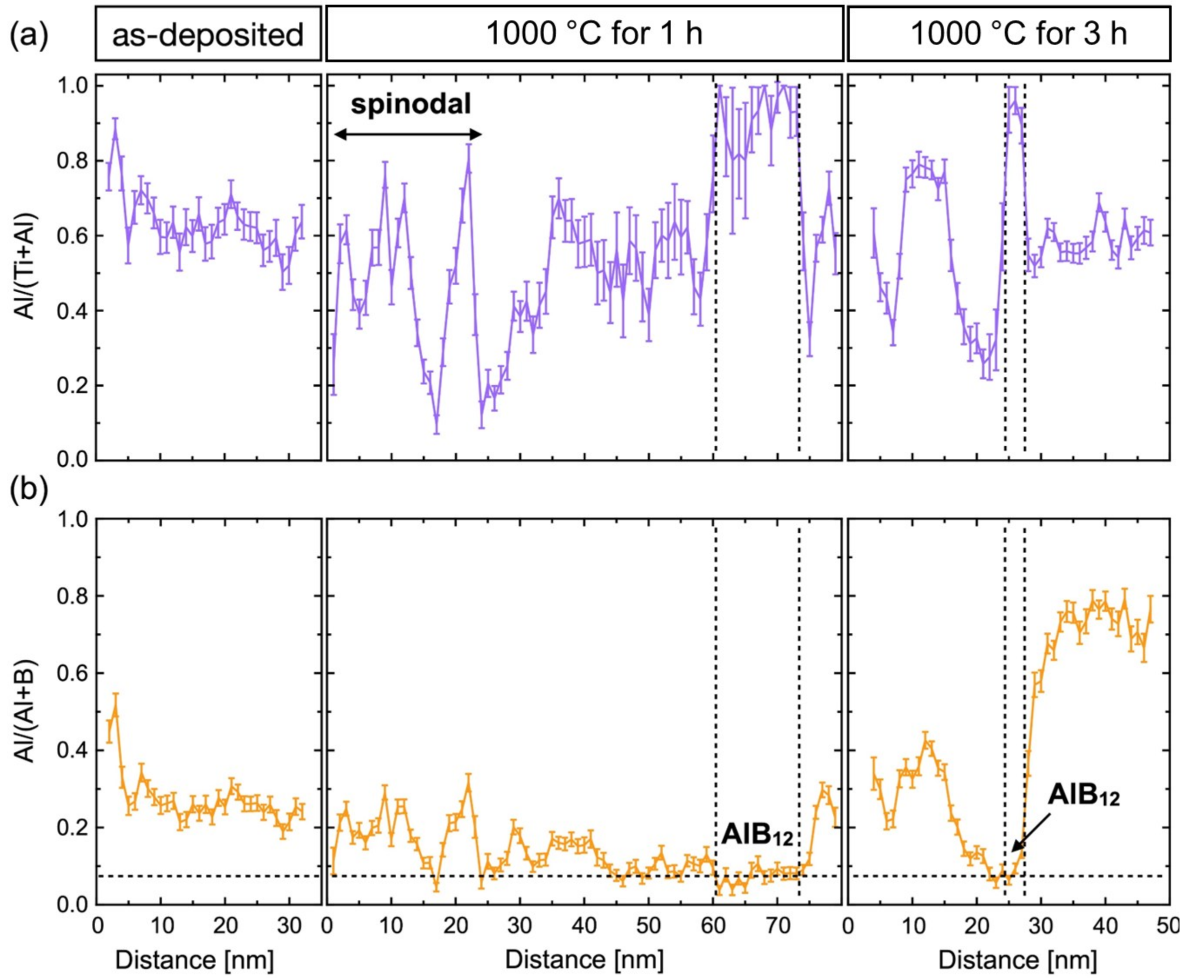

Figure 15. Evaluation of composition profiles from Figure 14 with respect to (a) Al/(Ti+Al) ratio and (b) Al/(Al+B) ratio. A spinodally decomposed region is highlighted with an arrow after vacuum annealing at 1000 °C for 1 h. Moreover, the local formation of AlB_{12} is emphasized with dashed lines after vacuum annealing at 1000 °C for 1 h and 3 h.

Formation of AlB_{12} by annealing has not been observed in thin films so far, however, it was reported in the literature for bulk materials where a glaring discrepancy exists between values reported for peritectic reaction temperature of $AlB_2 \rightarrow AlB_{12} + Al_{(l)}$, from 956 [134] to 1500 °C [135], which could be explained by different techniques of measurement, experimental conditions and concentration of impurities in the investigated samples [134-138].

To resolve the decomposition process during the annealing, *in situ* heating experiments on a $Ti_{0.12}Al_{0.28}B_{0.60}$ coated SiN-heating chip up to 1100 °C with an average heating rate of 12 K/min and a holding time of 30 minutes were performed.

During the heating process, the thin film was investigated with STEM imaging and analyzed with EDX after heating (Figure 16 (a)). After holding at 1100 °C for 30 minutes, segregation into Ti-rich (brighter regions) and Al-rich (Ti,Al)B_2 regions (darker regions, green circle) can be seen in Figure 16 (a) as well as in the temporally resolved *in situ* STEM images depicted in Figure 16 (b), (c) and (d) taken during the holding period at 1100 °C after 4, 9 and 14 minutes and the corresponding video in the supplementary material.

The delayed onset of segregation in the *in situ* experiments, compared to the previously presented annealing data, is likely caused by the higher heating rate, lower holding time and influenced by the modified film surface chemistry by atmosphere exposure as an oxygen concentration of 8 at.% was measured by EDX, compared to the 0.6 at.% in as-deposited state, measured by ERDA. The fact that the composition of the $Ti_{0.12}Al_{0.28}B_{0.60}$ film deposited onto the heating chip was Al-rich compared to the previously discussed $Ti_{0.12}Al_{0.21}B_{0.67}$ film, cannot explain the here observed delayed decomposition as according to Alling et al. [117] the driving forces for decomposition are similar for both compositions.

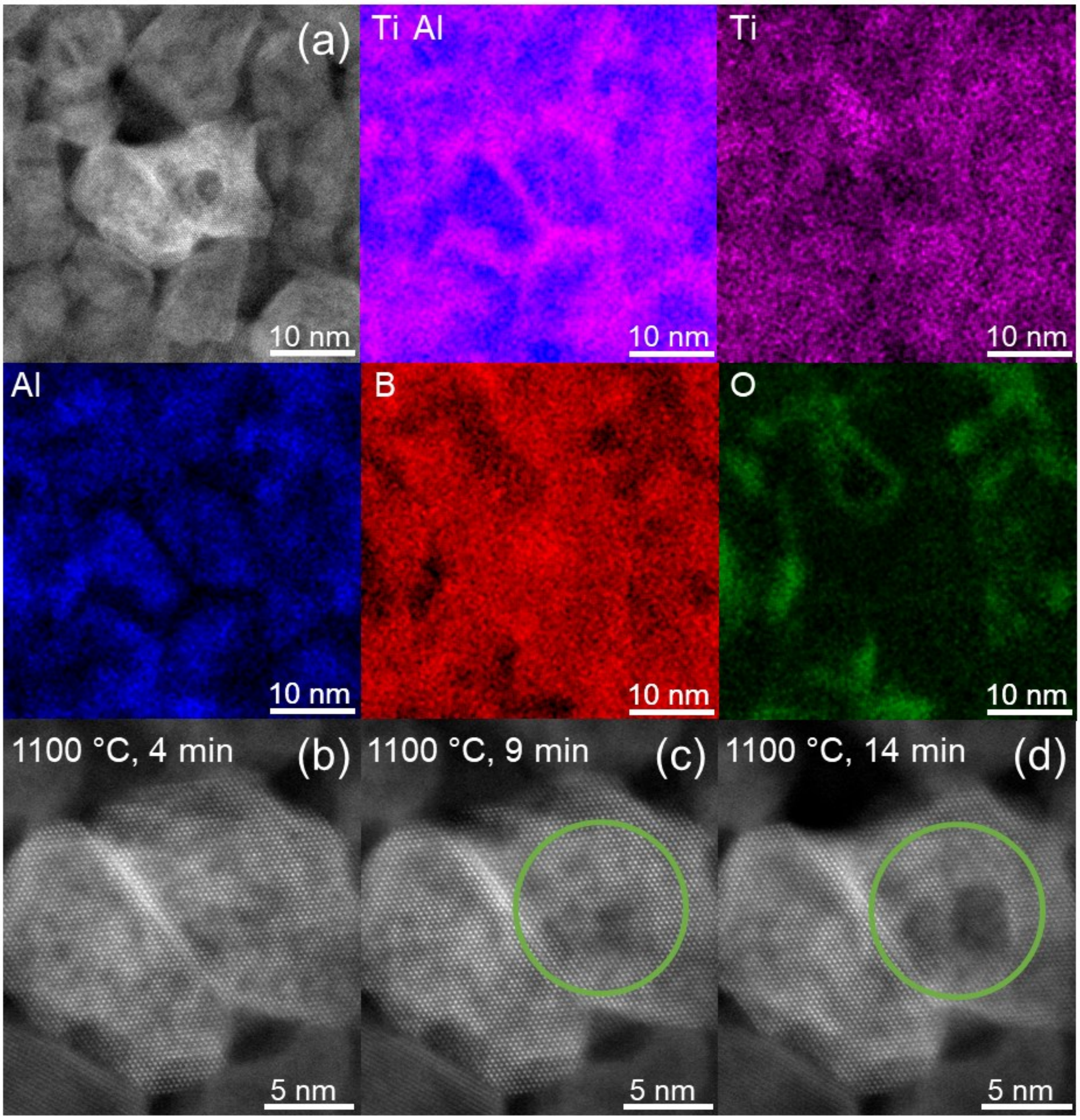

Figure 16. HADDF image and EDX map (a) after TEM *in situ* heating at 1100 °C for 30 minutes. (b)-(d) during heating at 1100 °C significant segregation of Al and Ti can be observed. In the green circle, segregation into Ti- and Al-rich regions can be observed.

4.4 Conclusions

We examined the thermal stability of magnetron sputtered $Ti_{0.12}Al_{0.21}B_{0.67}$ thin films by vacuum annealing at a temperature of 1000 °C for durations of 1 and 3 h. As-deposited and vacuum-annealed thin films were investigated regarding changes in chemical composition, phase formation, and morphology. XRD data of the as-deposited thin film indicated the formation of a solid solution.

After annealing for 1 h, the formation of Al- and Ti-rich $(Ti,Al)B_2$ domains, indicating spinodal decomposition, was demonstrated by STEM-EDX and APT data. Moreover, the formation of AlB_{12} with a concomitant reduction in Al concentration from 20.9 to 16.8 at.%, likely by evaporation, as a result of decomposition of Al-rich $(Ti,Al)B_2$ domains during annealing for 1 h was observed.

After annealing for 3 h, the observed phase separation was more distinct, and due to the continuous decomposition of Al-rich $(Ti,Al)B_2$ domains, the formation of AlB_{12}, confirmed by APT and SAED, and a reduction in the Al concentration to 12.5 at.%, revealed by ERDA, was observed. The observed decomposition products during *in situ* TEM heating experiments at 1100 °C were consistent with APT and SAED data at 1000° C. Comparison with the XRD data from Figure 10 shows that the sole reliance on XRD data for thermal stability investigation leads to an overestimation of thermal stability. Hence, the thermal stability of $Ti_{0.12}Al_{0.21}B_{0.67}$ thin films restricts the application in vacuum to temperatures below 1000 °C.

5 Contactless Health Monitoring in Autonomous Self-reporting Ceramic Coatings

5.1 Introduction

Extending the service life of components aligns materials design efforts with the United Nations Sustainable Development Goal 12, titled "responsible consumption and production" [139]. Often, materials lifetime assessments are based on statistical data in combination with safety factors [16, 17]. Depending on the width of the statistical distribution and the magnitude of the safety factor, components are taken out of service long before their actual end of life. Clearly, tracking health data of coating materials during application would enable a more sustainable material consumption as the individual component lifetime is significantly increased. Thus, employing self-reporting materials, where the unmodified material acts as a sensor, possessing a material property that has a causal relationship with structural and/or chemical changes [18], might yield significant benefits for reaching the UN's goal.

Steps in this direction have been taken by tracking changes in color [20, 21, 27, 32], photoluminescence [19, 21, 28-31], or electrical resistance [22-26] as response to mechanical loading, resulting in strain generation in polymers [27-29], composites [21, 30], liquid crystals [32], and ceramics [31], crack formation in polymers [20, 21] as well as composites [22-26], and scratches in metals [19].

Also, polymers containing a second sensing phase have been designed to report electrical degradation by color changes [140]. Chemical changes have been tracked by observing color [33-35], photoluminescence [36], or electrical resistance [18] variations in dual-phase polymers [33], polymer-metal composites [34-36], and in ceramic materials [18].

A phase separation due to heat exposure has been reported by changes in the fluorescence of polymer blends [141]. Moreover, phase changes from amorphous to a crystalline disordered solid and a subsequent phase transition to an ordered structure have been tracked by contact-based electrical resistance measurements during vacuum annealing of Cr_2AlC protective coatings [37]. It was shown that phase transitions could be related to distinct modulations of the temperature-dependent, *in situ* measured electrical resistance. Hence, Cr_2AlC serves as protective coating and at the same time as sensor for phase transitions.

From the literature review above, it is evident that self-reporting materials can convey information pertaining to mechanical loading, structural changes as well as electrical and chemical degradation.

Recently, proof of concept for tracking materials health data at temperatures > 500 °C in harsh environments has been demonstrated via resistivity measurements utilizing physical contacts attached to the monitored material surface [37]. This methodology is, however, extremely challenging to be utilized in real life applications with fast-moving components operating in harsh environments. We therefore propose a simple contactless method for gauging the materials health status of $Cr_{0.34}Al_{0.31}B_{0.35}$ coatings (Figure 17), without the need for a secondary sensor phase, revealing phase transitions due to high-temperature exposure by modulations in electrical resistance. We verify contactless-obtained data by comparison to well-established contact-based resistance measurements as well as *in situ* and *ex situ* structural and chemical analyses. Hence, we demonstrate the proof of concept for contactless tracking of materials health-relevant data, namely multiple phase transitions occurring between room temperature and 800 °C.

5.2 Principle of Contactless Phase Transition Detection

Annealing of amorphous $Cr_{0.34}Al_{0.31}B_{0.35}$ coatings (Figure 17a) triggers two amorphous to crystalline phase transitions: Between 400 and 500 °C, the formation of the Cr_2AlB_2 MAB phase, a member of the nanolaminated transition metal borides, whereby M corresponds to an early transition metal, A for an A-group element and B for Boron, is inferred, see Figure 17b and supplementary information Figure S 16 - Figure S 18, and between 500 - 600 °C, the formation of the Cr_3AlB_4 MAB phase is detected, see Figure 17c. These observations are consistent with contact-based and contactless normalized resistance measurements, calorimetry, and spatially resolved structure analysis, which are in very good agreement. Accelerated growth of Cr_2AlB_2 and Cr_3AlB_4 from the amorphous precursor phase is observed between 600 and 700 °C (Figure 17d). Between 700 and 800 °C, the complete transformation of the amorphous phase into crystalline Cr_2AlB_2 and Cr_3AlB_4 MAB phases as well as into liquid Al is inferred, see Figure 17e. Hence, we show proof of concept for remote tracking of complex combinations between phase transitions and grain growth by contact-based resistance measurements as well as by contactless resistance measurements, which are in excellent agreement with the former (Figure 17f). We envision that contactless tracking of materials health data in harsh environments and on complex-shaped components will extend the service life thereof and hence enable more sustainable materials consumption.

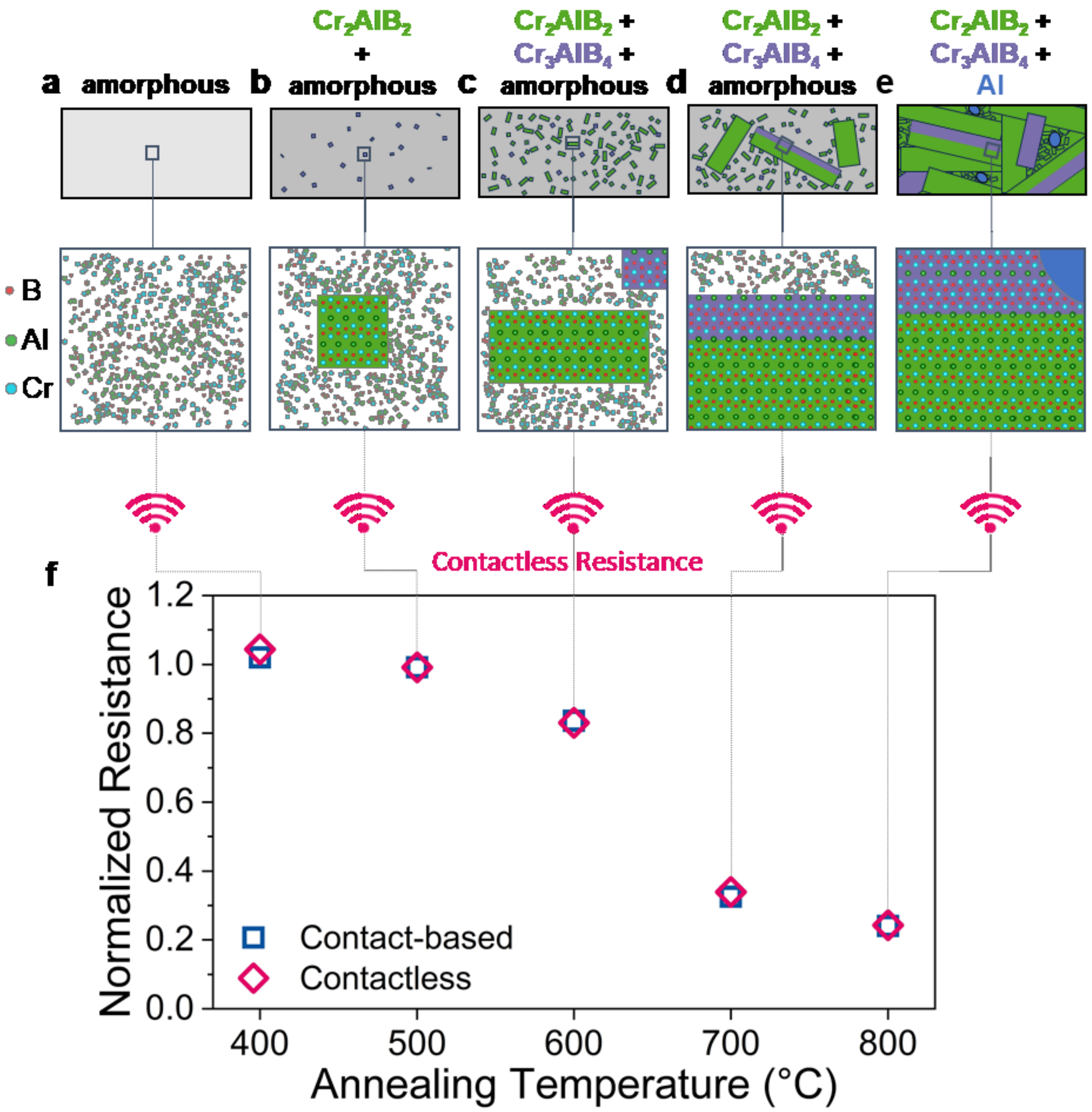

Figure 17. Schematic illustration of crystal structure and grain size after annealing (a-e). Contact-based and contactless measured, normalized resistance versus annealing temperature (f) showing a crystal structure and grain size dependent resistivity decrease with increasing annealing temperature. Resistance data are normalized with respect to their initial value before annealing.

5.3 Referencing with Contact-based Resistance and Calorimetry

To demonstrate the proof of concept for contactless tracking of temperature-dependent materials health data, calorimetric data, indicating three phase transitions, is compared to the normalized *ex situ* measured contactless resistance and the normalized *in situ* measured contact-based resistance, see Figure 18g. The maximum deviation between contact-based and contactless measured resistance data is 4% and hence, they exhibit very good agreement (Figure 17f, supplementary information Figure S 10). Therefore, we refer to both, contactless and contact-based measured resistance values simply as resistance. Resistance measurements between room temperature and 400 °C reveal a negative thermal coefficient of resistance (TCR), characteristic for glassy structures [142, 143]. Subsequently, at ~450 °C, the temperature dependent resistance signal exhibits a pronounced change in slope, as revealed by the non-linear behavior of the first derivative of the measured resistance with temperature (dR/dT vs. T). Over the whole, here investigated temperature range, three well defined peaks in dR/dT vs. T can be seen. Interestingly, the onset and peak temperatures in dR/dT vs. T show, with maximum deviations of 7 and 18 °C, excellent agreement with the corresponding temperatures as obtained from calorimetry, see Figure 18g. The significance of this observation for tracking materials health data with resistivity measurements is highlighted by the corresponding structural analysis data from high-resolution scanning transmission electron microscopy (HRSTEM, *ex situ* Figure 18a-f, *in situ* Figure 20), selected area electron diffraction (SAED, Figure 19, supplementary information Figure S 12) and X-ray diffraction (XRD, supplementary information Figure S 13). The average chemical composition of the films was not significantly altered by the annealing as is evident from elastic recoil detection analysis (ERDA, supplementary information Figure S 11). The slight offset measured between the calorimetric data and the temperature-dependent resistance data can be rationalized by differences in sample nature and experimental protocol: for the resistance measurement a thin film on a substrate was heated in vacuum, while the calorimetry measurements were conducted on powder samples in an Argon atmosphere.

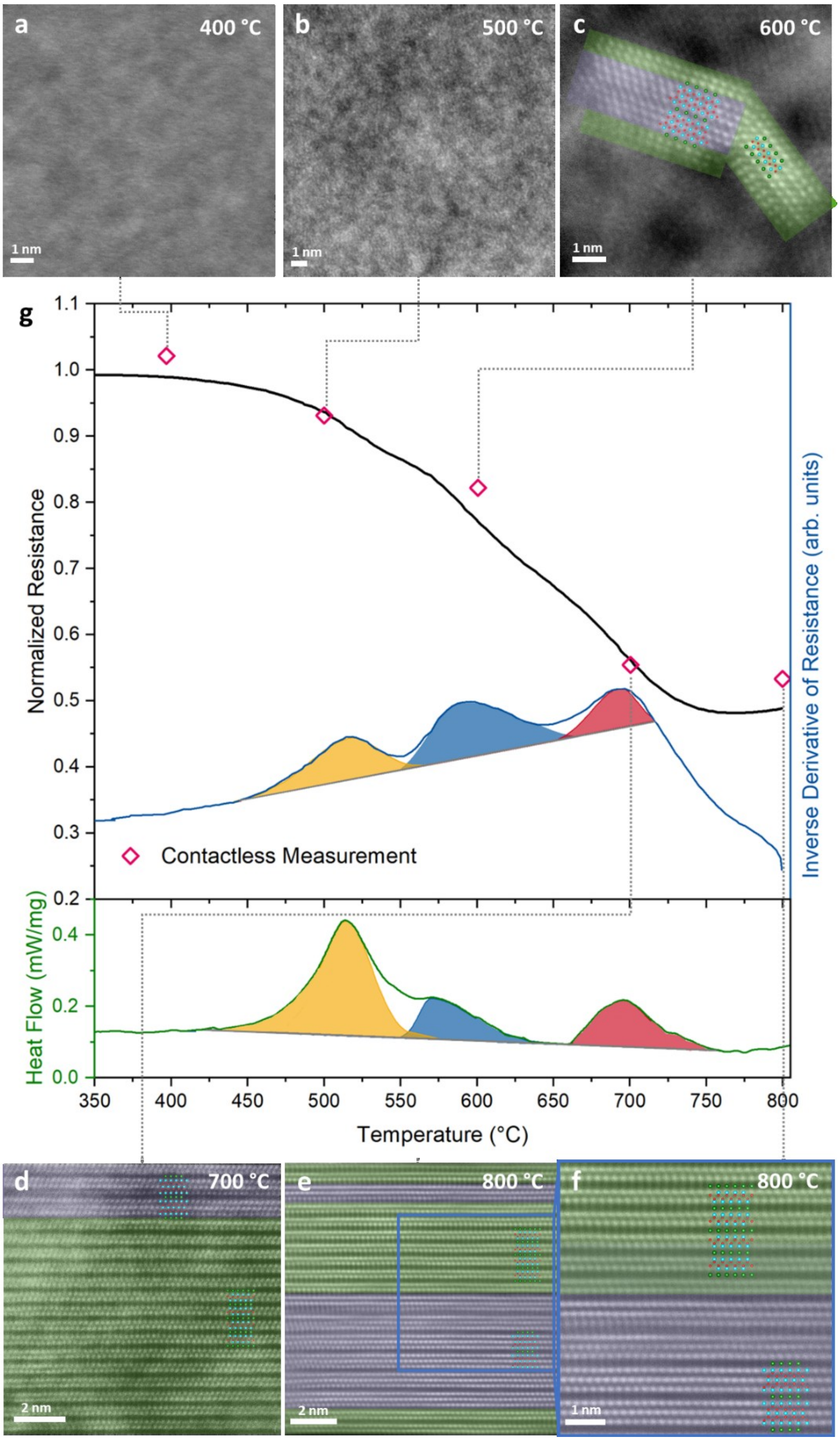

Figure 18. *Ex situ* HRSTEM images with overlays of ideal structures (blue atoms corresponding to Cr, green atoms to Al, and red atoms to B) and colored areas where Cr_2AlB_2 (green) and Cr_3AlB_4 (purple) are identified (a-e). A higher magnification image of the region marked in blue borders in e is shown in f. *In situ* contact-based measured resistance normalized with respect to its initial room temperature value (black curve, top) and the derivative dR/dT versus temperature (blue curve, top) along with contactless measured resistance (magenta diamonds) measured at room temperature and multiplied with the thermal coefficient of resistance determined for the respective sample and calorimetric measurement

(green curve, bottom) (g). Peaks in the calorimetric data as well as in dR/dT versus T were colored as a guide for the eye.

While up to 400 °C, no evidence for phase transformations can be inferred from HRSTEM and *in situ* SAED measurements (Figure 19b and d, supplementary information Figure S 12), the onset of a first transformation is identified by a change in the *in situ* SAED peak shape at 450 °C between 1.5 and 3 Å, see Figure 19d and supplementary information Figure S 14. A decrease in diffracted intensity at $d < 2.25$ Å in combination with an intensity increase at $d > 2.25$ Å, signaling a shift towards peak positions indicating formation of crystalline phases. This interpretation is consistent with the temperature dependent crystallization depicted in the diffractograms shown in supplementary information Figure S 12. Moreover, evidence for nucleation of a crystalline phase can be seen in the HRSTEM image of the sample annealed to 500 °C, see Figure 18b. A more detailed analysis of phase formation, based on XRD and SAED, given in the supplementary information infers the formation of Cr_2AlB_2 at these temperatures (supplementary information Figure S 15 - Figure S 17). These characteristic manifestations of an amorphous - crystalline phase transition coincide with both, the onset of the first peak identified in the dR/dT signal as well as the onset of the first enthalpic peak in the calorimetric data, see orange colored region in Figure 18g at 451 and 458 °C, respectively. Hence, changes in dR/dT vs. T indicate the onset of phase transitions. Moreover, as the peak position of dR/dT vs. T at 518 °C aligns with the first peak of the DSC signal at 515 °C, it is evident that dR/dT vs. T tracks the amorphous to crystalline phase transition in $Cr_{0.34}Al_{0.31}B_{0.35}$ coatings.

A second transformation is indicated by the blue colored region in Figure 18g displaying calorimetric data with onset and peak temperatures of 548 °C and 572 °C, respectively. The HRSTEM micrograph in Figure 18c shows a crystallite containing Cr_3AlB_4 and Cr_2AlB_2 domains, consistent with the *in situ* SAED data displayed in Figure

19d at 600 °C. These observations also concur with *in situ* HRSTEM data, as displayed in Figure 20d, as well as with *ex situ* XRD data as shown in supplementary information Figure S 13. The formation of Cr_3AlB_4 at these temperatures is further inferred from the more detailed phase formation analysis given in supplementary information Figure S 15 - Figure S 17. The above discussed onset and peak temperatures obtained by calorimetry, indicating the 2nd transition, coincide with the onset and peak temperatures in dR/dT vs. T at 551 °C and 590 °C, respectively. Hence, dR/dT vs. T was demonstrated to track both phase transformations discussed so far.

A third transformation is indicated in the red colored region in Figure 18g, displaying DSC data with onset and peak temperatures of 660 °C and 696 °C, respectively. From the comparison of *in situ* HRSTEM micrographs, Figure 20, taken during annealing at 600 °C (Figure 20d), 700 °C (Figure 20e), and 750 °C (Figure 20f), it is evident that the observed peak in DSC data corresponds to accelerated grain growth is occurring in this temperature regime, as has been shown before for nanocomposite TiB_xN_y and TiB_xC_y coatings [144, 145] as well as nanocrystalline Cu powders [146]. Furthermore, the video recorded at 750 °C (supplementary information Figure S 18) supports this interpretation, showing atomic scale, layer-by-layer growth of a crystal containing intergrown structures of both Cr_2AlB_2 and Cr_3AlB_4 MAB phases, similar to what has been observed for $(Mo,Cr)_2AlB_2$ [147] and MoAlB MAB phases [148-150]. Hence, based on *in situ* HRSTEM investigations, it is inferred that accelerated grain growth is causing the exothermal reaction captured in the corresponding calorimetric data set. Further supporting evidence for the above observed accelerated grain growth of both Cr_3AlB_4 and Cr_2AlB_2 is obtained by comparing the HRSTEM micrographs obtained after annealing to 600 °C, see Figure 18c, to the 700 °C anneal shown in Figure 18d. Also, the SAED data displayed in Figure 19d and the XRD data shown in supplementary information Figure S 13 are exhibiting significant peak intensity increases and concomitant decreases in full-width at half maximum for Cr_3AlB_4 and Cr_2AlB_2 diffraction signals and are therefore consistent with the grain coarsening notion. This accelerated reaction can be rationalized based on melting of excess Al, present since the overall chemical composition contains 33 at.% Al while the 212 and the 314 phase only contain 20 at.% and 12.5 at.%, respectively. In Figure S 10, the DSC heating curves for repeated heating cycles of one sample are shown. In the first three heating cycles depicted by the blue (1st cycle), green (2nd cycle) and yellow (3rd cycle), exothermic signals indicate the crystalline amorphous transition as discussed above, consistent with the DSC data presented in Figure 2. The DSC data of the 4th heating cycle (red curve) indicates that the amorphous to crystalline transition was completed during the first 3 heating cycles as an endothermic peak at ~ 640 °C, which coincides with the melting point reported for Al (659 °C) [151], is visible. The small endothermic peak is concealed by the exothermic signal associated with the amorphous to crystalline transition tracked in a single heating run as it takes place simultaneously, see Figure 2. This notion is supported by the peaks corresponding to elemental Al visible in the XRD after cooling (Supplementary Figure S 13). After the third transformation, the previously decreasing trend of resistance is reversed since grain growth and phase formation have been completed leading to a now positive TCR as expected for MAB phases [152-154].

As for both above discussed phase transitions, the agreement for the third transition, marked in red in Figure 18g, between dR/dT vs. T and the DSC data sets regarding onset and peak position temperatures is, with a maximum deviation of 5 °C, very good.

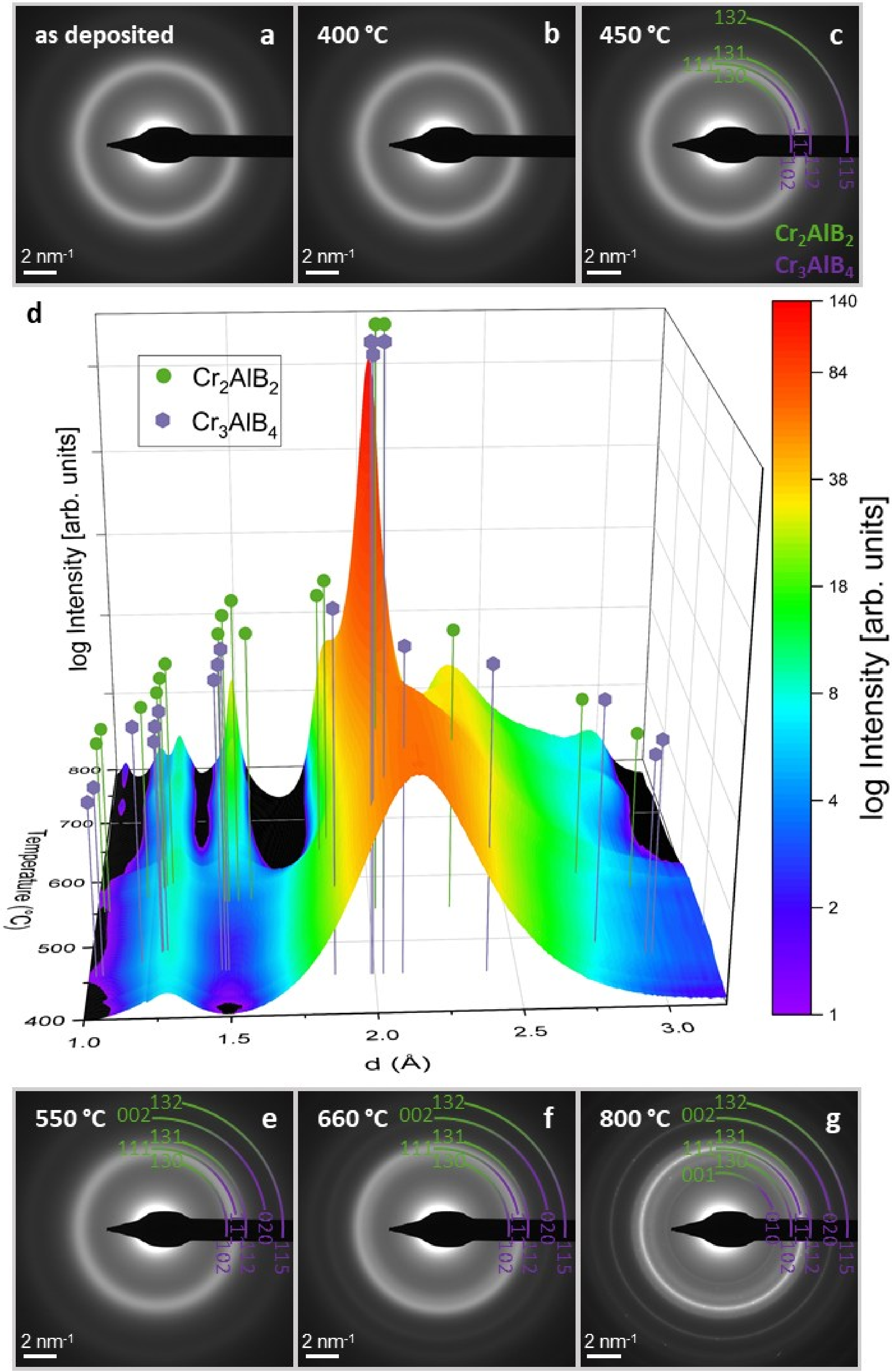

Figure 19. *In situ* SAED patterns (a-c, e-g) and the corresponding integrated intensity plotted with respect to temperature (d). Peak positions of Cr_2AlB_2 and Cr_3AlB_4 are indicated. A first transformation is

visible at 450 °C (see supplementary information Figure S 14) with subsequent emergence of peaks corresponding to Cr_2AlB_2 and Cr_3AlB_4.

Hence, we have demonstrated that three different phase transformations can be tracked by *in situ* contact-based resistance measurements. Furthermore, *ex situ* contactless electrical resistance measurements mirror the trend displayed by the contact-based measurement: The agreement between both methods, displayed in Figure 17f, is excellent as the differences are ≤ 4 % for the entire here investigated temperature range. Thus, by relating periodic contactless measurements to the preceding structural analysis, the current state of the material can be inferred. Therefore, the proof of concept for contactless materials health tracking has been demonstrated. Other potential candidates for application include, for example, TiAlN thin films, that show different recovery processes, phase transitions and spinodal decomposition as observed by DSC measurements [155]. Especially the technologically-relevant decomposition would be of interest due to the large difference in the electrical resistivities of the binary nitrides TiN and AlN, which is also expressed in a close to exponential increase in the resistivity of TiAlN upon Al addition for an Al content between 7.9 and 51.5 at.% [156]. As the electrical resistance of materials is generally affected by changes in the environment, materials health data tracking can be envisioned for a wide range of applications in harsh environments, where physical and/or chemical changes are triggered by mechanical, thermal, or chemical stressors.

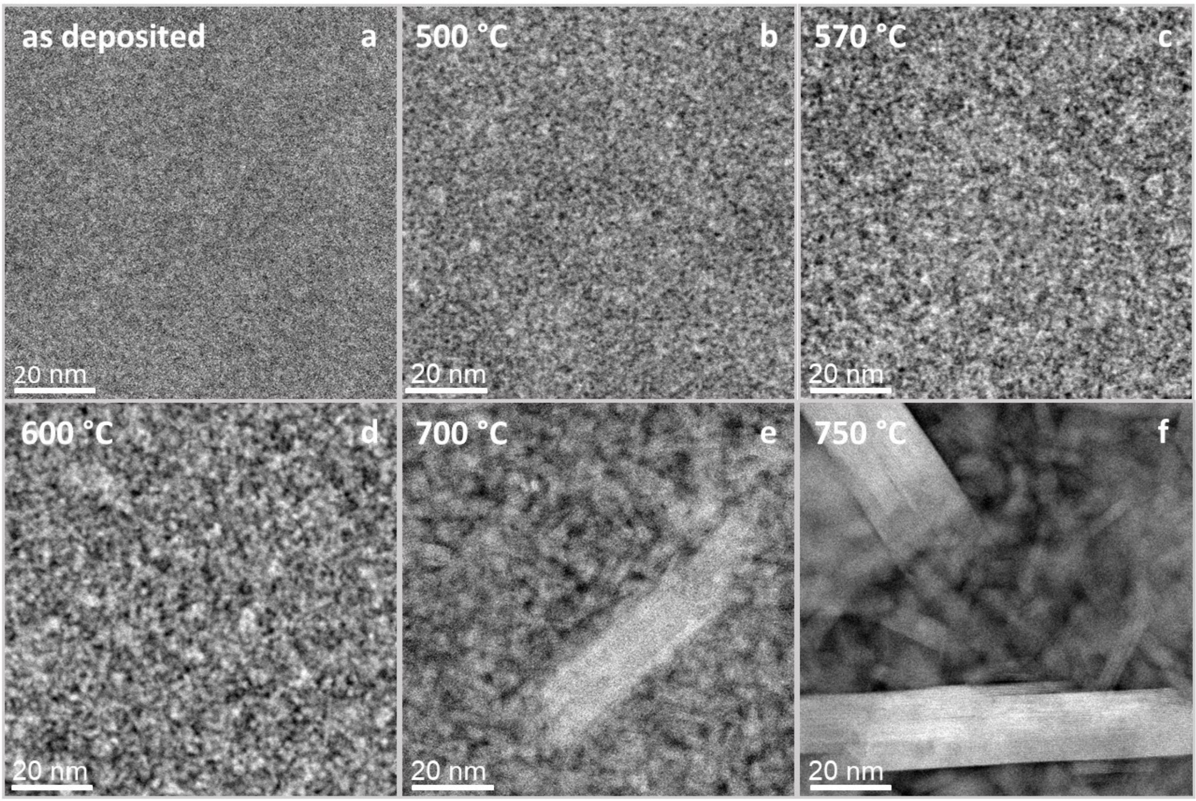

Figure 20. HRSTEM micrographs taken during *in situ* annealing at indicated temperatures (a-f). The amorphous as deposited structure becomes partly crystalline after 500 °C, whereby MAB phase formation is observed, with a significant increase in crystal domain size after 700 °C.

While the contact-based measurement required four physical contact wires attached to the sample surface and measurement times of about 30 seconds per data point, the contactless measurement time is around 1 second. Considering that it is a mechanical and electrical engineering exercise to integrate contactless resistance measurement technology into complex shaped coated components, the dynamic assessment of dR/dT vs T at high speeds in harsh environments appears feasible from a fundamental science perspective. We envision that materials health monitoring by contactless electrical resistance measurements enables a more sustainable materials usage as the individual remaining component lifetime is assessed and can replace component operation relying on safety factor-based design.

5.4 Conclusions

In summary, amorphous $Cr_{0.34}Al_{0.31}B_{0.35}$ coatings were annealed in vacuum and three phase transformations were identified. It was shown that these phase changes can be tracked with *in situ* contact-based as well as *ex situ* contactless resistance data via comparison to XRD, DSC, ERDA as well as *ex situ* and *in situ* HRSTEM and SAED data measured in the corresponding temperature ranges. The contactless resistance data are, with deviations ≤ 4 %, in excellent agreement with contact-based resistance data. Therefore, it is demonstrated that contactless resistance data are useful for assessing materials health by tracking structural changes in $Cr_{0.34}Al_{0.31}B_{0.35}$ coatings. Contactless resistance tracking can in principle be integrated into coated components operating at high speeds in harsh environments and is thereby expected to enable a more sustainable usage, as the individual remaining component lifetime is tracked, replacing component operation based on designs utilizing safety factors.

5.5 Methods

Synthesis of Cr-Al-B thin films

Amorphous Cr-Al-B thin films were synthesized by direct current magnetron sputtering (DCMS) without intentional heating in a high vacuum deposition system with a base pressure below $9 \cdot 10^{-7}$ mbar. A 2” ternary 1 : 1 : 1 Cr : Al : B target (Plansee Composite Materials GmbH, Lechbruck am See, Germany) was run at a constant power of 120 W facing the floating single crystalline 10 x 10 cm Al_2O_3 (0001) substrate at a distance of 10 cm. An argon pressure of 0.3 Pa and a deposition time of 60 min led to films with a thickness of ~ 0.8 µm.

Electrical resistance measurements

Contact-based electrical resistance was measured using the Van-der-Pauw method [51, 52]. The *in situ* measurement setup utilized here was identical to previous experiments and is described in more detail elsewhere [18, 37]. The heating and cooling rate was kept constant at 10 Kmin^{-1} while the pressure in the vacuum furnace was below $5 \cdot 10^{-6}$ mbar. To determine significant changes in R vs. T, the first derivative of the resistance was computed with respect to T (dR/dT). The onset and peak temperatures of dR/dT vs. T were fitted by using a bi-gaussian function [157]. The thermal coefficient of resistance (TCR) was extracted from the linear slope of the cooling curves.

Contactless resistance was determined using Eddy-current measurements carried out *ex situ* for samples annealed to the indicated temperatures in an EddyCus TF lab 2020SR (SURAGUS GmbH, Dresden, Germany) performing self-referencing before every measurement session. For each sample, two measurements were averaged to obtain the sheet resistance R_S, which was then used to calculate the resistivity (ρ) by multiplying it with the film thickness (d) according to $\rho = R_S \cdot d$. The highest determined variation for repeated measurements of one sample was < 0.6 %.

X-ray diffraction

Phase formation was studied by Bragg-Brentano X-ray diffraction (XRD) in a Panalytical Empyrean MRD diffractometer (Malvern Panalytical, Almelo, The Netherlands) equipped with a Cu Kα source and operated at a current of 40 mA and a voltage of 40 kV. Scans were recorded with a − 5° omega offset scan with a step size of 0.026° and a measurement time of 100 s/step. Powder diffraction files (PDF) of Cr_2AlB_2 (01-084-8899), Cr_3AlB_4 (01-084-8900), and Al (04-0787) were used for phase identification.

Crystallization kinetics

Crystallization kinetics were studied by differential scanning calorimetry (DSC) in a Jupiter® STA 449 C (Netzsch GmbH, Selb, Germany) with a continuous heating mode (heating rate 10 $Kmin^{-1}$) in Ar atmosphere (purity 99.9999%). Low oxygen content (<1 ppm) in the atmosphere was ensured by the integrated oxygen trap system (OTS®). Temperature and sensitivity were calibrated by melting high purity standards (≥99.9%) (Zn, Sn, Al, Ag, Au, Pd) and the onset temperatures of the reactions were extracted using the tangent method [158]. As a guide for the eye, the exothermal peaks were schematically colored in the graphical representation. The powder for the experiments was generated by deposition of a film on a NaCl substrate and subsequent dissolution thereof [159].

Compositional analysis

The chemical composition depth profile of the films was quantified by time-of-flight elastic recoil detection analysis (ToF-ERDA) at the Tandem Accelerator Laboratory of

Uppsala University [121] using a 36 MeV $^{127}I^{8+}$ primary beam. The angle between the primary beam and the detector telescope was 45°, while the incidence and exit angles of the primary ions and detected recoils with respect to the film surface were 22.5°. Energy discrimination was done by using a gas detector system [123] and the time-of-flight was determined with thin carbon foils [122]. Depth profiles were obtained from time-energy coincidence spectra using CONTES [160]. The films were found to be homogeneous and average concentrations were calculated from the depth profiles, while the oxygen-rich surface-near region was excluded. For B, a maximum total uncertainty of 5 % of the determined values is assumed, and aliquot fractions thereof for the metals Cr and Al.

High-resolution analysis

Thin lamellae (< 100 nm) for high-resolution scanning transmission electron microscopy (HRSTEM) investigations were prepared by focused ion beam (FIB) techniques in a Helios 5 Hydra UX dual-beam microscope (Thermo Fisher Scientific, Waltham, USA). Xe^+ ions were employed at 30 kV for the standard lift-out procedure onto an omniprobe lift-out grid. Thinning of the lamellae was carried out with Ga^+ ions in a Helios Nanolab 600 dual-beam system (Thermo Fisher Scientific, Waltham, USA). These lamellae were subsequently analyzed in a Titan Themis 200 G3 equipped with a SuperX EDX detector (Thermo Fisher Scientific, Waltham, USA) at an acceleration voltage of 200 kV.

For *in situ* HRSTEM as well as selected area electron diffraction (SAED) heating experiments, Wildfire nano-chips (DENS Solutions, Delft, The Netherlands) were coated with < 50 nm of the Cr-Al-B in equivalent conditions to all other films. For the SAED experiments, a constant heating rate of 10 K min^{-1} was applied, while for the HRSTEM imaging, the annealing was interrupted by quenching at specific temperatures to further investigate critical events. The integrated SAED patterns were post-processed for the 3-dimensional graph by partly subtracting an as deposited spectrum as well as the background to showcase the changes induced by annealing. Furthermore, the spectra were corrected for the thermal expansion during the measurement. For phase identification, PDF of Cr_2AlB_2 (01-084-8899) and Cr_3AlB_4 (01-084-8900) were used.

6 Contactless Tracking of Decomposition in Self-reporting Ceramic Cr-Al-B Coatings

6.1 Introduction

Today, the assessment of materials service life is often based on statistical data, where, based on the corresponding safety factors, components are replaced prematurely before the end of their individual lifetimes [16, 17]. Hence, tracking of materials health data during application would enable more sustainable materials consumption as the individual component lifetime could be utilized.

Self-reporting behavior has been shown by tracking changes in photoluminescence [21, 28-30], color [20, 21, 27], or electrical resistance [22-26] resulting from strain generation [21, 27-30] as well as crack formation [20-22, 24] in polymers [20, 27-29] and composites [21-26, 30]. Moreover, color [32] and photoluminescence [19, 31] have been related to the emergence of strain in liquid crystals [32] and ceramics [31] as well as scratches in metals [19]. Furthermore, electrical resistance measurements [37] have been used to track phase changes in ceramic coatings [37].

The ability for self-reporting is often based on introducing a sensor material into a matrix. For polymer-based composites, color changes of molecular indicators blended into a polymer have been shown to report electrical degradation via a chromogenic response to oxygen radicals, which are formed during the degradation process [140]. Moreover, chemical changes have been tracked through color variations induced by swelling of a hydrogel polymer manufactured by combining colloidal crystal templating and molecular imprinting, which was subjected to different protein solutions [33]. Polymer-metal composites [34-36] have been employed to track chemical changes by observation of color [34, 35] or photoluminescence modulations [36] resulting from reaction with Fe^{2+} from the underlying steel [34] or pH-sensitivity [35, 36].

Moreover, tracking changes in fluorescence caused by exposure to heat have been used to monitor a phase separation in polymer blends [141], while contact-based electrical resistance measurements have been used to track chemical changes caused by oxidation of TiN hard protective coatings [18] as well as in V_2AlC MAX phase thin films [161]. For TiN, temperature- and time-dependent *in situ* electrical resistance tracking was used to predict the unoxidized, remaining film thickness [18], which is relevant to assess the remaining lifetime. Hence, TiN served as protective coating and, at the same time, as oxidation progress sensor. For V_2AlC thin films, it was shown that the oxidation progression could be qualitatively related to the increase in electrical resistance measured after oxidation at different times and temperatures [25]. The decomposition in an Al-Mg-Si-Cu alloy [162] and in (Ti,Al)N [163] as well as the formation and decomposition of natural gas hydrate have also been monitored using electrical resistivity data acquired via physical contacts [164].

The recent advancements in tracking materials health data at temperatures higher than 500 °C in harsh environments via resistance measurements utilized physical contacts attached to the material [18]. Implementing tracking strategies based on physical contacts in non-stationary applications would pose formidable engineering challenges.

Thus, we demonstrate that thermally triggered decomposition reactions in $Cr_{0.34}Al_{0.31}B_{0.35}$ coatings can be tracked by contactless-acquired electrical resistance data. As the decomposition progress can be related to changes in electrical resistance, the health state of materials can be monitored with the method proposed here.

6.2 Results and Discussion

Figure 21 shows structural analysis data obtained by X-ray diffraction (XRD) (Figure 21a, supplementary material Figure S 20) along with results of the compositional analysis obtained by elastic recoil detection analysis (ERDA) for samples annealed to the indicated temperatures (Figure 21b). While the overall chemical composition of the coating is determined to be $Cr_{0.34}Al_{0.31}B_{0.35}$, the XRD data are consistent with the formation of the Cr_2AlB_2 and Cr_3AlB_4 MAB phases in the sample annealed at 800 °C. This is in agreement with high-resolution scanning transmission electron microscopy (HRSTEM) micrographs (Figure 22a) as well as density functional theory (DFT) calculations, predicting negative free Gibbs energies of formation for both Cr_2AlB_2 and Cr_3AlB_4, when compared to the constituting elements and also compared to the competing phases CrB, CrB_2, and Cr_3B_4 (supplementary material Figure S 21). Furthermore, Cr_2AlB_2 and Cr_3AlB_4 are energetically preferred compared to the CrAlB phase [147, 153]. Segregation of Al, observed both by XRD, see Figure 21a, as well as in energy-dispersive X-ray spectroscopy (EDX) maps, shown in Figure 23a, can be rationalized based on the fact that the film composition is Al-rich compared to both MAB phase compositions.

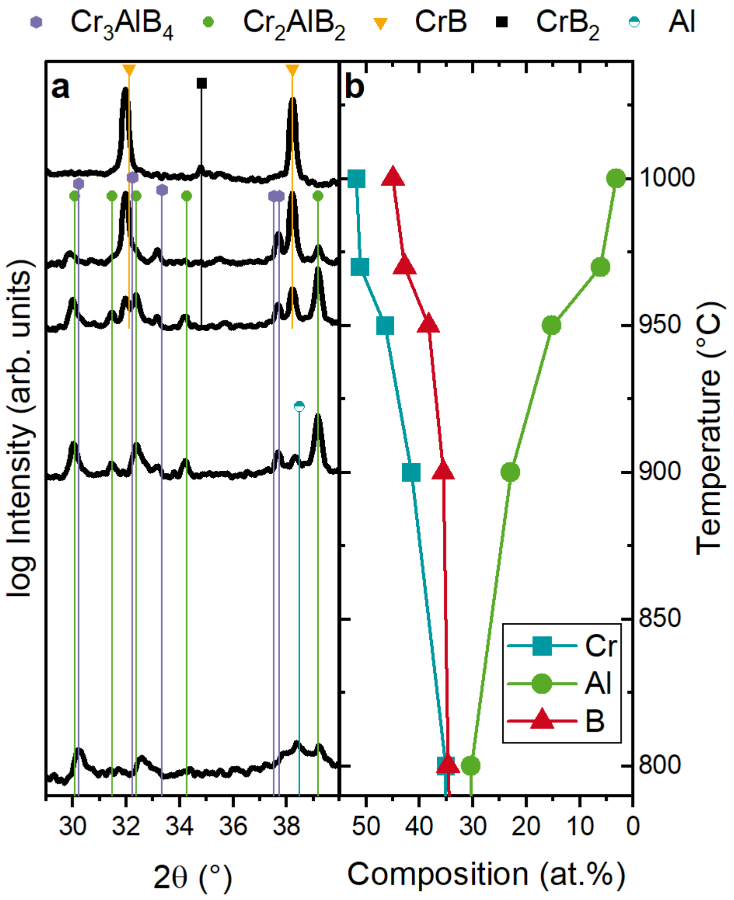

Figure 21. X-ray diffractogram of samples annealed to the indicated temperatures (a) along with chemical composition determined by ERDA (b), showing depletion of Al and concomitant formation of CrB and CrB_2.

Between 800 and 900 °C, both, the decrease in Al concentration from 30 at.% to 23 at.%, measured by ERDA, shown in Figure 21b, and the decrease in diffracted intensity of the Al phase, shown in Figure 21a, are consistent with Al evaporation. In the same figure, the MAB phase related diffraction signals can be seen to increase in intensity. Moreover, the EDX mappings displayed in Figure 23 reveal regions of Al segregation for samples annealed at 800 and 900 °C and HRSTEM micrographs show large crystalline MAB phase regions (Figure 22b). The evaporation of Al from the sample is plausible as the vapor pressure of Al at 800 °C is with 6.5×10^{-7} mbar similar to the base pressure during vacuum annealing at a pressure of $<5 \times 10^{-6}$ mbar [133].

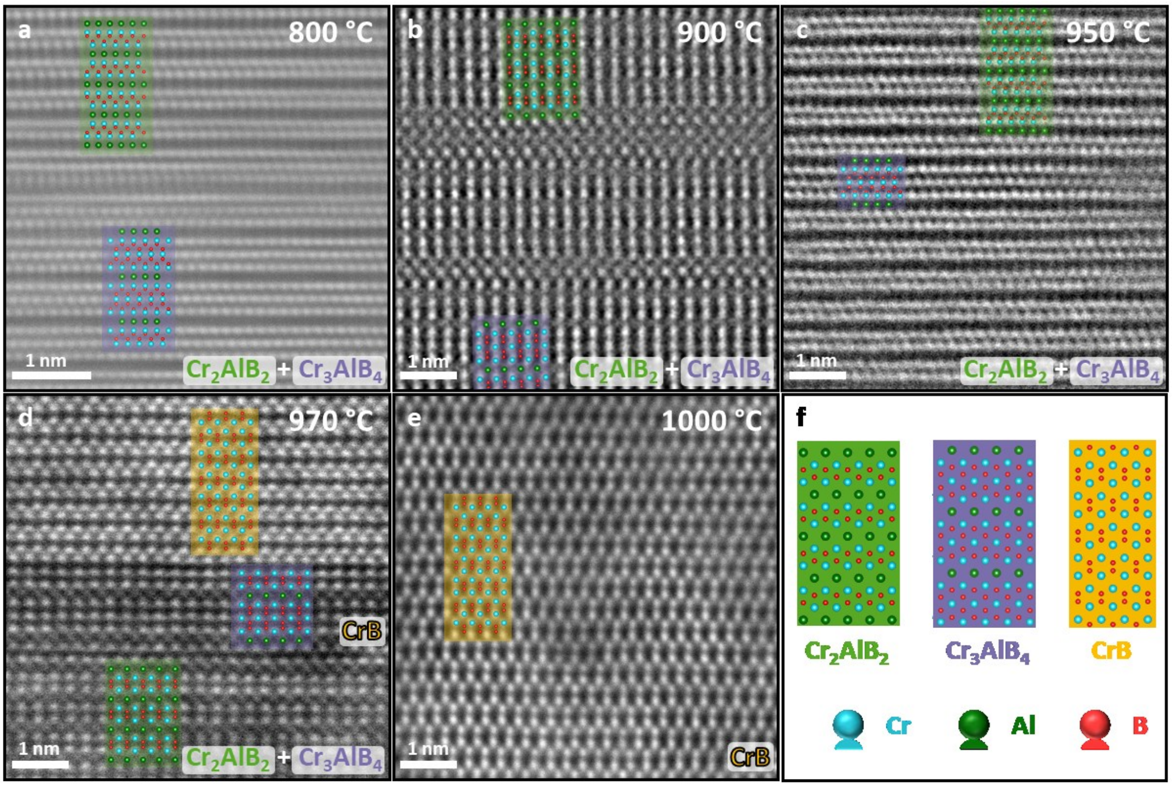

Figure 22. *Ex situ* HRSTEM micrographs of samples annealed to the indicated temperatures (a-e) along with labels for easier distinction of the present phases.

A second distinct chemical and structural change, observed between 900 and 950 °C, is caused by an accelerated loss of Al from 23 to 15 at.%, see Figure 21b, and results in decreased diffraction signal intensities of the MAB phases and the concomitant increase in diffracted intensity, indicating the formation of CrB and CrB_2, see Figure 21a. Moreover, in HRSTEM, the phase formation of CrB is detected at 950 °C (supplementary material Figure S 22) in addition to the MAB phases (Figure 22c). Density functional theory calculations (supplementary material Figure S 21) predict the stability of Cr_2AlB_2 up to a temperature of 927 °C, while Cr_3AlB_4 is only slightly energetically favored, the energetic difference being within the numerical accuracy of DFT. Thus, the simultaneous decomposition of MAB phases by deintercalation of Al from the structure and subsequent formation of CrB, as observed experimentally, is predicted. The determined chemical change caused by MAB phase decomposition and subsequent Al depletion can be explained by the bonding state within the MAB phases:

While the covalent/ionic bonds between Cr and B are strong in comparison, the metallic bonds between Cr and Al render Al to be the most weakly bound species [153], therefore leading to its selective removal and the formation of binary borides.

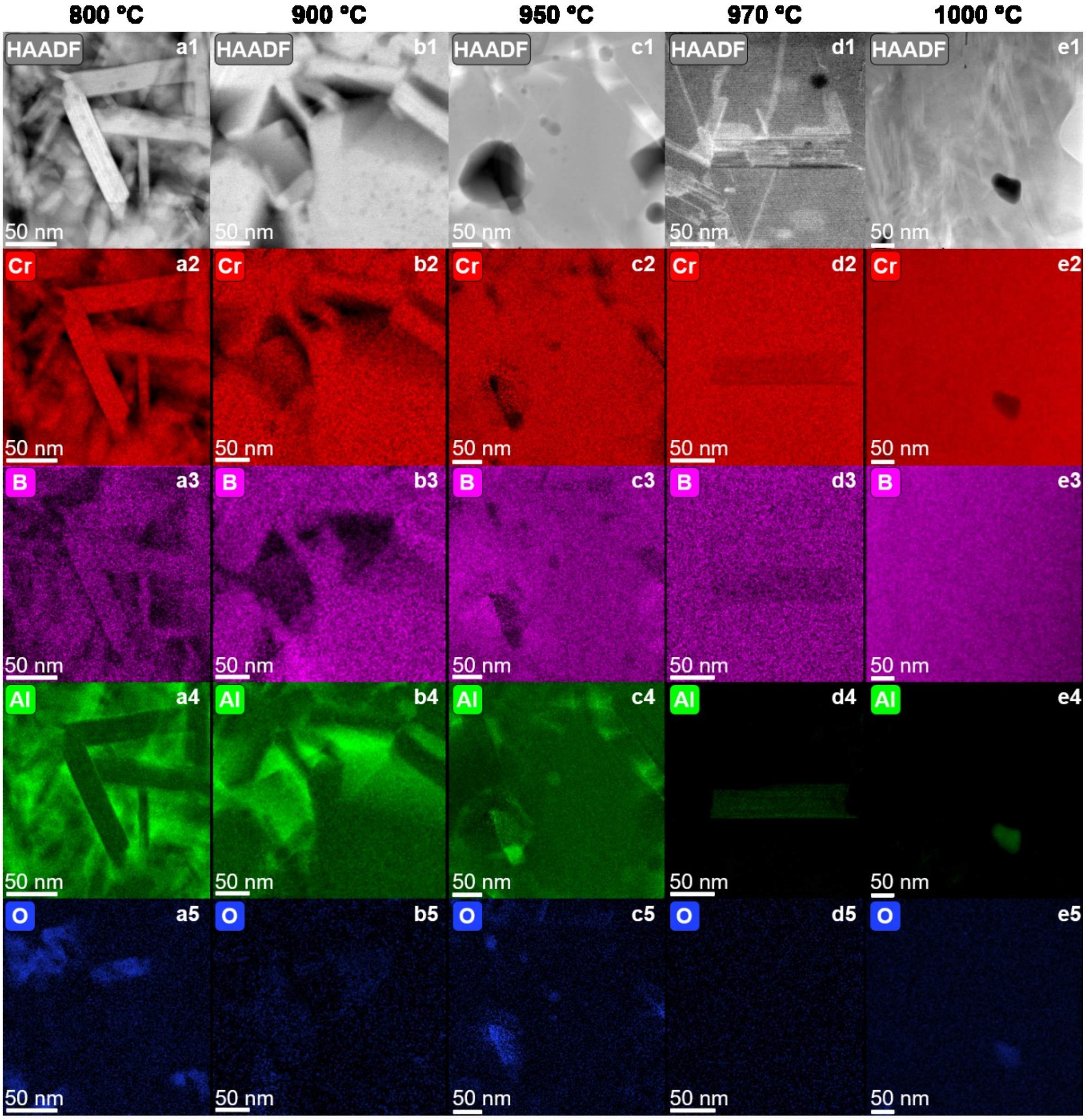

Figure 23. HAADF images and corresponding EDX elemental maps of samples annealed to the indicated temperatures (a-e) showing the distribution of elements after annealing.

Between 950 and 970 °C, the decrease of the Al content from 15 to 6 at.% continues, see Figure 21b, while the increase in CrB and CrB_2 XRD peak intensities indicates an increase in phase fraction thereof (Figure 21a). Moreover, this evolution is consistent with the HRSTEM images shown in Figure 22d, indicating the collapse of the ternary

MAB phases as well as the formation of CrB and CrB_2 crystallites, which are observed to coalesce and grow as the temperature is increased from 950 to 970 °C. This notion is further supported by a HRSTEM video, recorded during an *in situ* annealing experiment between 900-917 °C, showing the deintercalation of Al and the subsequent collapse of the MAB phase grains (supplementary material Figure S 23) as well as by corresponding HRSTEM images showing small CrB and CrB_2 grains at 930 °C, which significantly coarsen after annealing to 1000 °C (Figure 24). Moreover, upon comparison of the EDX maps of samples annealed to 900 °C (Figure 23b) and 1000 °C (Figure 23e and Figure 24 d-g), it is evident that Al has deintercalated from the MAB phase grains causing the formation of CrB and CrB_2.

After annealing to 1000 °C, structural analysis by XRD (Figure 21a) and HRSTEM (Figure 22e) indicate the presence of CrB and CrB_2 phases as well as a small fraction of MAB phases (supplementary material Figure S 24). The remaining Al concentration is 3 at.%, see Figure 21b and Figure 23e.

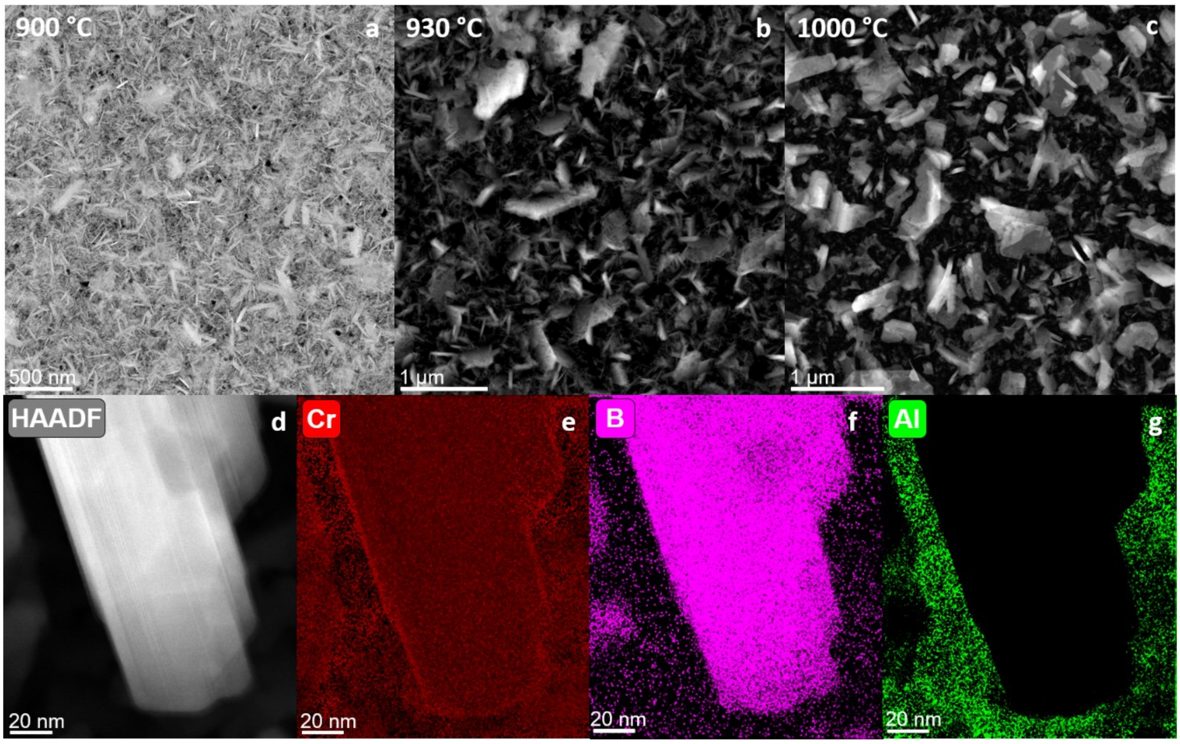

Figure 24. *In situ* STEM micrographs recorded during annealing at 900 °C (a), 930 °C (b), and 1000 °C (c). HAADF micrographs along with EDX elemental map of a grain after annealing at 1000 °C (d-g).

It has been shown that annealing of $Cr_{0.34}Al_{0.31}B_{0.35}$ coatings, containing a mixture of Cr_2AlB_2 and Cr_3AlB_4 MAB phases as well as excess Al (Figure 25a), triggers two changes: First, between 800 and 900 °C, evaporation of Al is observed, leading to a decrease in Al concentration, see Figure 25b. Also, MAB phase grains coarsen, as witnessed by the corresponding increase in diffracted intensity, see Figure 1a. These changes, revealed by employing compositional and structural probes, coincide with an increase in the temperature-dependent resistance signal (Figure 25f).

Second, between 900 °C and 950 °C, decomposition of the MAB phases and subsequent formation of CrB and CrB_2 is detected, see Figure 25c. This deintercalation of Al could also lead to an increase in point defect concentration, that function as electron scattering centers and thereby increase the measured resistance, similar to what was observed for TiC [165] and structurally similar MAX phases [166]. These changes coincide with a significant increase in the slope of the temperature-dependent resistance, see Figure 25f, and hence, the temperature-dependent resistance was demonstrated to track all the chemical and physical changes discussed so far. The observed increase in resistance by 100 % provides a reliable reference point for failure of the coating in the case of application.

When the temperature is increased from 950 to 970 °C, the Al deintercalation from the MAB phases continues until the collapse thereof and concurrent formation of CrB and CrB_2 is observed, see Figure 25d. After annealing at 1000 °C, primarily CrB and CrB_2 remain in the sample, see Figure 25e, and the decomposition of the MAB phases is mostly completed. This concurs with the *in situ* measured temperature-dependent resistance signal showing a decrease after 950 °C (Figure 25f), which is caused by the initial grain growth of newly formed binary borides, reducing the resistance since fewer grain boundaries, acting as obstacles for charge carrier movement, are present. This is in excellent agreement with an observed decrease caused by grain growth in the structurally similar MAX phase Cr_2AlC [37]. Grain growth reduces the number of grain boundaries in the sample and, thus, the resistance. Hence, temperature-dependent resistance data was shown to track the microstructural evolution associated with the decomposition of MAB phases.

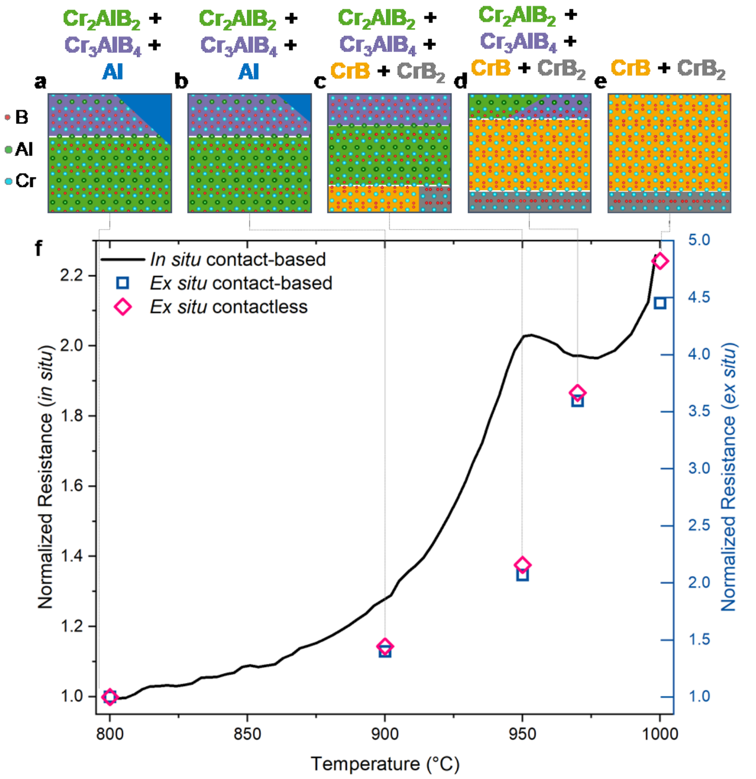

Figure 25. Schematic illustration of phases formed during annealing (a-e) along with *in situ* measured normalized electrical resistance (black curve) and *ex situ* contactless (pink diamonds) as well as contact-based (blue squares) normalized electrical resistance measured at room temperature and, adjusted with the thermal coefficient of resistance (TCR) plotted as a function of temperature (f). TCR and measured resistance values are given in supplementary material Figure S 25.

Furthermore, the increase in resistance due to the decomposition of the MAB phase is supported by the available literature data on electrical resistivities measured at room temperature: While there are no reports of resistivities for the Cr_2AlB_2 MAB phase, MoAlB was measured to exhibit 0.67 µΩm as single crystals [152], with the values decreasing down to 0.23 µΩm upon the addition of Cr [152], indicating that a purely Cr-containing MAB phase might exhibit even lower resistivities. The binary borides CrB and CrB_2 are reported to exhibit resistivities in the region of 0.32 – 0.78 µΩm and 0.30 – 0.99 µΩm [167-170], respectively, thus supporting the notion of an expected increase in resistance upon MAB phase decomposition. The increase in resistance between 970 °C to 1000 °C can be rationalized by the electrical behavior of the newly formed binary chromium borides, since both CrB and CrB_2 were reported to exhibit a positive thermal coefficient of resistance (TCR) [169, 170], and the deintercalation of Al from the remaining MAB phases in combination with the corresponding increase in point defect concentration, explaining the increase in resistance with increasing temperature.

The difference between *in situ* contact-based and *ex situ* contactless resistance measurements is likely caused by the longer exposure to high temperatures of the *ex situ* samples: Since they are subjected to higher temperature during heating and cooling periods, as opposed to the *in situ* samples, which are only subjected to high temperature during the heating period, the reactions observed will be continued during the cooling regime, causing the measured resistances after annealing to be higher for the *ex situ* samples. Since there was no indication of oxidation of the samples, the contact-based method is expected to measure a similar thickness as the contactless method. This notion is supported by the fact that the *ex situ* measured contact-based resistance is in very good agreement with the contactless measurement with a maximum difference of 11%.

Contact-based measurements require physical connections between the coating and readout, limiting their application to stationary components. Contactless measurements, however, overcome this drawback and continuous or periodic contactless tracking of resistance will allow for the monitoring of materials health relevant data in moving components, enabling a more sustainable materials consumption by extending the individual component lifetime.

6.3 Conclusions

Proof of concept for tracking the decomposition of $Cr_{0.34}Al_{0.31}B_{0.35}$ coatings at elevated temperatures was demonstrated by contact-based as well as contactless electrical resistance measurements supported by XRD, ERDA, EDX, and HRSTEM data. The increase in resistance measured between 800 and 900 °C was attributed to Al depletion based on XRD, ERDA, and EDX data. The subsequent resistance increase was explained by the deintercalation of Al from the Cr_2AlB_2 and Cr_3AlB_4 MAB phases, resulting in decomposition thereof and concomitant formation of CrB and CrB_2, consistent with temperature-dependent Gibbs energies of formation obtained from DFT calculations. We envision that the proof of concept for contactless tracking of decomposition in extreme environments presented here serves as inspiration for the integration of this metrology into moving components, enabling more sustainable resource usage as lifetime assessments based on safety factors can be replaced by real-time individual components health data.

6.4 Experimental Details

Cr-Al-B films were synthesized in a high vacuum deposition system ($p_{Base} < 9 \times 10^{-7}$ mbar) without intentional heating by direct current magnetron sputtering (DCMS) using a 2” Cr : Al : B 1 : 1 : 1 target (Plansee Composite Materials GmbH, Lechbruck am See, Germany). The ternary target was operated at a constant power of 120 °W facing the single-crystalline 10 x 10 mm^2 Al_2O_3 (0001) substrates, which were kept at a floating potential. The 60 min deposition time and argon pressure of 0.3 Pa led to a film thickness of ≈ 0.8 µm.

The Van-der-Pauw method [51, 52] was used to measure contact-based electrical resistance, with the *in situ* measurement setup being described in detail elsewhere [18, 37]. A constant heating and cooling rate of 10 K min^{-1} was applied and the base pressure of the vacuum furnace was below 5×10^{-6} mbar.

An EddyCus TF lab 2020SR (SURAGUS GmbH, Dresden, Germany) was used for contactless resistance measurements utilizing eddy currents at a measuring gap of 10 mm. Self-referencing was carried out before every measurement. Two measurements were averaged for each sample to obtain the sheet resistance, whereby the whole area of the sample of 10 x 10 mm was measured. The largest relative deviation between the two measurements was 0.8 %.

Phase formation was analyzed using a Panalytical Empyrean MRD diffractometer (Malvern Panalytical, Almelo, Netherlands) for Bragg-Brentano X-ray diffraction (XRD) equipped with a Cu-Kα source and operated at a current of 40 mA and a voltage of 40 kV. Scans were recorded with a −5° omega offset scan, a step size of 0.026° and a measurement time of 100 s/step. Powder diffraction files (PDF) of Cr_2AlB_2 (01-084-8899), Cr_3AlB_4 (01-084-8900), Al (00-04-0787), CrB (01-089-3587), and CrB_2 (01-084-8447) were used for phase identification.

Depth profiling of the chemical composition was carried out by time-of-flight elastic recoil detection analysis (ToF-ERDA) at the Tandem Accelerator Laboratory of Uppsala University [121]. 36 MeV $^{127}I^{8+}$ ions were used and the incidence and exit angle of primary beam and detected recoils was 22.5° with respect to the film surface, while the angle between the primary beam and the detector telescope was 45°. Thin carbon foils were used for time-of-flight measurements [122] and a segmented gas detector used for energy measurements [123]. Depth profiles were obtained from time-energy coincidence spectra with the CONTES software [160]. Average concentrations were extracted, excluding the oxygen-rich surface-near region. A maximum total uncertainty of 5 % of the determined value is assumed for B and aliquot fractions thereof for the metals Cr and Al.

A Helios 5 Hydra UX dual-beam microscope (Thermo Fisher Scientific, Waltham, USA) was used to fabricate thin lamellae (< 100 nm) by a standard lift-out procedure onto an omniprobe lift-out grid by focused ion beam (FIB). Subsequently, a Titan Themis 200

G3 equipped with a SuperX EDX detector (Thermo Fisher Scientific, Waltham, USA), operated at an acceleration voltage of 200 kV, was employed to analyze the lamellae by high-resolution scanning transmission electron microscopy (HRSTEM). Furthermore, Wildfire nano-chips (DENS Solutions, Delft, Netherlands), directly deposited with < 50 nm of Cr-Al-B, were heated at a constant heating rate of 10 Kmin^{-1} for *in situ* HRSTEM analysis. For imaging, the annealing was interrupted by quenching at specific temperatures for further investigation of critical events.

7 Conclusion

Boride coatings have been shown to possess extraordinary properties for extreme environment conditions potentially enabling their usage in a sustainable and more efficient industry. While diborides, particularly $TiAlB_2$, show extraordinary oxidation resistance, CrAlB can be used as self-reporting materials to reduce materials consumption.

The oxidation resistance of $Ti_{0.12}Al_{0.21}B_{0.67}$ is defined by the lower activation energy of diffusion of Al atoms in comparison to Ti, based on DFT envelope calculations, leading to a preferential diffusion of Al and consequently to the formation of a passivating Al-rich and B-containing oxide layer upon oxidation. SAED and TEM analysis reveal the formation of a passivating oxide layer that is amorphous at oxidation temperatures up to 800 °C after 8 h and consists of nanocrystalline $Al_5(BO_3)O_6$ after 8 h at 900 °C. At this temperature, in the bulk of the film, Ti diffusion is initiated as well enabling spinodal decomposition in Al- and Ti-rich diboride regions. This is not only true for oxidation conditions, but also takes place upon annealing in vacuum at 1000 °C. Hereby, $TiAlB_2$ spinodally decomposes to form TiB_2 and AlB_2 regions. While the TiB_2 regions are not significantly altered upon longer holding times, AlB_2 decomposes into liquid Al and AlB_{12}, which was shown *ex situ* by SAED and EDX analysis as well as by *in situ* STEM imaging. Therefore, while the oxidation resistance of $Ti_{0.12}Al_{0.21}B_{0.67}$ up to 900 °C is due to the preferential diffusion of Al superior to e.g. TiAlN coatings with a similar Al-content, its thermal stability limits its application to 1000°C.

Contactless resistivity measurements were employed on amorphous self-reporting CrAlB thin films to identify the health status of the material up to 1000 °C. The contactless and contact-based resistivity data were verified and analyzed with the help of *ex situ* and *in situ* STEM and SAED as well as ERDA, XRD and DSC. Three separate phase transitions including the formation of Cr_2AlB_2 and Cr_3AlB_4 could be identified *in situ* for the contact-based method with a maximum deviation of 4 % for the contactless measurements in comparison to the contact-based resistivity measurements. In addition to the formation of the crystalline Cr_2AlB_2 and Cr_3AlB_4 phases, accelerated grain growth could be tracked *in situ* and contactless as well.

Additionally, the decomposition of the CrAlB phases into CrB and CrB_2 by deintercalation of the Al layer could be tracked *in situ* by an increase in resistivity and verified with HRSTEM and SAED data. With a maximum deviation of 11 % for the contactless resistivity measurement, the decomposition could also be tracked contactless. The decomposition process is characterized by three steps. First, excess Al evaporates in vacuum at temperatures above 800 °C, which is present due to the presence of Cr_2AlB_2 and Cr_3AlB_4 phases in a 1:1:1 Cr:Al:B stoichiometry sample. In a second step, starting at 900 °C, the MAB phases start to decompose into the binary borides resulting in a collapse of the MAB phases at 950 – 970 °C and the simultaneous grain growth of formed CrB and CrB_2.

The proof of concept for contactless resistivity measurements to track structural, chemical and phase changes in CrAlB coatings, demonstrates its potential in tracking the health status of materials and components. Due to its simple design and short measurement times, it can be employed for extreme environment and high speed applications, significantly extending their lifetimes.

8 Future Work

While $Ti_{0.12}Al_{0.21}B_{0.67}$ already shows outstanding oxidation properties as well as thermal stability up to 900 °C, above 1000 °C, the decomposition of the ternary diboride into TiB_2 and AlB_2 limits their application at these temperatures due to the lower thermal stability and therefore decomposition of AlB_2. In order to increase the application temperatures without losing the superior oxidation resistance achieved by the addition of Al, the spinodal decomposition of the ternary diboride needs to be delayed. While Al is needed as part of the ternary boride due to its role in increasing the oxidation resistance, Ti could be replaced by an alternative transition metal, e.g. Hf or Ta, in order to change the decomposition behavior. As spinodal decomposition is only taking place once the Ti diffusion is initiated, a DFT screening could be conducted to identify the transition metal with the highest activation energy for diffusion as part of a ternary $TMAlB_2$. A second approach would incorporate the reduction of the Al content, potentially decreasing the impact of decomposition. As decreasing the Al content < 15 at.% leads to a non-passivating oxide layer on top and therefore to a worse oxidation resistance [15], the oxidation resistance needs to be enhanced with a different approach. Therefore, either a multi-layer approach with high and low Al contents could prove useful or an artificial oxide layer on top of a coating with a low Al content might increase the oxidation resistance.

The proof of concept for self-reporting MAB coatings by contactless resistivity measurements showed its potential in the tracking of materials health status. In order to increase its usability for application in extreme environments, the design and construction of a high temperature eddy current measurement device would enable more complex and application-oriented tests. Additionally, to prove the usability of the contactless resistivity method, a wider range of simple and complex materials need to be tested. Thereby, a calibration protocol should be implemented, standardizing the analysis of the approach. The most promising analytical methods to calibrate the resistivity data with regard to time effort and cost as well as accuracy include XRD and DSC measurements for simpler materials, while TEM and SAED should only be necessary for more complex material systems. In summary, with the above mentioned additional processes, a relatively cheap, fast, standardized and simple method could be developed in order to track materials health in extreme environments for different material systems.

9 References

1. Mayrhofer, P.H. *Thermal stability and self-arrangement of nanocrystalline hard coatings*. in *Nanostructured Thin Films and Nanodispersion Strengthened Coatings*. 2004. Springer.
2. Mayrhofer, P., et al., *Self-organized nanocolumnar structure in superhard TiB 2 thin films.* Applied Physics Letters, 2005. **86**(13): p. 131909.
3. Kota, S., et al., *Isothermal and cyclic oxidation of MoAlB in air from 1100° C to 1400° C.* Journal of The Electrochemical Society, 2017. **164**(13): p. C930.
4. Xu, L., et al., *Synthesis, microstructure and properties of MoAlB ceramics.* Ceramics International, 2018. **44**(11): p. 13396-13401.
5. Kota, S., M. Sokol, and M.W. Barsoum, *A progress report on the MAB phases: atomically laminated, ternary transition metal borides.* International Materials Reviews, 2020. **65**(4): p. 226-255.
6. Zou, B., et al., *Mechanical properties and microstructure of TiB2–TiC composite ceramic cutting tool material.* International Journal of Refractory Metals and Hard Materials, 2012. **35**: p. 1-9.
7. Moghanlou, F.S., et al., *A numerical approach to the heat transfer in monolithic and SiC reinforced HfB2, ZrB2 and TiB2 ceramic cutting tools.* Ceramics International, 2019. **45**(13): p. 15892-15897.
8. Grigoriev, S., et al., *The Study of Radius End Mills with TiB2 Coating When Milling a Nickel Alloy.* Materials, 2023. **16**(6): p. 2535.
9. Tampieri, A. and A. Bellosi, *Oxidation of monolithic TiB2 and of Al2O3-TiB2 composite.* Journal of materials science, 1993. **28**(3): p. 649-653.
10. Bakhit, B., et al., *Improving the high-temperature oxidation resistance of TiB2 thin films by alloying with Al.* Acta Materialia, 2020. **196**: p. 677-689.
11. Voitovich, V., V. Lavrenko, and V. Adejev, *High-temperature oxidation of titanium diboride of different purity.* Oxidation of metals, 1994. **42**(1): p. 145-161.
12. Navidi Kashani, A.H., et al., *Synthesis and oxidation behavior of Ti0. 35Al0. 65By (y= 1.7–2.4) coatings.* Surface and Coatings Technology, 2022: p. 128190.
13. Thörnberg, J., et al., *Oxidation resistance and mechanical properties of sputter-deposited Ti0. 9Al0. 1B2-y thin films.* Surface and Coatings Technology, 2022: p. 128187.
14. Mollica, S., et al., *Effect of aluminium ion implantation on the oxidation resistance of DC magnetron sputter-deposited TiB2 thin films.* Surface and Coatings Technology, 2004. **177**: p. 185-197.
15. Navidi Kashani, A.H., et al., *Morphology, mechanical properties, and oxidation behavior of stoichiometric Ti0.33-xAlxB0.67 coatings (x = 0.04, 0.15, 0.21, and 0.28).* Acta Materialia, 2024. **270**: p. 119829.
16. Burdekin, F.M., *General principles of the use of safety factors in design and assessment.* Engineering Failure Analysis, 2007. **14**(3): p. 420-433.
17. Roos, E., et al., *Probabilistic safety assessment of components.* International Journal of Pressure Vessels and Piping, 2011. **88**(1): p. 19-25.
18. Stelzer, B., M. Momma, and J.M. Schneider, *Autonomously Self-Reporting Hard Coatings: Tracking the Temporal Oxidation Behavior of TiN by In Situ Sheet Resistance Measurements.* Advanced Functional Materials, 2020: p. 2000146.

19. Fang, L., et al., *On the potential of Er-doped AlN film as luminescence sensing layer for multilayer Al/AlN coating health monitoring.* Journal of Alloys and Compounds, 2017. **727**: p. 735-743.
20. Xiao, J., et al., *Glow Stick-Inspired Multilayered Composites with Damage Self-Reporting and Self-Healing Properties for Aquatic Environments.* Advanced Engineering Materials, 2023. **25**(16): p. 2300331.
21. Rifaie-Graham, O., et al., *Self-Reporting Fiber-Reinforced Composites That Mimic the Ability of Biological Materials to Sense and Report Damage.* Advanced Materials, 2018. **30**(19): p. 1705483.
22. Gao, L., et al., *Sensing of Damage Mechanisms in Fiber-Reinforced Composites under Cyclic Loading using Carbon Nanotubes.* Advanced Functional Materials, 2009. **19**(1): p. 123-130.
23. Gao, S.-l., et al., *Glass Fibers with Carbon Nanotube Networks as Multifunctional Sensors.* Advanced Functional Materials, 2010. **20**(12): p. 1885-1893.
24. Zhang, J., et al., *Single MWNT-Glass Fiber as Strain Sensor and Switch.* Advanced Materials, 2011. **23**(30): p. 3392-3397.
25. Markvicka, E.J., et al., *Soft Electronic Skin for Multi-Site Damage Detection and Localization.* Advanced Functional Materials, 2019. **29**(29): p. 1900160.
26. Picot, O.T., et al., *Using graphene networks to build bioinspired self-monitoring ceramics.* Nature Communications, 2017. **8**(1): p. 14425.
27. Davis, D.A., et al., *Force-induced activation of covalent bonds in mechanoresponsive polymeric materials.* Nature, 2009. **459**(7243): p. 68-72.
28. Bruns, N., et al., *Mechanical Nanosensor Based on FRET within a Thermosome: Damage-Reporting Polymeric Materials.* Angewandte Chemie International Edition, 2009. **48**(31): p. 5666-5669.
29. Wang, Q., et al., *Cephalopod-inspired design of electro-mechano-chemically responsive elastomers for on-demand fluorescent patterning.* Nature Communications, 2014. **5**(1): p. 4899.
30. Makyła, K., et al., *Fluorescent Protein Senses and Reports Mechanical Damage in Glass-Fiber-Reinforced Polymer Composites.* Advanced Materials, 2013. **25**(19): p. 2701-2706.
31. Tolpygo, V.K., D.R. Clarke, and K.S. Murphy, *Evaluation of interface degradation during cyclic oxidation of EB-PVD thermal barrier coatings and correlation with TGO luminescence.* Surface and Coatings Technology, 2004. **188-189**: p. 62-70.
32. Kim, Y.-K., et al., *Self-reporting and self-regulating liquid crystals.* Nature, 2018. **557**(7706): p. 539-544.
33. Hu, X., et al., *Construction of Self-Reporting Specific Chemical Sensors with High Sensitivity.* Advanced Materials, 2007. **19**(24): p. 4327-4332.
34. Liu, C., et al., *Design of smart protective coatings with autonomous self-healing and early corrosion reporting properties.* Corrosion Science, 2021. **184**: p. 109355.
35. Wang, J.-P., et al., *Smart-Sensing Polymer Coatings with Autonomously Reporting Corrosion Dynamics of Self-Healing Systems.* Advanced Materials Interfaces, 2019. **6**(10): p. 1900055.
36. Wang, J.-P., et al., *Adaptive Polymeric Coatings with Self-Reporting and Self-Healing Dual Functions from Porous Core–Shell Nanostructures.* Macromolecular Materials and Engineering, 2018. **303**(4): p. 1700616.
37. Stelzer, B., et al., *Remote Tracking of Phase Changes in Cr2AlC Thin Films by In-situ Resistivity Measurements.* Scientific Reports, 2019. **9**: p. 7.

38. Hans, M., et al., *Probing the onset of wurtzite phase formation in (V, Al) N thin films by transmission electron microscopy and atom probe tomography.* Surface and Coatings Technology, 2022: p. 128235.
39. Nayak, G.K., et al., *On correlations between local chemistry, distortions and kinetics in high entropy nitrides: An ab initio study.* Acta Materialia, 2023: p. 118951.
40. Kelly, P.J. and R.D. Arnell, *Magnetron sputtering: a review of recent developments and applications.* Vacuum, 2000. **56**(3): p. 159-172.
41. Janarthanan, B., et al., *Basic deposition methods of thin films**.* Journal of Molecular Structure, 2021. **1241**: p. 130606.
42. Musil, J., et al., *Reactive magnetron sputtering of thin films: present status and trends.* Thin solid films, 2005. **475**(1-2): p. 208-218.
43. Swann, S., *Magnetron sputtering.* Physics in technology, 1988. **19**(2): p. 67.
44. Gudmundsson, J.T., *Physics and technology of magnetron sputtering discharges.* Plasma Sources Science and Technology, 2020. **29**(11): p. 113001.
45. Musil, J. and J. Vlček, *Magnetron sputtering of alloy and alloy-based films.* Thin solid films, 1999. **343**: p. 47-50.
46. Bräuer, G., et al., *Magnetron sputtering – Milestones of 30 years.* Vacuum, 2010. **84**(12): p. 1354-1359.
47. Birkholz, M., *Thin film analysis by X-ray scattering*. 2006: John Wiley & Sons.
48. Goldstein, J.I., et al., *Scanning electron microscopy and X-ray microanalysis*. 2017: springer.
49. Schneider, R., *Energy-Dispersive X-Ray Spectroscopy (EDXS).* Surface and Thin Film Analysis: A Compendium of Principles, Instrumentation, and Applications, 2011: p. 293-310.
50. Harwood, R. and E. Smith, *Testing of natural textile fibres*, in *Handbook of natural fibres*. 2020, Elsevier. p. 535-576.
51. Pauw, L.J.V.d., *A method of measuring specific resistivity and Hall coefficient on lamellae of arbitrary shape.* Philips Technical Review, 1958. **20**: p. 220-224.
52. Pauw, L.J.V.d., *A method of measuring specific resistivity and Hall effect of discs of arbitrary shape.* Philips Research Reports, 1958. **13**: p. 1-9.
53. Oliveira, F., et al., *Simple analytical method for determining electrical resistivity and sheet resistance using the van der Pauw procedure.* Scientific reports, 2020. **10**(1): p. 16379.
54. Sophian, A., et al., *Electromagnetic and eddy current NDT: a review.* Insight, 2001. **43**(5): p. 302-306.
55. Tian, G.Y., Z.X. Zhao, and R.W. Baines, *The research of inhomogeneity in eddy current sensors.* Sensors and Actuators A: Physical, 1998. **69**(2): p. 148-151.
56. Williams, D.B., et al., *The transmission electron microscope*. 2009: Springer.
57. Miller, M.K., et al., *Introduction to atom-probe tomography.* Atom-Probe Tomography: The Local Electrode Atom Probe, 2014: p. 1-49.
58. Gault, B., et al., *Atom probe tomography.* Nature Reviews Methods Primers, 2021. **1**(1): p. 51.
59. Hans, M., et al., *Is it meaningful to quantify vacancy concentrations of nanolamellar (Ti,Al)N thin films based on laser-assisted atom probe data?* Surface and Coatings Technology, 2023. **473**: p. 130020.
60. Thompson, K., et al., *In situ site-specific specimen preparation for atom probe tomography.* Ultramicroscopy, 2007. **107**(2): p. 131-139.
61. Adams, F. and C. Barbante, *Chapter 8 - Particle-Based Imaging Techniques*, in *Comprehensive Analytical Chemistry*, F. Adams and C. Barbante, Editors. 2015, Elsevier. p. 315-337.

62. Harrison, N., *An introduction to density functional theory.* Nato Science Series Sub Series III Computer and Systems Sciences, 2003. **187**: p. 45-70.
63. Engel, E., *Density functional theory*. 2011: Springer.
64. Hohenberg, P. and W. Kohn, *Inhomogeneous electron gas.* Physical review, 1964. **136**(3B): p. B864.
65. Music, D., R.W. Geyer, and J.M. Schneider, *Recent progress and new directions in density functional theory based design of hard coatings.* Surface and Coatings Technology, 2016. **286**: p. 178-190.
66. Kohn, W. and L.J. Sham, *Self-consistent equations including exchange and correlation effects.* Physical review, 1965. **140**(4A): p. A1133.
67. Munro, R.G., *Material properties of titanium diboride.* Journal of Research of the National institute of standards and Technology, 2000. **105**(5): p. 709.
68. Berger, M. and S. Hogmark, *Evaluation of TiB2 coatings in sliding contact against aluminium.* Surface and Coatings Technology, 2002. **149**(1): p. 14-20.
69. Dranenko, A., V. Lavrenko, and V. Talash, *Corrosion resistance of nanostructured TiB2 films in 3% NACl solution.* Powder Metallurgy and Metal Ceramics, 2010. **49**(3): p. 174-178.
70. Shaw, M.C. and J. Cookson, *Metal cutting principles*. Vol. 2. 2005: Oxford university press New York.
71. Huang, X., et al., *Hypervelocity impact of TiB2-based composites as front bumpers for space shield applications.* Materials & Design, 2016. **97**: p. 473-482.
72. Gupta, N., et al., *Ballistic Studies on TiB 2-Ti Functionally Graded Armor Ceramics.* Defence Science Journal, 2012. **62**(6).
73. Fahrenholtz, W.G. and G.E. Hilmas, *Ultra-high temperature ceramics: Materials for extreme environments.* Scripta Materialia, 2017. **129**: p. 94-99.
74. Berger, M., M. Larsson, and S. Hogmark, *Evaluation of magnetron-sputtered TiB2 intended for tribological applications.* Surface and Coatings Technology, 2000. **124**(2-3): p. 253-261.
75. Polyakov, M.N., et al., *Microstructure-driven strengthening of TiB2 coatings deposited by pulsed magnetron sputtering.* Surface and Coatings Technology, 2019. **368**: p. 88-96.
76. Padamata, S.K., et al., *Wettable TiB2 cathode for aluminum electrolysis: a review.* Journal of Sustainable Metallurgy, 2022. **8**(2): p. 613-624.
77. Li, J., et al., *Research progress in TiB 2 wettable cathode for aluminum reduction.* Jom, 2008. **60**: p. 32-37.
78. Cooke, A.V. and W.M. Buchta, *Use of TiB2 cathode material: demonstrated energy conservation in VSS cells*, in *Essential Readings in Light Metals: Volume 4 Electrode Technology for Aluminum Production*. 1985, Springer. p. 1153-1163.
79. Xi, L., et al., *High-temperature wetting and interfacial interaction between liquid Al and TiB 2 ceramic.* Journal of Materials Science, 2015. **50**: p. 2682-2690.
80. He, R., et al., *Anti-corrosion and conductivity of titanium diboride coating on metallic bipolar plates.* Corrosion Science, 2020. **170**: p. 108646.
81. Monticelli, C., et al., *The corrosion behaviour of titanium diboride in neutral chloride solution.* Corrosion science, 2001. **43**(5): p. 979-992.
82. Diao, Y. and K. Zhang, *Microstructure and corrosion resistance of TC2 Ti alloy by laser cladding with Ti/TiC/TiB2 powders.* Applied Surface Science, 2015. **352**: p. 163-168.

83. Cai, X., et al., *Unmasking the anomalous rapid oxidation of refractory TiB2 at low temperatures.* Journal of the European Ceramic Society, 2021. **41**(10): p. 5100-5108.
84. Fuger, C., et al., *Revisiting the origins of super-hardness in TiB2+z thin films – Impact of growth conditions and anisotropy.* Surface and Coatings Technology, 2022. **446**: p. 128806.
85. Stüber, M., et al., *Microstructure of Al-containing magnetron sputtered TiB2 thin films.* Thin Solid Films, 2019. **688**: p. 137361.
86. Nedfors, N., et al., *Influence of the Al concentration in Ti-Al-B coatings on microstructure and mechanical properties using combinatorial sputtering from a segmented TiB2/AlB2 target.* Surface and Coatings Technology, 2019. **364**: p. 89-98.
87. Mockuté, A., et al., *Age hardening in (Ti1-xAlx) B2+ Delta thin films.* Scripta Materialia, 2017. **127**: p. 122-126.
88. Thompson, K., et al., *Three-dimensional atom mapping of dopants in Si nanostructures.* Applied Physics Letters, 2005. **87**(5): p. 052108.
89. Wei, S.-H., et al., *Electronic properties of random alloys: Special quasirandom structures.* Physical Review B, 1990. **42**(15): p. 9622.
90. Kresse, G. and J. Furthmüller, *Efficiency of ab-initio total energy calculations for metals and semiconductors using a plane-wave basis set.* Computational materials science, 1996. **6**(1): p. 15-50.
91. Kresse, G. and J. Furthmüller, *Efficient iterative schemes for ab initio total-energy calculations using a plane-wave basis set.* Physical review B, 1996. **54**(16): p. 11169.
92. Perdew, J.P., et al., *Restoring the density-gradient expansion for exchange in solids and surfaces.* Physical review letters, 2008. **100**(13): p. 136406.
93. Blöchl, P.E., *Projector augmented-wave method.* Physical review B, 1994. **50**(24): p. 17953.
94. Monkhorst, H.J. and J.D. Pack, *Special points for Brillouin-zone integrations.* Physical review B, 1976. **13**(12): p. 5188.
95. Methfessel, M. and A. Paxton, *High-precision sampling for Brillouin-zone integration in metals.* Physical Review B, 1989. **40**(6): p. 3616.
96. Sheppard, D., R. Terrell, and G. Henkelman, *Optimization methods for finding minimum energy paths.* The Journal of chemical physics, 2008. **128**(13): p. 134106.
97. Nayak, G.K., M.N. Popov, and D. Holec, *Pressure- and temperature-dependent diffusion from first-principles: A case study of V and Ti in a TiN matrix.* Surface and Coatings Technology, 2021. **422**: p. 127491.
98. Gottstein, G., *Physical foundations of materials science*. Vol. 3. 2004: Springer.
99. Norton, J.T., H. Blumenthal, and S. Sindeband, *Structure of diborides of titanium, zirconium, columbium, tantalum and vanadium.* JOM, 1949. **1**(10): p. 749-751.
100. Sokolova, E.V., et al. *Crystal structure of synthetic ortho-3-borate, Al_5(BO_3)O_6*. in *Doklady Akademii Nauk*. 1978. Russian Academy of Sciences.
101. Felten, E.J., *The preparation of aluminum diboride, AlB21.* Journal of the American Chemical Society, 1956. **78**(23): p. 5977-5978.
102. Zhou, R.-S. and R.L. Snyder, *Structures and transformation mechanisms of the η, γ and θ transition aluminas.* Acta Crystallographica Section B: Structural Science, 1991. **47**(5): p. 617-630.

103. Ollivier, B., et al., *Crystal structure of κ-alumina: an X-ray powder diffraction, TEM and NMR study.* Journal of Materials Chemistry, 1997. **7**(6): p. 1049-1056.

104. Navidi Kashani, A.H., et al., *Temporally-resolved decomposition of Ti0. 12Al0. 21B0. 67 thin films at 1000° C.* Surface and Coatings Technology, 2024: p. 131026.

105. Holleck, H., *Material selection for hard coatings.* Journal of Vacuum Science & Technology A, 1986. **4**(6): p. 2661-2669.

106. Thörnberg, J., et al., *Microstructure and materials properties of understoichiometric TiB_x thin films grown by HiPIMS.* Surface and Coatings Technology, 2020. **404**: p. 126537.

107. Berger, M., et al., *Low stress TiB_2 coatings with improved tribological properties.* Thin Solid Films, 2001. **401**(1): p. 179-186.

108. Milman, V. and M.C. Warren, *Elastic properties of TiB_2 and MgB_2.* Journal of Physics: Condensed Matter, 2001. **13**(24): p. 5585.

109. Panda, K.B. and K.S. Ravi Chandran, *Determination of elastic constants of titanium diboride (TiB_2) from first principles using FLAPW implementation of the density functional theory.* Computational Materials Science, 2006. **35**(2): p. 134-150.

110. Shein, I.R. and A.L. Ivanovskii, *Elastic properties of mono- and polycrystalline hexagonal AlB_2-like diborides of s, p and d metals from first-principles calculations.* Journal of Physics: Condensed Matter, 2008. **20**(41): p. 415218.

111. Berger, M. and S. Hogmark, *Tribological properties of selected PVD coatings when slid against ductile materials.* Wear, 2002. **252**(7): p. 557-565.

112. Korobov, I.I., et al., *Corrosion resistance of nanostructured films of titanium diboride in mineral acid solutions.* Protection of Metals and Physical Chemistry of Surfaces, 2016. **52**(4): p. 618-621.

113. Shappirio, J., et al., *TiB_2 and ZrB_2 diffusion barriers in GaAs Ohmic contact technology.* Journal of Vacuum Science & Technology A, 1985. **3**(6): p. 2255-2258.

114. Sade, G. and J. Pelleg, *Co-sputtered TiB_2 as a diffusion barrier for advanced microelectronics with Cu metallization.* Applied Surface Science, 1995. **91**(1): p. 263-268.

115. Chen, J.S. and J.L. Wang, *Diffusion Barrier Properties of Sputtered TiB_2 Between Cu and Si.* Journal of The Electrochemical Society, 2000. **147**(5): p. 1940.

116. Wang, J.L. and J.S. Chen, *TiB_2 as a Diffusion Barrier for Cu/<Si> Metallization.* MRS Online Proceedings Library, 1999. **563**(1): p. 33-38.

117. Alling, B., et al., *A theoretical investigation of mixing thermodynamics, age-hardening potential, and electronic structure of ternary $M^1{}_{1-x}M^2{}_xB_2$ alloys with AlB_2 type structure.* Scientific Reports, 2015. **5**: p. 9888.

118. Becher, H.J., *Über die Darstellung und Beständigkeit von Aluminiumdiborid.* Zeitschrift für anorganische und allgemeine Chemie, 1961. **308**(1-6): p. 13-22.

119. Raghavan, V., *Al-B-Ti (aluminum-boron-titanium).* Journal of phase equilibria and diffusion, 2009. **30**(6): p. 610-613.

120. Mockute, A., et al., *Synthesis and characterization of $(Ti_{1-x}Al_x)B_{2+\Delta}$ thin films from combinatorial magnetron sputtering.* Thin Solid Films, 2019. **669**: p. 181-187.

121. Ström, P. and D. Primetzhofer, *Ion beam tools for nondestructive in-situ and in-operando composition analysis and modification of materials at the Tandem Laboratory in Uppsala.* Journal of Instrumentation, 2022. **17**(04): p. P04011.

122. Zhang, Y., et al., *Detection efficiency of time-of-flight energy elastic recoil detection analysis systems.* Nuclear Instruments and Methods in Physics Research Section B: Beam Interactions with Materials and Atoms, 1999. **149**(4): p. 477-489.
123. Ström, P., et al., *A combined segmented anode gas ionization chamber and time-of-flight detector for heavy ion elastic recoil detection analysis.* Review of Scientific Instruments, 2016. **87**(10): p. 103303.
124. Kottler, C., et al., *A spectrometer for low energy heavy ion ERDA.* Nuclear Instruments and Methods in Physics Research Section B: Beam Interactions with Materials and Atoms, 2006. **248**(1): p. 155-162.
125. Schneider, J.M., et al., *Role of hydrogen for the elastic properties of alumina thin films.* Applied Physics Letters, 2002. **80**(7): p. 1144-1146.
126. Mikula, M., et al., *Thermally-induced structure evolution in ternary Ti1−xYxB2+Δ films.* Scripta Materialia, 2019. **164**: p. 91-95.
127. Greczynski, G., et al., *Venting temperature determines surface chemistry of magnetron sputtered TiN films.* Applied Physics Letters, 2016. **108**(4): p. 041603.
128. *JCPDS International Centre for Diffraction Data, Titanium Diboride (TiB_2) card 00-035-0741.*
129. *JCPDS International Centre for Diffraction Data, Aluminium Diboride (AlB_2) card 00-008-0216.*
130. to Baben, M., et al., *Unprecedented thermal stability of inherently metastable titanium aluminum nitride by point defect engineering.* Materials Research Letters, 2017. **5**(3): p. 158-169.
131. Holzapfel, D.M., et al., *Enhanced thermal stability of (Ti,Al)N coatings by oxygen incorporation.* Acta Materialia, 2021. **218**: p. 117204.
132. *JCPDS International Centre for Diffraction Data, Aluminum dodecaboride (AlB_{12}) card 01-076-1235.*
133. Alcock, C.B., V.P. Itkin, and M.K. Horrigan, *Vapour Pressure Equations for the Metallic Elements: 298–2500K.* Canadian Metallurgical Quarterly, 1984. **23**(3): p. 309-313.
134. Hall, A. and J. Economy, *The $Al_{(L)}$ + $AlB_{12} \leftrightarrow AlB_2$ peritectic transformation and its role in the formation of high aspect ratio AlB2 flakes.* Journal of Phase Equilibria, 2000. **21**(1): p. 63-69.
135. Sirtl, E. and L.M. Woerner, *Preparation and properties of aluminum diboride single crystals.* Journal of Crystal Growth, 1972. **16**(3): p. 215-218.
136. Campbell, C.E. and U.R. Kattner, *A thermodynamic assessment of the Ni-Al-B system.* Journal of Phase Equilibria, 1999. **20**(5): p. 485.
137. Mirković, D., et al., *Experimental study and thermodynamic re-assessment of the Al–B system.* Journal of Alloys and Compounds, 2004. **384**(1-2): p. 168-174.
138. Duschanek, H. and P. Rogl, *The Al-B (aluminum-boron) system.* Journal of Phase Equilibria, 1994. **15**(5): p. 543-552.
139. United-Nations, *The Sustainable Development Goals Report 2023: Special Edition*. 2023: The Sustainable Development Goals Report 2023: Special Edition.
140. Huang, X., et al., *Autonomous indication of electrical degradation in polymers.* Nature Materials, 2023.
141. Crenshaw, B.R. and C. Weder, *Phase Separation of Excimer-Forming Fluorescent Dyes and Amorphous Polymers: A Versatile Mechanism for Sensor Applications.* Advanced Materials, 2005. **17**(12): p. 1471-1476.

142. Mooij, J.H., *Electrical conduction in concentrated disordered transition metal alloys.* physica status solidi (a), 1973. **17**(2): p. 521-530.
143. Mizutani, U., *Electron Transport in Non-Periodic Metallic Systems: Amorphous Alloys and Quasicrystals.* physica status solidi (b), 1993. **176**(1): p. 9-30.
144. Mayrhofer, P.H. and C. Mitterer, *High-temperature properties of nanocomposite TiBxNy and TiBxCy coatings.* Surface and Coatings Technology, 2000. **133-134**: p. 131-137.
145. Mayrhofer, P.H., H. Willmann, and C. Mitterer, *Recrystallization and grain growth of nanocomposite Ti–B–N coatings.* Thin Solid Films, 2003. **440**(1): p. 174-179.
146. Liu, J., et al., *Microstructure Characterization and Thermal Stability of Nanocrystalline Cu Powders Processed via Cryomilling.* MATERIALS TRANSACTIONS, 2012. **53**(4): p. 766-769.
147. Pöllmann, P.J., et al., *Metastable phase formation of (Mo,Cr)2AlB2 MAB phase thin films revealed by theory and experiments.* Materials Research Letters, 2024. **12**(1): p. 58-66.
148. Sahu, R., et al., *Compositional defects in a MoAlB MAB phase thin film grown by high-power pulsed magnetron sputtering.* Nanoscale, 2023. **15**(43): p. 17356-17363.
149. Sahu, R., et al., *Defects in an orthorhombic MoAlB MAB phase thin film grown at moderate synthesis temperature.* Nanoscale, 2022. **14**(7): p. 2578-2585.
150. Sahu, R., et al., *Direct MoB MBene domain formation in magnetron sputtered MoAlB thin films.* Nanoscale, 2021. **13**(43): p. 18077-18083.
151. Buschow, K.H.J., *Phase relations and intermetallic compounds in the systems neodymium-aluminium and gadolinium-aluminium.* Journal of the Less Common Metals, 1965. **9**(6): p. 452-456.
152. Okada, S., et al., *Single Crystal Growth of (MoXCr1−X)AlB and (MoXW1−X)AlB by Metal Al Solutions and Properties of the Crystals.* Journal of Solid State Chemistry, 1997. **133**(1): p. 36-43.
153. Bogdanovski, D., P.J. Pöllmann, and J.M. Schneider, *An ab initio investigation of the temperature-dependent energetic barriers towards CrAlB and (Mo, Cr) AlB formation in a metastable synthesis scenario.* Nanoscale, 2022. **14**(35): p. 12866-12874.
154. Zhou, Y., et al., *Electrical conductive and damage-tolerant nanolaminated MAB phases Cr2AlB2, Cr3AlB4 and Cr4AlB6.* Materials Research Letters, 2017. **5**(6): p. 440-448.
155. Abrikosov, I.A., et al., *Phase stability and elasticity of TiAlN.* Materials, 2011. **4**(9): p. 1599-1618.
156. Martins, B., et al., *Electrical properties and thermistor behavior of TiAlN thin films deposited by combinatorial sputtering.* Surface and Coatings Technology, 2023. **464**: p. 129545.
157. Huon, A., et al., *Effect of chemical pressure on the electronic phase transition in Ca1−xSrxMn7O12 films.* APL Materials, 2017. **5**(9).
158. Limaiem, A. and F. Trochu, *Geometric algorithms for the intersection of curves and surfaces.* Computers & Graphics, 1995. **19**(3): p. 391-403.
159. Abdulkadhim, A., et al., *Crystallization kinetics of V2AlC.* Thin Solid Films, 2012. **520**(6): p. 1930-1933.
160. Janson, M., *CONTES Conversion of Time-energy Spectra a Program for ERDA Data Analysis (Internal Report, Uppsala University).* Internal Report, 2004. **Uppsala University**(Uppsala University).

161. Azina, C., et al., *Oxidation behaviour of V2AlC MAX phase coatings.* Journal of the European Ceramic Society, 2020. **40**(13): p. 4436-4444.
162. Esmaeili, S., et al., *A study on the early-stage decomposition in the Al–Mg–Si–Cu alloy AA6111 by electrical resistivity and three-dimensional atom probe.* Philosophical Magazine, 2007. **87**(25): p. 3797-3816.
163. Rachbauer, R., et al., *Temperature driven evolution of thermal, electrical, and optical properties of Ti–Al–N coatings.* Acta Materialia, 2012. **60**(5): p. 2091-2096.
164. Li, S., et al., *Resistivity in Formation and Decomposition of Natural Gas Hydrate in Porous Medium.* Chinese Journal of Chemical Engineering, 2010. **18**(1): p. 39-42.
165. Williams, W.S., *Scattering of Electrons by Vacancies in Nonstoichiometric Crystals of Titanium Carbide.* Physical Review, 1964. **135**(2A): p. A505-A510.
166. Yu, W., et al., *Solid solution effects in the Ti2Al(CxNy) MAX phases: Synthesis, microstructure, electronic structure and transport properties.* Acta Materialia, 2014. **80**: p. 421-434.
167. Samsonov, G.V. and I.M. Vinickij, *Handbook of refractory compounds / G. V. Samsonov and I. M. Vinitskii*. IFI data base library. 1980, New York [u.a: IFI/Plenum.
168. Okada, S., et al., *Single-crystal growth and properties of CrB, Cr3B4, Cr2B3 and CrB2 from high-temperature aluminum solutions.* Journal of Crystal Growth, 1996. **166**(1): p. 429-435.
169. Guy, C.N., *The electronic properties of chromium borides.* Journal of Physics and Chemistry of Solids, 1976. **37**(11): p. 1005-1009.
170. L'Vov, S.N., et al., *The electrical properties of chromium borides, carbides, and nitrides.* Soviet Powder Metallurgy and Metal Ceramics, 1962. **1**(4): p. 243-247.
171. Kresse, G. and J. Hafner, *Ab initio molecular dynamics for liquid metals.* Physical Review B, 1993. **47**(1): p. 558-561.
172. Perdew, J.P., K. Burke, and M. Ernzerhof, *Generalized Gradient Approximation Made Simple.* Physical Review Letters, 1996. **77**(18): p. 3865-3868.
173. Dahlqvist, M. and J. Rosen, *Impact of vacancies on structure, stability and properties of hexagonal transition metal diborides, MB2 (M = Sc, Y, Ti, Zr, Hf, V, Nb, Ta, Cr, Mo, W, Mn, and Fe).* Materialia, 2022. **26**: p. 101629.
174. van de Walle, A., et al., *Efficient stochastic generation of special quasirandom structures.* Calphad, 2013. **42**: p. 13-18.
175. Paier, J., et al., *Screened hybrid density functionals applied to solids.* The Journal of Chemical Physics, 2006. **124**(15): p. 154709.
176. Khazaei, M., et al., *Novel MAB phases and insights into their exfoliation into 2D MBenes.* Nanoscale, 2019. **11**(23): p. 11305-11314.
177. Blöchl, P.E., *Projector augmented-wave method.* Physical Review B, 1994. **50**(24): p. 17953-17979.
178. Kresse, G. and D. Joubert, *From ultrasoft pseudopotentials to the projector augmented-wave method.* Physical Review B, 1999. **59**(3): p. 1758-1775.
179. Monkhorst, H.J. and J.D. Pack, *Special points for Brillouin-zone integrations.* Physical Review B, 1976. **13**(12): p. 5188-5192.
180. Methfessel, M. and A.T. Paxton, *High-precision sampling for Brillouin-zone integration in metals.* Physical Review B, 1989. **40**(6): p. 3616-3621.
181. Ade, M. and H. Hillebrecht, *Ternary Borides Cr2AlB2, Cr3AlB4, and Cr4AlB6: The First Members of the Series (CrB2)nCrAl with n = 1, 2, 3 and a Unifying Concept for Ternary Borides as MAB-Phases.* Inorganic Chemistry, 2015. **54**(13): p. 6122-6135.

182. Togo, A. and I. Tanaka, *First principles phonon calculations in materials science.* Scripta Materialia, 2015. **108**: p. 1-5.
183. Stoffel, R.P., et al., *Ab Initio Thermochemistry of Solid-State Materials.* Angewandte Chemie International Edition, 2010. **49**(31): p. 5242-5266.

10 Supplementary Material

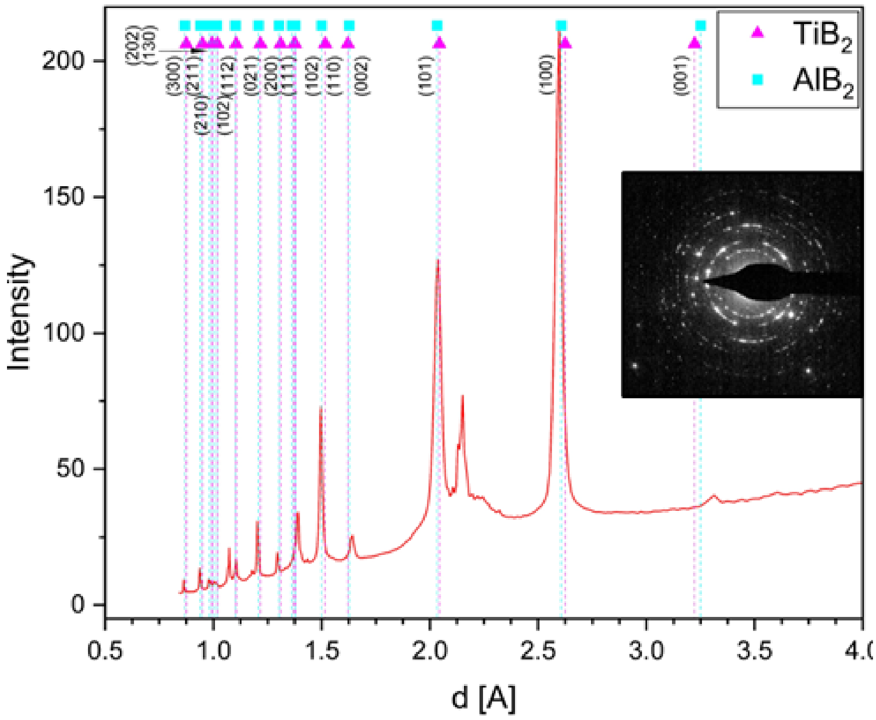

Figure S 1. Integrated intensity of SAED pattern of as deposited $Ti_{0.12}Al_{0.21}B_{0.67}$ sample with peak positions for TiB_2 [42] and AlB_2 [43] as well as SAED pattern.

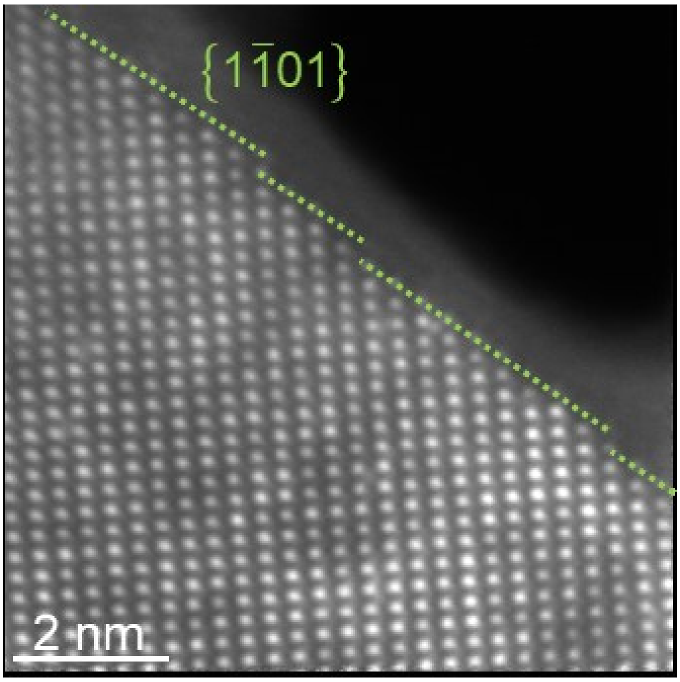

Figure S 2. HRSTEM image of the column asperity at the coating/oxide interface. $(1\bar{1}01)$ facets can be observed.

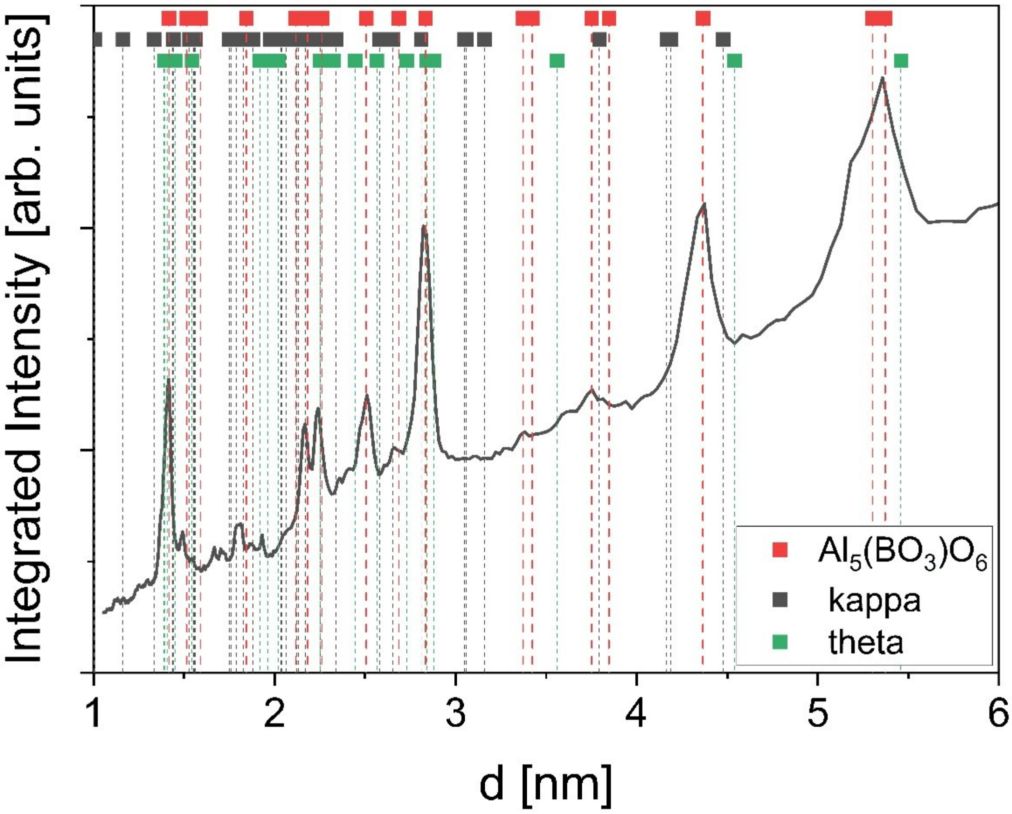

Figure S 3. Integrated intensity of SAED pattern of $Ti_{0.12}Al_{0.21}B_{0.67}$ sample annealed at 900 °C for 8 h, see Figure 4 (f), with peak positions for $Al_5(BO_3)O_6$ [100], θ- [102] and κ- [103] alumina.

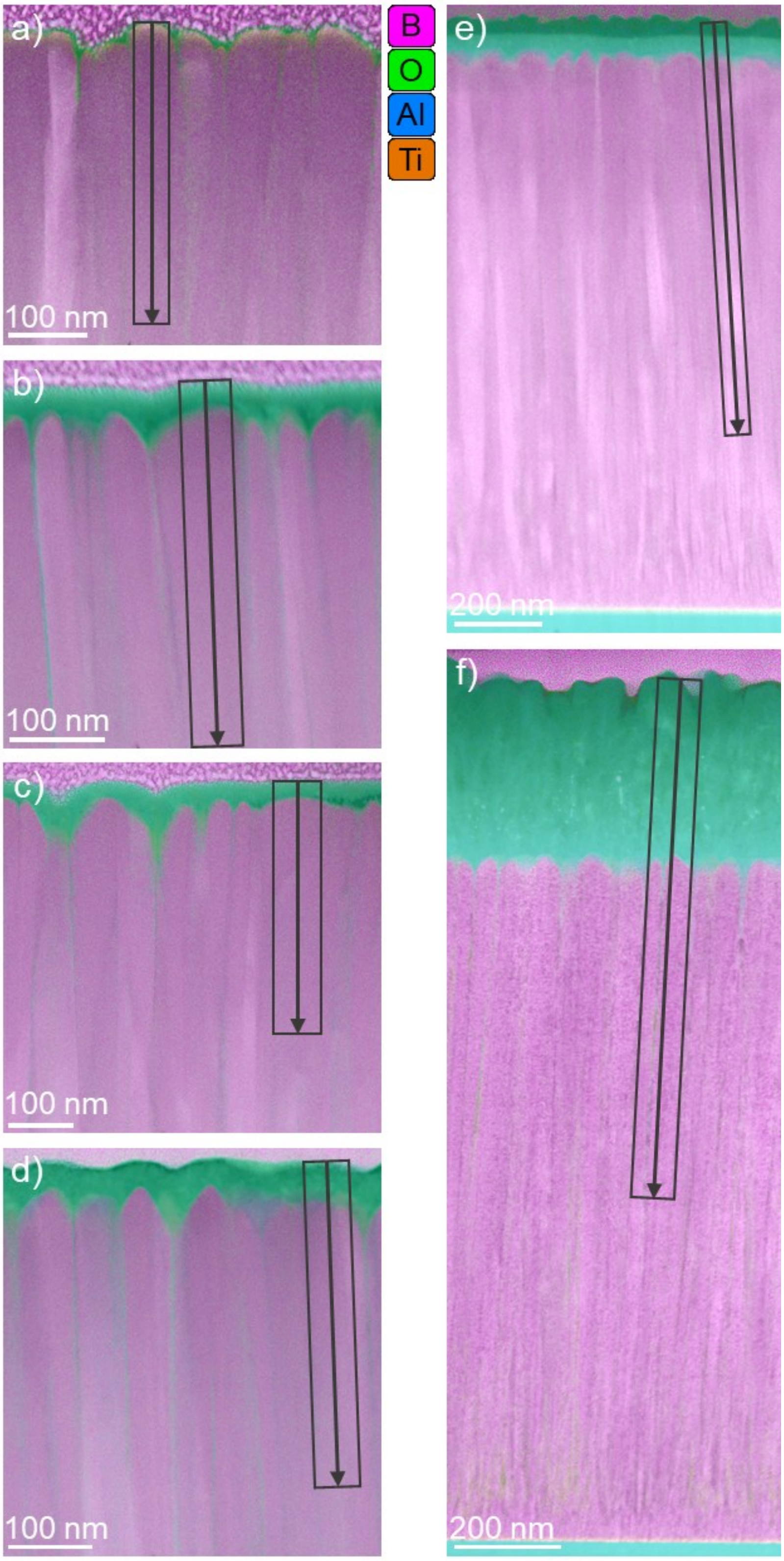

Figure S 4. EDX maps and line scans corresponding to Figure 6, of as deposited (a) and oxidized $Ti_{0.12}Al_{0.21}B_{0.67}$coatings at 700 °C for 1 (b), 4 (c) and 8 h (d), 800 °C for 8 h (e) and 900 °C for 8 h (f).

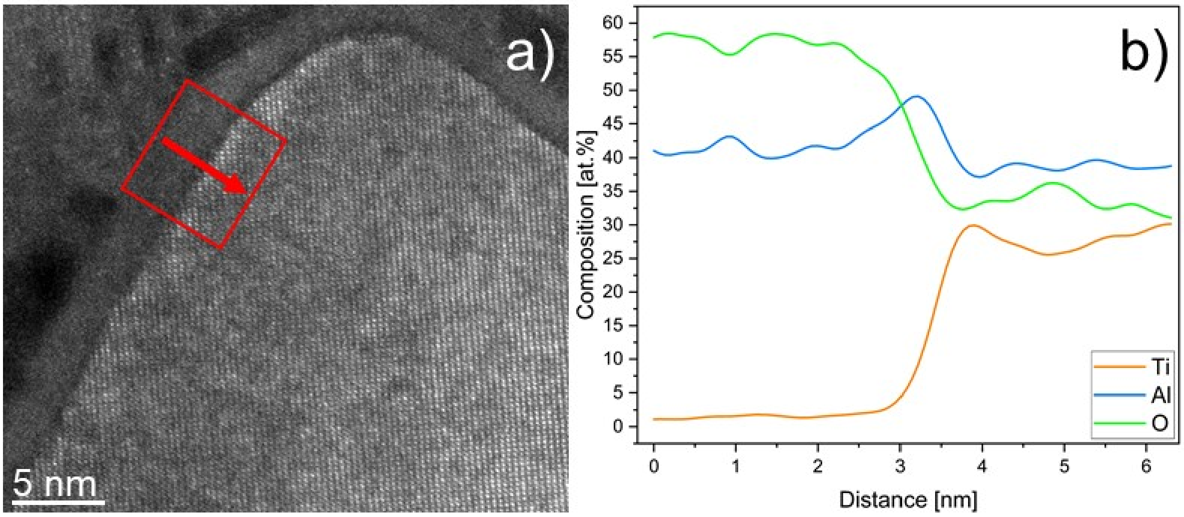

Figure S 5. HRSTEM image of the tip of a grain of the oxidized sample (700 °C, 8 h) (a) and line scan of the interface (b). Compared to the coating composition, the oxide scale is composed mainly of Al and O, consistent with the lower resolution data displayed in **Figure 4 (a)** and **Figure 6 (d)**, with an Al enrichment at the scale/coating interface between 2.5 and 4 nm.

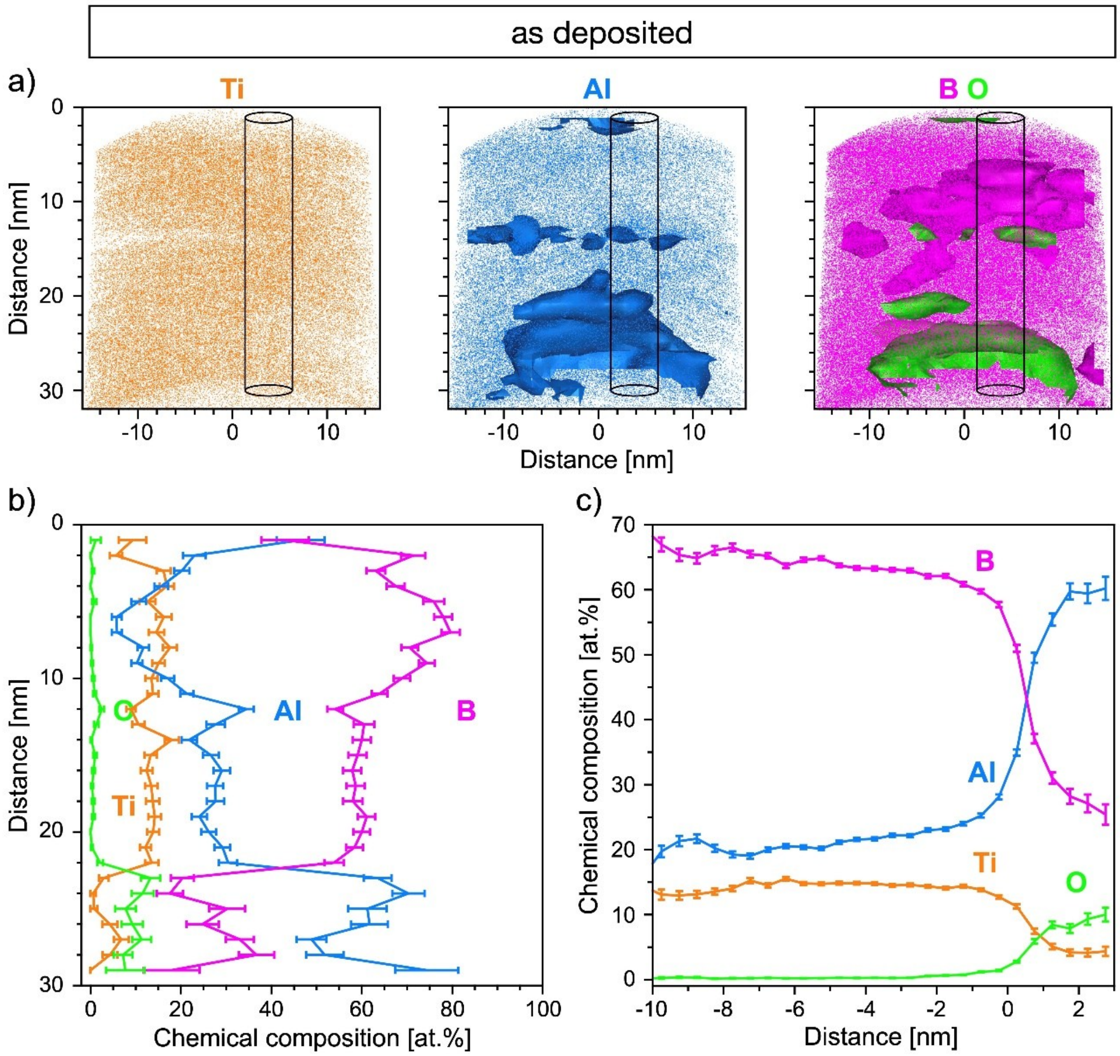

Figure S 6. APT data for as deposited sample from an in-plane specimen. Atomic positions of Ti, Al, B and O are shown together with isoconcentration surfaces of Al ≥ 30 at.%, B ≥ 70 at.%, O ≥ 4 at.% (a). The composition profile is extracted from a cylindrical region with a diameter of 5 nm (b) and the proximity histogram shows Al-rich regions ≥ 30 at.% (c).

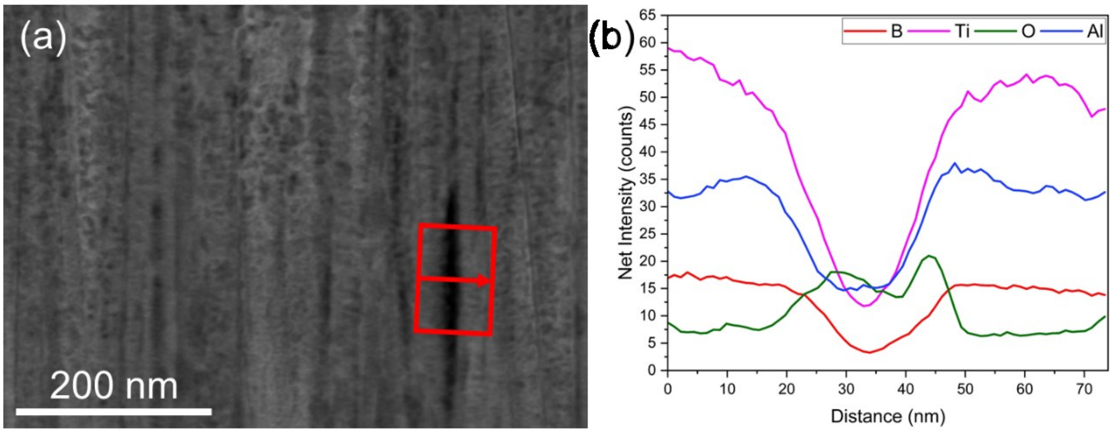

Figure S 7. HAADF image of Ti$_{0.12}$Al$_{0.21}$B$_{0.67}$ coating annealed at 1000 °C for 3 h including an EDX line scan and the corresponding net intensity (b). The net intensity is significantly decreased in the dark region confirming the presence of pores.

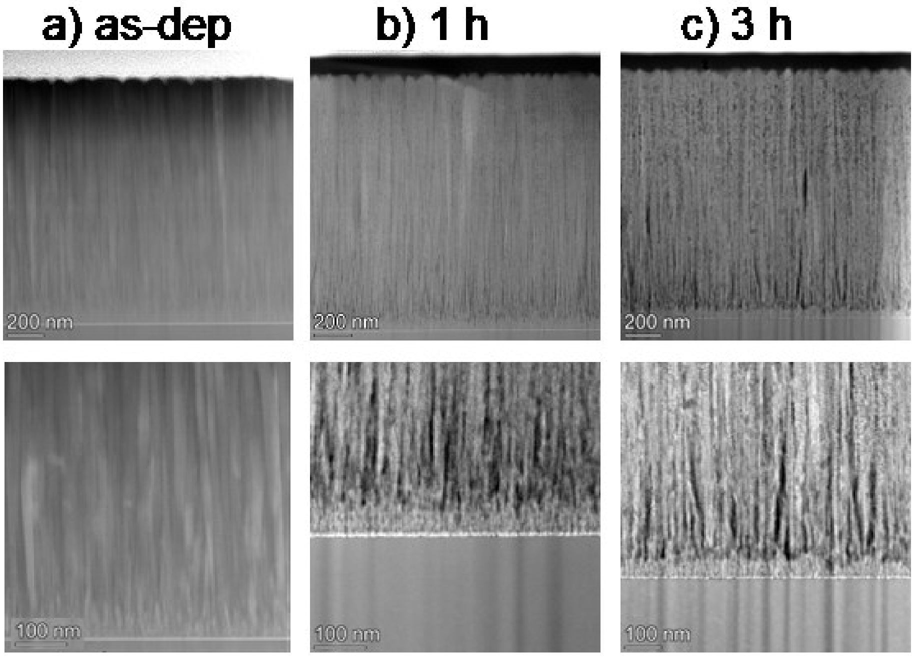

Figure S 8. HAADF images of $Ti_{0.12}Al_{0.21}B_{0.67}$ coating (a) as-deposited and (b) and (c) annealed at 1000 °C.

Computational details Chapter 4

Ab initio calculations were performed in the framework of density functional theory (DFT) [64, 66] as implemented in the Vienna *Ab initio* Simulation Package (VASP) [90, 171]. A plane-wave basis set with the generalized gradient approximation (GGA) in the Perdew-Burke-Ernzerhof (PBE) parameterization [172] was applied to describe the exchange-correlation effects. As cutoff energy, 500 eV was chosen based on the results of convergence test runs on a selection of configurations. The cutoff for the forces was set in accordance with previous publications for similar systems i.e. [173]. The first Brillouin zone was sampled with a 6 × 6 × 6 K-point mesh centered at the Γ point. The calculations were considered converged with an energy difference of 10^{-5} eV and atomic forces lower than 10^{-2} eV/Å. For the calculations, 4 × 4 × 4 supercells containing 192 atoms were created based on the hexagonal TiB_2 structure. The sublattices were populated with the special quasi-random structure (SQS) method [174].

Lattice Parameters

To determine the experimental lattice parameters, the CellCalc software V.2.10. was employed while a profile fitting-based software (TOPAS V.3) with a pseudo-Voigt II function was used for peak fitting on the measured XRD diffractograms. The experimental and calculated values of the lattice parameters and the equilibrium volumes are shown and compared in Figure S 9. The maximum differences of experimental lattice parameters and unit cell volumes between TiB_2 (PDF cards 00-035-0741) and AlB_2 (PDF cards 00-008-0216) are 1.0 and 0.4 %, respectively, while these differences for DFT calculated values are 1.9 and 0.3 % (Figure S 9), showing very similar lattice parameters. This can serve as an explanation for the absence of peak splitting in the diffractogram. Moreover, the experimentally determined lattice parameters of the as-deposited and the annealed thin films exhibit maximum deviations of 0.8 % from the calculated corresponding DFT values. According to Paier *et al*., [175] deviations of ≤ 2 % between experimentally and theoretically determined lattice parameters have to be expected based on the employed exchange-correlation functionals. Hence, the here measured lattice parameters are in very good agreement with DFT predictions.

Figure S 9. Experimental and theoretical values of the lattice parameters and the equilibrium volumes of the as-deposited [12] and annealed $Ti_{0.12}Al_{0.21}B_{0.67}$ films at 1000 °C up to 3 h.

	Exp. a (Å)	Exp. c (Å)	Exp. V (Å^3)	DFT a (Å)	DFT c (Å)	DFT V (Å^3)
As-deposited	3.003	3.279	25.594	3.007	3.265	25.558
1 h anneal	3.010	3.252	25.514	3.001	3.260	25.423
3 h anneal	3.008	3.259	25.533	2.995	3.233	25.106
TiB_2	3.030	3.223	25.683	3.032	3.229	25.707
AlB_2	3.009	3.262	25.577	3.007	3.292	25.778

Figure S 10. Results of resistance measurements for individual samples in as deposited and annealed state as well as thermal coefficient of resistance (TCR) obtained from cooling curves in the contact-based measurements.

Annealing temperature [°C]	Resistance contact-based as dep. [Ohm/sq]	Resistance contact-based annealed [Ohm/sq]	Resistance contactless as dep. [Ohm/sq]	Resistance contactless annealed [Ohm/sq]	TCR [1/°C]
400	3.5	3.6	4.7	4.9	-5.3E-05
500	3.4	3.4	4.9	4.8	-1.2E-04
600	3.5	2.9	4.8	4.0	-1.5E-05
700	3.5	1.1	4.8	1.6	3.1E-04
800	3.5	0.8	4.8	1.2	3.6E-04

Figure S 11. Chemical composition determined *ex situ* by ERDA measurements for samples annealed to the indicated temperatures.

Annealing Temperature [°C]	**Composition**
As dep.	$Cr_{0.34}Al_{0.31}B_{0.35}$
400	$Cr_{0.37}Al_{0.31}B_{0.32}$
500	$Cr_{0.35}Al_{0.31}B_{0.34}$
600	$Cr_{0.35}Al_{0.31}B_{0.34}$
700	$Cr_{0.36}Al_{0.31}B_{0.33}$
800	$Cr_{0.35}Al_{0.30}B_{0.35}$

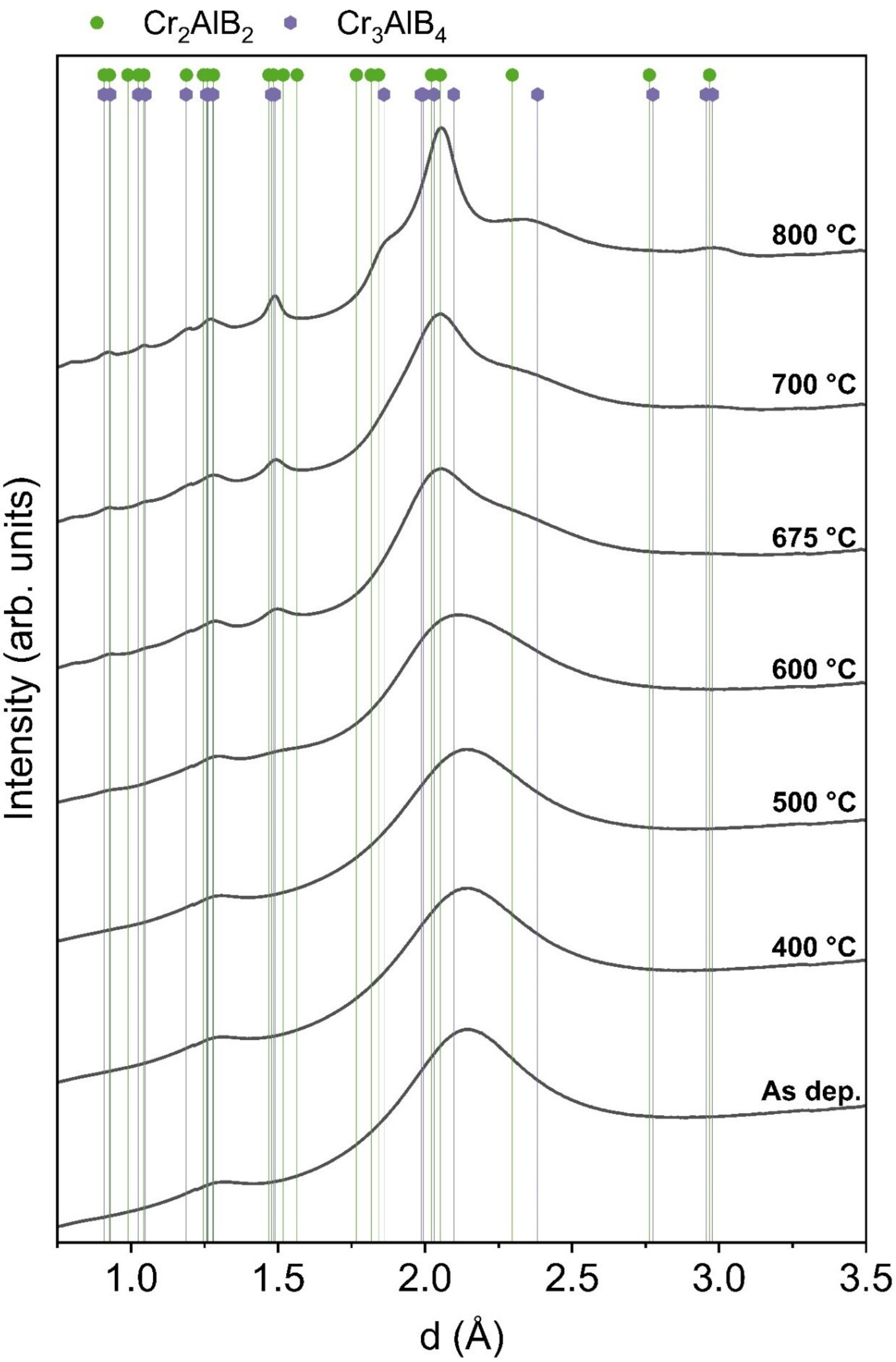

Figure S 12. Integrated SAED patterns for various temperatures extracted during *in situ* annealing with no background subtraction performed. The data were corrected for thermal expansion. Up to 400 °C, no change to the amorphous as deposited state can be seen, while at higher temperatures the formation and grain growth of Cr_2AlB_2 and Cr_3AlB_4 can be seen.

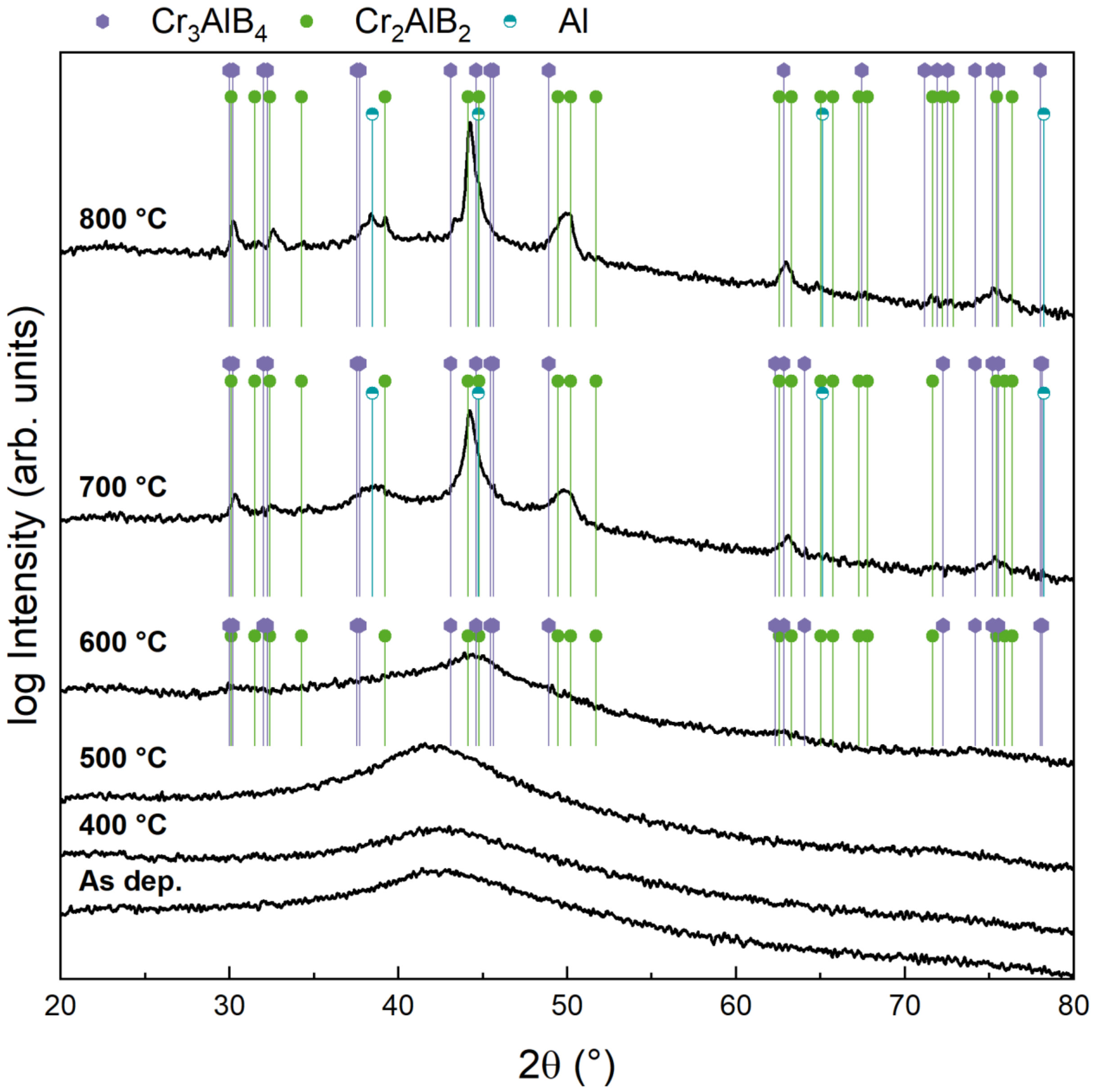

Figure S 13. Full 2θ range of X-ray diffraction carried out for samples annealed at the indicated temperatures. Formation and growth of MAB phases Cr_2AlB_2 and Cr_3AlB_4 can be observed.

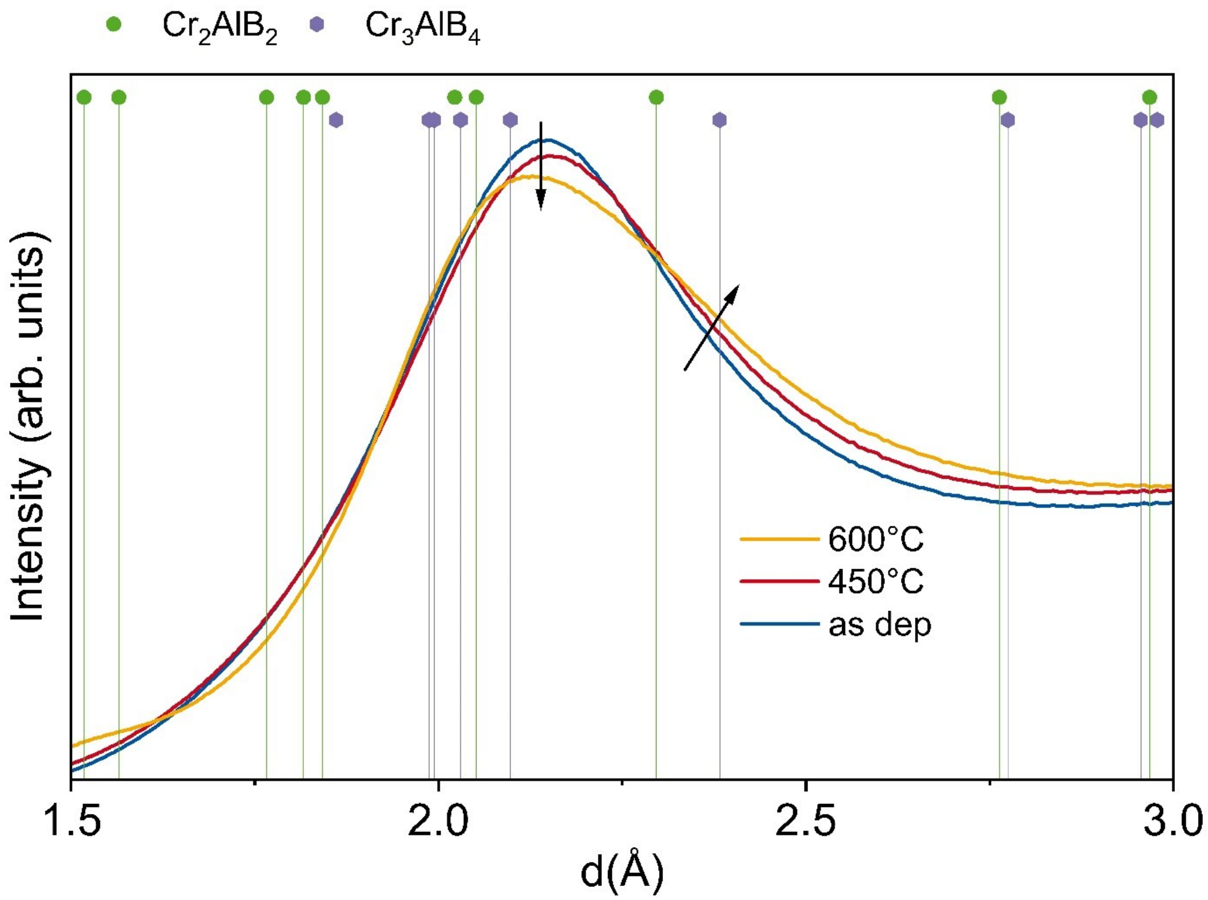

Figure S 14. Comparison of the *in situ* SAED data for the as deposited state and at 450 °C between 1.5 and 3 Å. A shift in the ratio of the intensities below 2.25 Å and above 2.25 Å indicate the formation of a crystalline phase out of the predominantly amorphous matrix.

More detailed analysis of phase formation

To further study phase formation between 450 and 600 °C, longer annealing experiments with holding times of 24 h at 500 °C and 600 °C have been conducted. While SAED data of the sample annealed at 500 °C only reveal the formation of a crystalline Cr-Al-B phase (Figure S 16), the formation of the Cr_2AlB_2 MAB phase at this temperature is clearly shown by HRSTEM in Figure S 17a. This can be rationalized by the reported calculated enthalpies of formation predicting Cr_2AlB_2 to be energetically favored over Cr_3AlB_4, even though the experimental chemical composition here differs from the theoretically assumed [176]. However, due to the low reported energetic difference (0.044 eV/atom) between both phases, concurrent formation of Cr_3AlB_4 cannot be fully ruled out at this temperature.

After annealing at 600 °C, the formation of both Cr_2AlB_2 and Cr_3AlB_4 can be observed (Figure S 16, Figure S 17b), whereby the observed phase fraction of Cr_2AlB_2 is significantly larger compared to Cr_3AlB_4. The higher amount of Cr_2AlB_2 correlates with the higher DSC peak intensity of the first transition (orange colored region Figure 2) and with the lower energetic barrier of formation, while the lower fraction of Cr_3AlB_4 correlates with the second transition (blue colored region Figure 2) and the slightly higher enthalpy of formation [176]. All of the above indicates that the first transition observed here (orange colored region Figure 2) corresponds to the formation of the Cr_2AlB_2 MAB phase, whereas the second transition (blue colored region Figure 2) corresponds to the formation of the Cr_3AlB_4 MAB phase while concurrent formation due to structural and energetic similarity cannot be fully ruled out.

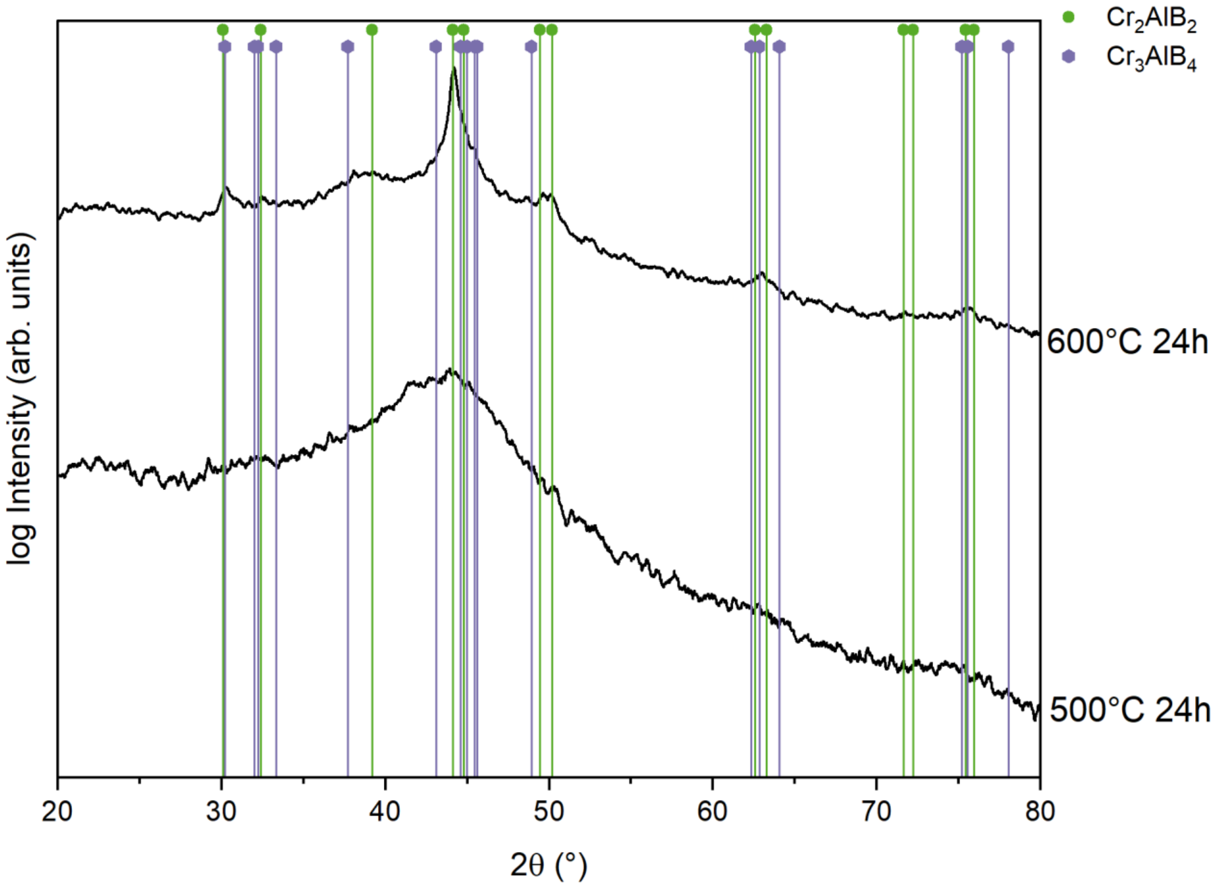

Figure S 15. XRD measured of samples annealed for 24 h at the indicated temperatures to narrow down phase formation. After 600 °C peaks corresponding to Cr_2AlB_2 start emerging which cannot be seen at the lower temperature.

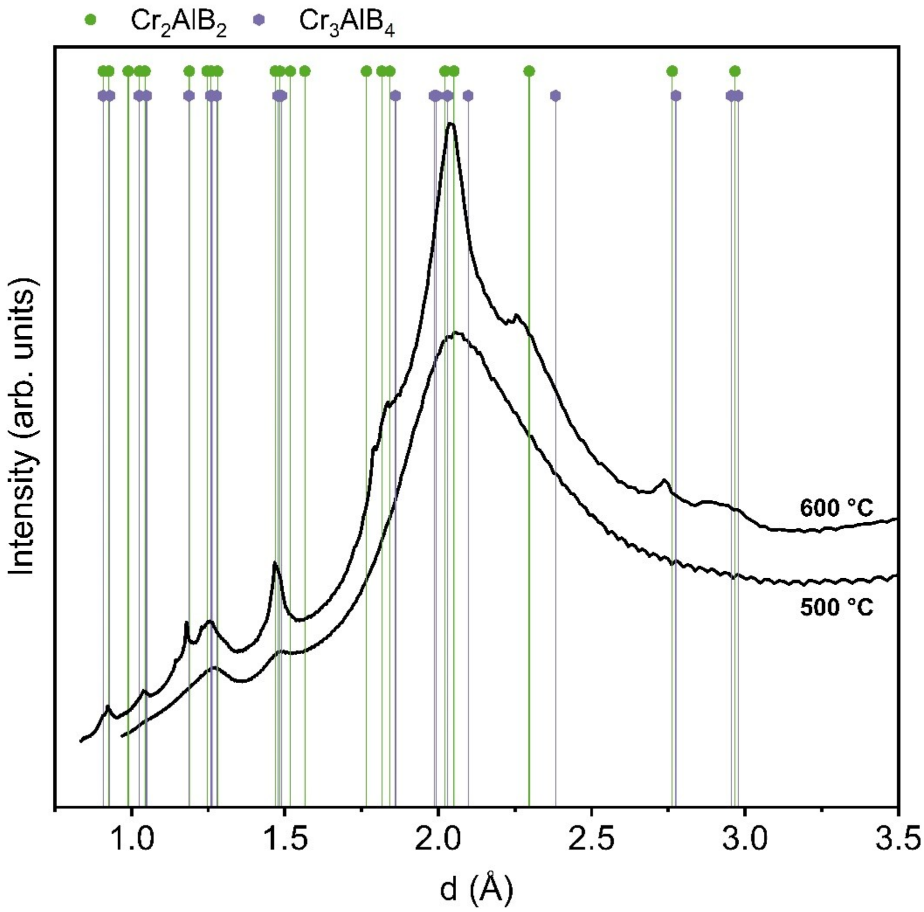

Figure S 16. Integrated intensity of SAED patterns of samples annealed at 500 and 600 °C for 24 h. The formation of a MAB phase is indicated by the presence of three distinct peaks after 500 °C, while the presence of Cr_2AlB_2 and Cr_3AlB_4 as well as a significant increase in crystallinity and crystal size is visible after annealing at 600 °C.

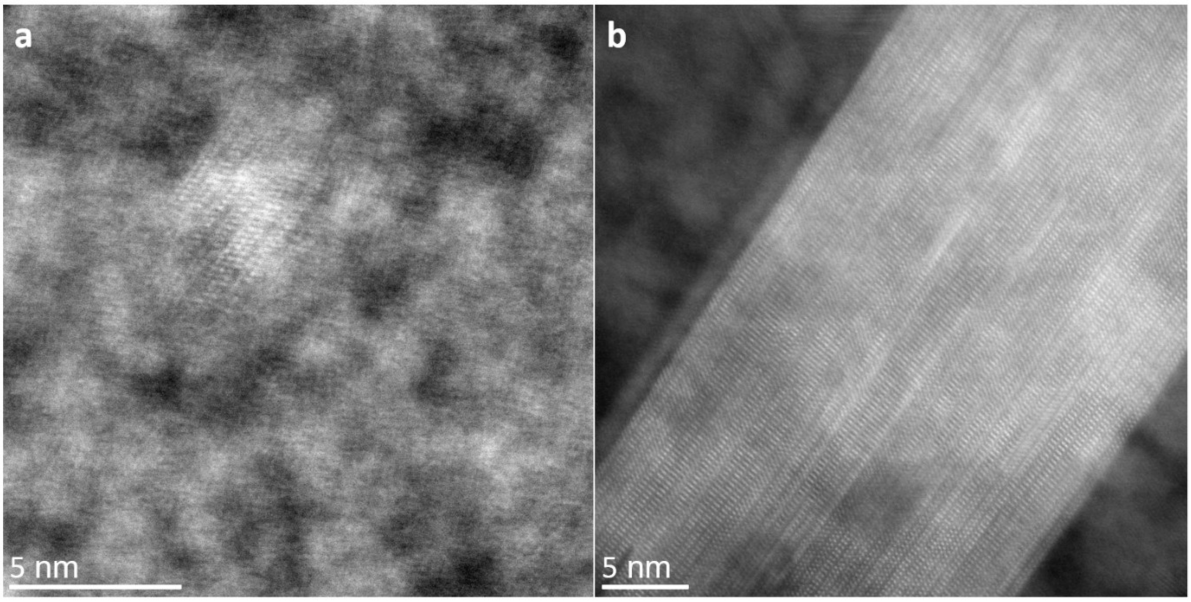

Figure S 17. *Ex situ* HRSTEM micrographs of 24 h annealed samples at 500 °C (a) and 600 °C (b). MAB crystallites containing the Cr_2AlB_2 phase are formed after 500 °C. The crystal size is significantly increased after 600 °C, whereby the Cr_2AlB_2 as well as the Cr_3AlB_4 phase can be identified.

Figure S 18.: Supplementary video grain growth

Available electronically

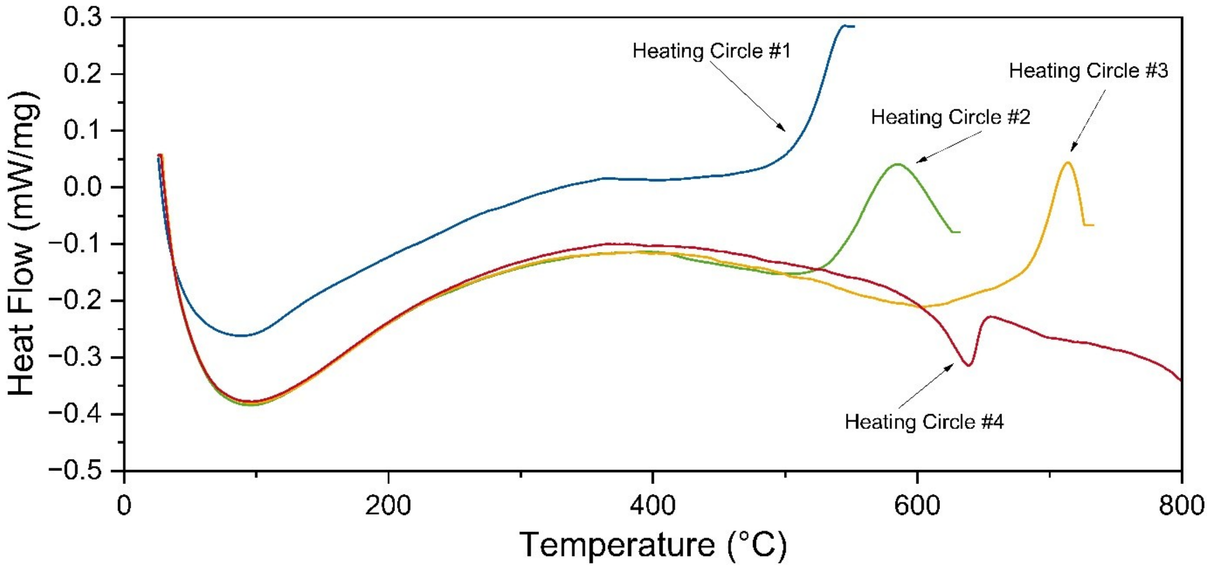

Figure S 19. DSC curves for repeated heating. In addition to the peaks corresponding to exothermic amorphous crystalline transformations (heating cycles 1 to 3), an endothermic peak corresponding to Al melting can be observed in the 4th heating cycle (red curve).

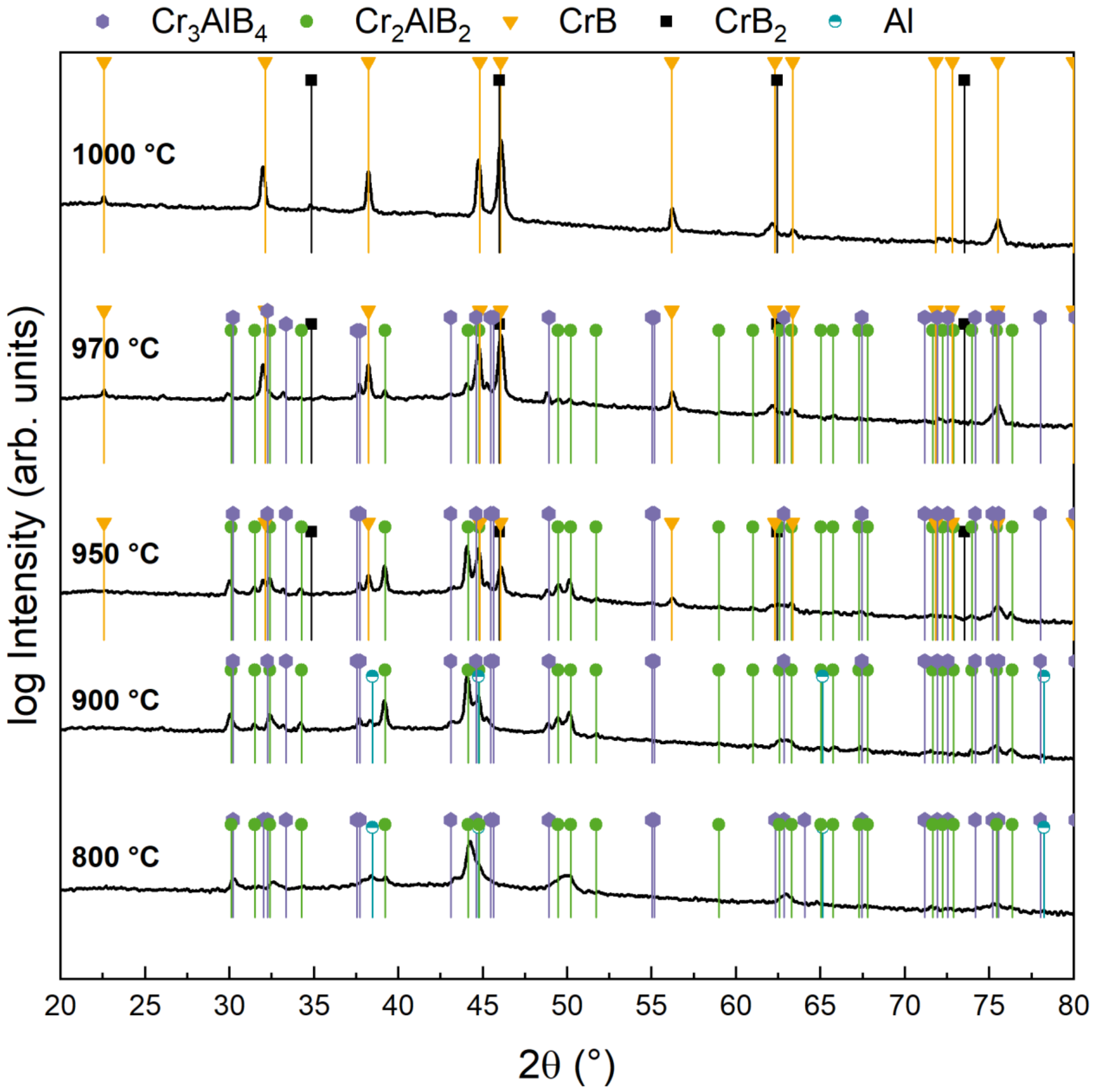

Figure S 20. Full 2θ range for *ex situ* recorded XRD.

Computational Methods Chapter 6

A lattice dynamics approach based on density functional theory (DFT) calculations was utilized to calculate temperature-dependent Gibbs energies of formation. For the DFT runs, the Vienna ab initio Simulation Package (VASP, version 5.4.4, University of Vienna, Austria) was used [90, 91, 171]. The basis set was generated using the projector-augmented wave method [177, 178] with a cutoff energy of 500 eV and the well-established generalized gradient approximation (GGA) functional as parametrized by Perdew, Burke, and Ernzerhof (PBE) [172], employed to treat electronic exchange and correlation. The atomic potentials, modeling the valence electron configurations were $4s^2 3d^4 3p^6$ for Cr (semi-core states incorporated), $3s^2 3p^1$ for Al, and $2s^2 2p^1$ for B. The Monkhorst-Pack method [179] was used to construct the *k* mesh in the irreducible Brillouin zone. Since the *k* mesh varied for each system, they will not be listed in full, however, the density was chosen to ensure energetic convergence up to 10^{-3} eV for each system as verified *via* convergence tests. Brillouin zone integration was done by the Methfessel-Paxton method [180] of order 1.

The structural models of MAB phases were constructed with initial data from literature [181] and subsequently fully optimized in the ground state. Afterward, these optimized models were fed as an input for the lattice dynamics simulations, using VASP and the *phonopy* package (version 2.11.0, University of Kyoto, Japan) [182] as a postprocessing code. This approach is described in greater detail in literature [183] and our recent publication [153].

The Gibbs energies of formation were calculated with the G(T) data from MAB phases and competing phases according to:

$$\Delta G(T) = \Sigma\, x\, G(T)(\mathrm{product}) - \Sigma\, y\, G(T)(\mathrm{starting\ materials})$$

with *x* and *y* corresponding to the stoichiometric coefficients of the individual reactants.

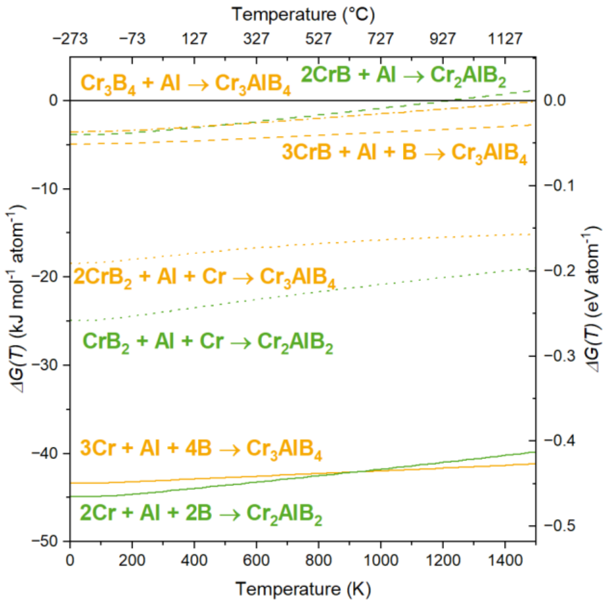

Figure S 21. Temperature-dependent Gibbs free energies of formation obtained by DFT and lattice dynamics simulations for Cr_2AlB_2 and Cr_3AlB_4 MAB phases compared to the constituting elements and CrB, CrB_2, and Cr_3B_4 as competing phases.

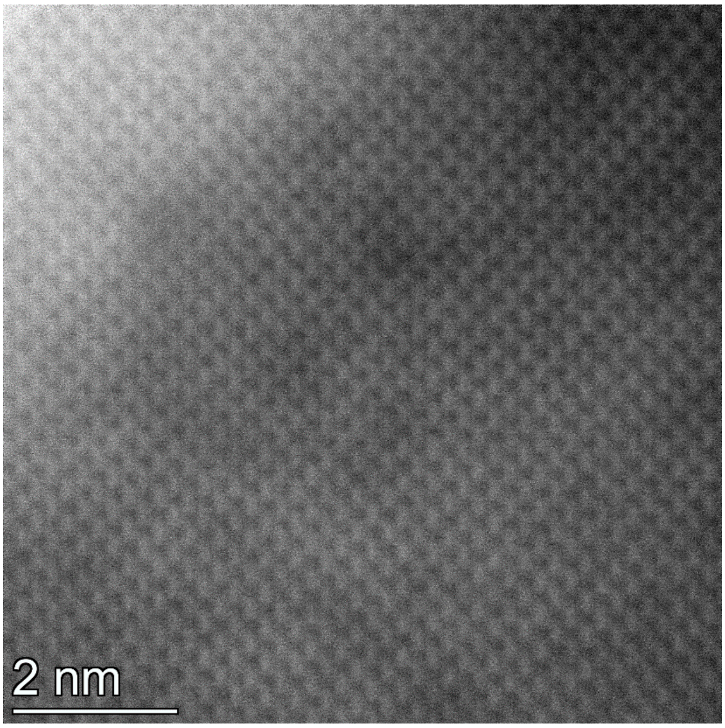

Figure S 22. HRSTEM micrograph of a sample annealed to 950 °C showing a CrB region.

Figure S 23. Supplementary video decomposition

Available electronically

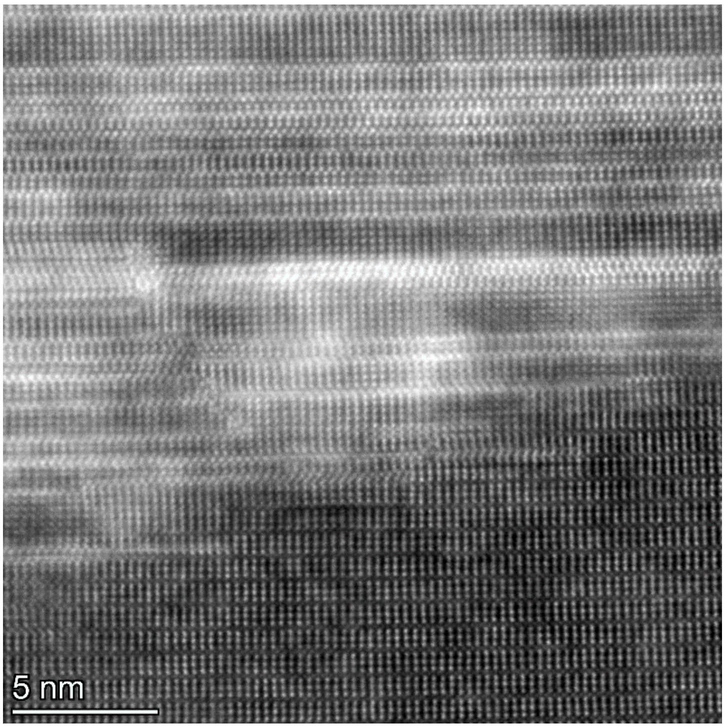

Figure S 24. HRSTEM micrograph of sample annealed to 1000 °C, showing small remaining regions of the Cr_3AlB_4 MAB phase.

Figure S 25. Results of resistance measurements for individual samples after annealing and thermal coefficients of resistance (TCR) obtained from cooling curves in the contact-based measurements.

Annealing temperature [°C]	Resistance contact-based annealed [Ohm/sq]	Resistance contactless annealed [Ohm/sq]	TCR [1/°C]
800	0.8	1.2	3.6E-04
900	0.8	1.1	5.6E-04
950	1.2	1.7	7.5E-04
970	2.5	3.4	7.5E-04
1000	3.2	4.6	7.6E-04